CURRENT SENSING ATOMIC FORCE MICROSCOPY STUDY OF AGING MECHANISM OF NAFION MEMBRANES DUE TO THERMAL ANNEALING

A DISSERTATION IN
Physics
And
Engineering

Presented to the Faculty of the University
of Missouri-Kansas City in partial fulfillment of
the requirement for the degree

DOCTOR OF PHILOSOPHY

by
O SUNG KWON

B.A., Myoung-Ji University, Young-In, R.O. Korea, 1999

M.S., University of Missouri-Kansas City, Kansas City, MO, USA, 2007

Kansas City, Missouri
2011

CURRENT SENSING ATOMIC FORCE MICROSCOPY STUDY OF AGING MECHANISM OF NAFION MEMBRANES DUE TO THERMAL ANNEALING

O Sung Kwon, Candidate for the DOCTOR OF PHILOSOPHY Degree

University of Missouri-Kansas City, 2011

ABSTRACT

Proton transport properties of Nafion 212 and Nafion 115 membranes have been studied using current sensing atomic force microscopy to reveal changes of the ionic domains and the local ionic conductivity distribution in the membranes due to the aging.

The current sensing atomic force microscopy (CSAFM) is a novel technique which can map morphological and electronic structures of materials on nanometer scales. The technique has been employed in this work to study the ionic structures of Nafion membranes which consist of proton conductive hydrophilic side chains embedded in non-conductive hydrophobic backbones. The hydrophilic side chains aggregate forming ionic domains which could be interconnected when the membrane adsorbs water. We used CSAFM to image the ionic channel network and monitor their changes in a thermal aging process.

The results reveal that the thermal aging process undergoes two steps: First, the ionic channels on the membrane surface changes from cluster-like to chain-like structure, accompanied by an increase of the conductance of the membrane. The observed changes can be explained in terms of reorientation of ionic channels near the membrane surface from perpendicular to parallel to the surface as the annealing temperature approaches the glass transition of the membranes. Second, as the annealing continues, the chain-like structure of

the proton channels persists but the conductance of the membranes decreases. The observed conductance decreasing can be explained by sulfonic acid group decomposition due to produce sulfonic acid anhydride.

The faculty listed below, appointed by the Dean of the Collage of Art and Sciences have examined a dissertation titled “Current Sensing Atomic Force Microscopy Study of Aging Mechanism OF The Nafion Membranes due to Thermal Annealing,” presented by Osung Kwon, candidate for the Ph. D of Physics degree, and certify that in their opinion it is worthy of acceptance.

Supervisory Committee

Da-Ming Zhu, Ph.D., Committee Chair

Department of Physics

Michael B. Kruger, Ph. D.

Department of Physics

Wai-Yim Ching, Ph. D.
Department of Physics

Bryan R. Becker, Ph. D.
Department of Civil and Mechanical Engineering

Ganesh Thiagarajan, Ph. D.
Department of Civil and Mechanical Engineering

TABLE OF CONTENTS

LIST OF ILLUSTRATIONS

Figure Page

LIST OF TABLES

Table Page

ACKNOWLEDGEMENTS

I would like to specially thank my advisor, Dr. Zhu. His intelligence and enthusiasm have inspired me to overcome the difficulties encountered during my research and the process of writing this dissertation. His patience and a lot of advices helped me to complete my dissertation.

My special gratitude goes to Dr. Ching, Dr. Kruger, Dr. Becker, and Dr. Thiagarajan for being my committee members, spending time reading my thesis and giving comments. Also, I especially appreciate my colleague Xie Xin, Yihong Kang, and Yucong Liu. They give me a lot of advice and inspiration to finish my dissertation research.

Finally, I would like to thank to my wife Hyunsim Kim. Her encouragement and consolation has become the panacea to me whenever I have problems. Her patience and sacrifice helped me in finishing my research. Also, I thank my family for their financial and spiritual support.

CHAPTER 1

INTRODUCTION

1.1 Fuel Cell

Global environmental concerns and the ever-increasing demands for fossil and electrical energy have created significant challenges for energy sustainability and urgent needs for revolutionary innovations in renewable energy technologies. Besides various alternative renewable energy technologies, such as solar panels, wind blades, geothermal heating pump, etc, the fuel cells are considered as the one of the most promising and environmentally friendly energy-conversion solutions that offer high fuel economy, higher efficiency, and substantially lower CO_2 emission for solving current issues due to use of fossil fuels. [1, 2]

All different types of fuel cells have the same operating principals. Figure 1 illustrates the configuration of proton exchange membrane and chemical reaction at the catalyst. At the anode, a fuel such as hydrogen is oxidized into proton and electrons while at the cathode, oxygen is reduced to oxide species and these then react from the water. Depending upon the electrolyte, either protons or oxide ions are transported through an ion conducting but electronically insulating electrolyte while electrons travel round an external circuit delivering electrical power. [3]

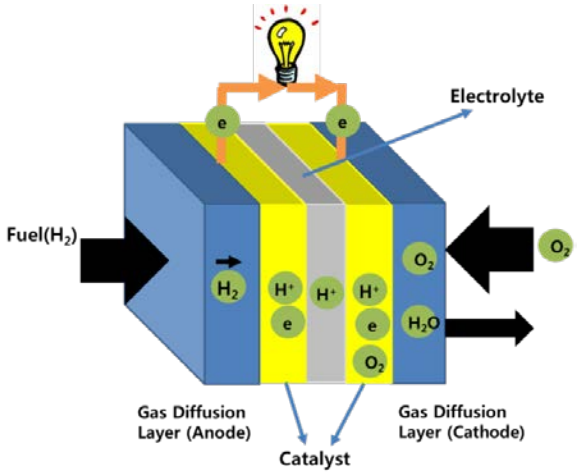

Figure 1. Configuration and chemical reaction of typical fuel cell

There are several different types of the fuel cell, which all have the same basic operating principle. The configuration of the fuel cells is that the electrolyte is located between two electrodes and the electrodes connected with external circuit which produces electric power. [3, 4, 5, 6] There are five types of fuel cells which are most widely studied and used. The five types of fuel cell are alkaline fuel cells (AFCs), phosphoric acid fuel cells (PAFCs), molten carbonate fuel cells (MCFCs), solid oxide fuel cells (SOFCs), and the polymer electrolyte membrane (PEM) fuel cells. [2, 3, 4, 5]

Alkaline fuel cells (AFCs) are one of the first developed fuel cell and were used for the early U.S. space program [3, 7, 8]. AFCs are low operating temperature fuel cell. Because of the low operating temperature, they do not need precious metal catalysts such as platinum. [8] So, various non-precious metals such as copper and nickel are used for accelerating the reactions. [8] Even though many advantages, AFCs have a couple of disadvantages. First, the

AFC system easily is poisoned by carbon dioxide. Even a small amount of carbon dioxide easily drops the AFC performance. Second, pure hydrogen and oxygen are needed to operate AFCs. AFCs use an aqueous solution of either sodium or potassium hydroxide as the electrolyte, with hydrogen as the fuel and air or pure oxygen as the oxidant, and have an operating temperature of around 70^{o}C. [2] The carbon with a potassium catalyst is used for the electrodes of fuel cell. The basic chemistry of the alkaline fuel cell is given below.

Anode: $2H_2+4OH^- \rightarrow 4H_2O+4e$

Cathode: $O_2+4e+2H_2O \rightarrow 4OH^-$

The AFCs have still many important advantages even if their importance and research interest are decreasing. [3]

Phosphoric acid fuel cells (PAFCs) are one of the early commercialized fuel cells because they have three significant advantages: they are relatively clean, they reform hydrocarbon, and they clean-up coal gas from gasifier [9]. PAFCs consist of proton-conducting electrolyte and platinum (Pt) or Pt alloy catalyst. The electrolyte, concentrated phosphoric acid (H_3PO_4), is a proton conductor, thus protons migrate from the anode to the cathode. Phosphoric acid also known as inorganic acid has thermal, chemical, and electrical stability and has low volatility. [9, 10] Unlike alkaline fuel cell, it has tolerance for CO_2 in the fuel and oxidant. Typically, operating temperature of the PAFCs is between 150^{o}C and 200^{o}C. Since the electrolyte is in liquid form, it must be protected water by the hydrophobic electrode. This is generally achieved by using polytetrafluoroethylene (PTFE) solution. In addition, the electrode must have good conductivity. For these reasons, electrodes are made of PTFE-bonded Pt/C. [3, 9, 10] A summary of the electrodes' reactions are

Anode: $2H_2 \rightarrow 4H^+ + 4e$

Cathode: $O^2 + 4H^+ + 4e \rightarrow 2H_2O$

Overall: $2H_2 + O_2 \rightarrow 2H_2O$

The PAFC stack consists of series of ribbed bipolar plates, the anode, electrolyte matrix, and cathode. The ribbed bipolar plate works as the separator of the single PAFC and electrical connector. Also the ribbed bipolar plate provides gas supply to anode and cathode. The PAFC stack contains 50 or more single PAFCs. The stack must include cooling system to remove heat from the cell operation. Usually cooling is done by water and air. The water cooling system is usually used in the 100-KW class and above because it has disadvantage. The disadvantage of water cooling system is that the water treatment is needed to prevent corrosion of the cooling pipes and blockage developing in the cooling loops and it rises manufacturing cost. For small fuel cell systems, the air cooling system is used. [3, 9] Typically, cell performance is affected by pressure, temperature, reactant gas. Also, the performance strongly depends on the purity of the gases. Even if small amounts of carbon monoxide are included H_2 gas, carbon monoxide seriously poisons the anode and the electro-catalytic activity of Pt electrode. Also, hydrogen sulfide and carbonyl sulfide from purity of fuel gases and coal gasifiers in PAFC power plant become cause of efficiency drop because of the hydrogen sulfide absorbs on Pt and blocks the active sites for H_2 oxidation. The goal of the cell performance is that the cell continuously operates 40000 hours. For this purpose, the degradation rate must be

$$\Delta V_{lifetime}(mV) = -3mv/1000 \text{ hours.}$$

Among the various fuel cell types the molten carbonate fuel cells (MCFCs) have incompatible advantages for industrial applications as well as for dispersed power supply

because they can be used for stationary generation of electric energy together with the production of highly valuable heat. [11] MCFCs have a molten potassium carbonate electrolyte which requires an operating temperature of around $65^{o}C$. In recent years, a porous sintered Ni-Cr/Ni-Al alloy is used as an anode and Lithiated NiO is used as a cathode. They run on a mixture of hydrogen and carbon monoxide which is formed by internally reforming practical hydrogen fuels within the fuel cell. At the anode, the carbonate ions are converted back into CO_2. There is therefore a net transfer of CO_2 from cathode to anode; one mole of CO_2 is transferred along with two Faradays of charge or two moles of electrons. [3] A summary of the electrodes' reactions are given below:

$$\text{Anode: } 2H_2+2CO^{2-}_3 \rightarrow 2H_2O+2CO_2+4e$$

$$\text{Cathode: } O_2+2CO_2+4e \rightarrow 2CO^{2-}_3$$

$$\text{Overall: } H_2 + \frac{1}{2}O_2 + CO_2 \rightarrow H_2O + CO_2$$

The stack configuration of the MCFCs is different from other fuel cells. One of the most significant differences is the aspect of sealing because the MCFC stack is composed of various porous and non-porous components. Thus it is very important that the sealing of the stack makes the good flow distribution of gases between individual cells, uniform distribution within each cell, and good thermal management to reduce temperature gradients throughout the stack. [3]

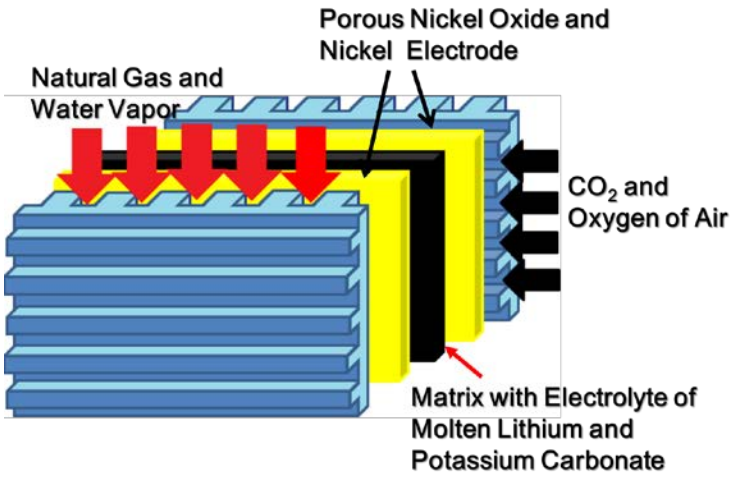

Figure 2. The stack configuration of molten carbon fuel cell

Solid oxide fuel cells (SOFCs) typically contain two porous electrodes, interposed between electrolytes made of a particular solid oxide ceramic material. [13] The operating temperature of a SOFC is 600°C-1000°C. There are two advantages due to high operating temperature of the SOFC. The first advantage, the SOFCs do not need pernicious material catalyst such as platinum. Therefore, carbon monoxide does not represent a harmful substance for the anode. The second advantage, hydrocarbons are internally reforming. The reaction is written by:

$$C_x H_y O_z + (2x - z) H_2 O \rightarrow x CO_2 + \left(\frac{y}{2} + 2x - z \right) H_2 .$$

This reaction is endothermic and thermal energy is accepted from the overall reaction (exothermic reaction) of the fuel cell. Thus almost no energy is lost from the fuel cell operation. [3, 4, 5, 6, 13] A summary of the electrode reaction is given below

Anode: $2H_2+2O^{=}\rightarrow 2H_2O+4e$

Cathode: $O_2+4e\rightarrow 2O^{=}$

Overall: $H_2+CO+O_2\rightarrow H_2O+CO_2+\Delta E$

There are two types of geometrical designs of the cell which are flat planar and tubular design. In flat planar, the electrodes, the electrolyte and the current collectors, are present as a flat planar geometry and arranged in the sandwich configuration as shown figure 3 (a). The advantages of this configuration are that the structure of the cell is simple, relatively easy and inexpensive to construct and the power density is relatively high. However, this design has a couple of problems. First, because each component has a different thermal expansion coefficient, cracking is induced in the cell. So, the maximum active surface is limited as some hundred cm^2. Second, cell has high contact resistance between electrode and electrolyte. The third, because of the geometrical configuration, it is very difficult to find proper materials which can be fulfill the chemical and physical properties.

Because of the disadvantages of flat planar, the tubular design of the cell is recently used (figure 3 (b)). The design of tubular is the overlap of the three cylinders such as cathode, electrolyte, and anode as shown figure 3 (b). One end of the cylinder is closed and another end of the cylinder is opened. From the opening, air is provided through a tube. The anode is not fully covered electrolyte and has disconnection. That part is inter-connected to the cathode and connects with the anode from the next cell. [13] The advantages of the tubular design are no sealing problem, and reduction of shear stress.

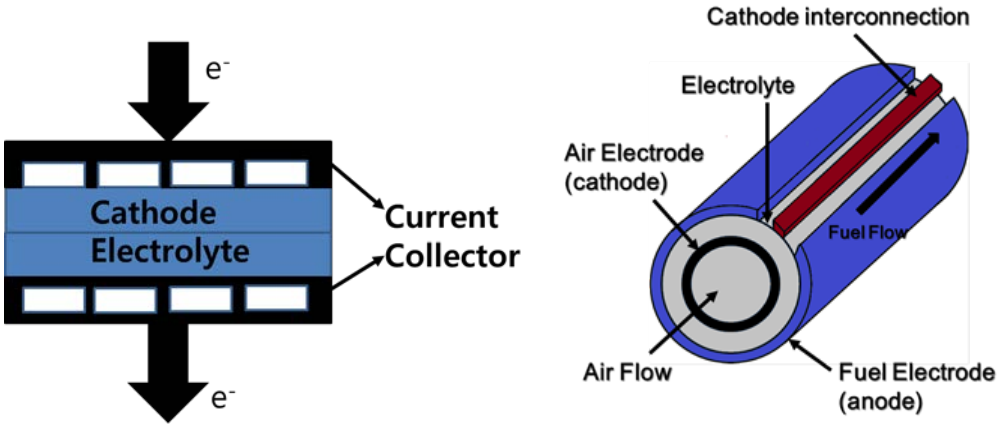

(a) (b)

Figure 3. Two types of solid oxide fuel cell stack design. (a) Flat planar design of solid oxide fuel stack (b) Tubular design of solid oxide fuel cell stack design

Among various types of fuel cells, the proton exchange membrane, also called polymer electrolyte membrane (PEM) fuel cells, offer many advantages which include high-density power, lower weight and volume, and lower operating temperatures which allow them to start quickly. [14-15] The characteristics of PEM fuel cells make them particularly suitable for potential power source applications ranging from centralized and distributed power generation to fuel cell engines for transportation and batteries for portable electronic devices. [16-17]

The polymer electrolyte membrane (PEM) fuel cells also known as proton conducting or solid polymer fuel cells (SPFCs) have ion conducting polymer as electrolyte and a catalyzed porous electrode and considered as the most promising type of fuel cells because their various advantages such as compact construction, large current density, solid electrolyte, low working temperature, and fast start-up. The electrode is bonded to the

electrolyte so the anode-electrolyte-cathode assembly is one item and very thin. The actual PEM fuel cells are membrane electrode assemblies (MEAs) which are series connection of single PEM fuel cells. Like AFCs, the mobile ion in the membrane is H^+ or proton. The operating temperature is typically low (80^oC). As the alkaline fuel cell, the electrodes are made from carbon with a platinum electro-catalyst. The PEMFCs are poisoned by carbon monoxide, so a complex and expensive fuel processor is required to convert practical hydrocarbon fuels into hydrogen and carbon dioxide, removing all traces of CO. [3, 12]

Typical, electrode reaction of PEMFCs is shown below. In the anode, supplied hydrogen decomposes into protons and electrons and protons moves to the cathode following ionic channels in the membrane, and electrons move to the cathode following external circuit. In the cathode, protons and electrons from the cathode and oxygen produce water. This reaction occurs continuously.

$$\text{Anode: } 2H_2 \rightarrow 4H^+ + 4e$$

$$\text{Cathode: } O_2 + 4H^+ + 4e \rightarrow 2H_2O$$

$$\text{Overall: } 2H_2 + O_2 \rightarrow 2H_2O + \Delta E$$

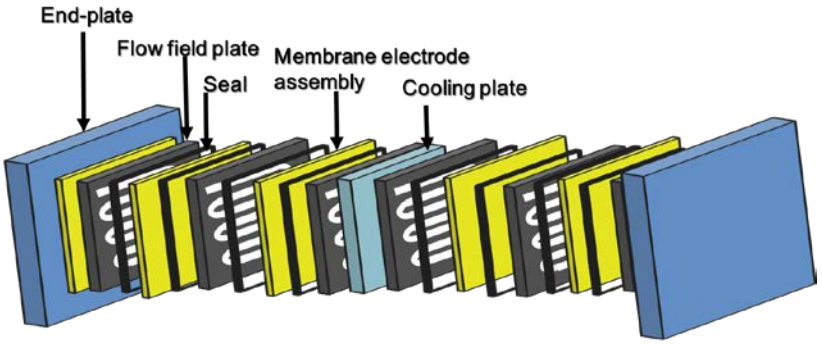

Figure 4. Stack configuration of proton exchange membrane fuel cell

The PEMFC stack configuration is the parallel connection of single cells, flow field plate (bipolar plate), and cooling plate as shown in figure 4 [18]. The bipolar plate has several functions in the fuel cell stack. [3, 18] They separate the single cells in the stack, distribute the fuel and oxidant in the stack, provide structural support, conduct heat from active cells to the cooling cells, and carry current away from the each cell [3, 18]. The topologies and materials have to satisfy these functions.

Topologies can include flow field, internal manifolding, internal humidification, and integrated cooling. [18] The requirements of materials for bipolar plate are the basis of chemical compatibility, resistance to corrosion, cost, density, electronic conductivity, gas diffusive/impermeability, manufacturability, stack volume/kW, material strength, and thermal conductivity. [18] Mainly two materials which are graphite-composite and coated metallic plates are satisfied the requirement of the bipolar plate. [3] For the maintaining proper operating temperature, the cooling plate is embedded to the stack. The air cooling is usually used for the small system and the water cooling system is used for large system. The PEM fuel cell stack generally several aspects are required. Most of all the reactants must be uniformly distributed to each cell. The second, the required temperature must be maintained in each cell. The third, the stack has minimum resistive loss. The forth, the reactant gas must be sealed. Finally, the stack has to have mechanical sturdiness. [3, 19]

1.2 Proton Exchange Membrane

Among a lot of elements of PEMFC stack, the heart of PEMFC is the polymer electrolyte membrane. Typically, the membrane is placed between catalyst electrodes and it acts as both the gas separator and proton conductor. As a separator, the membrane prevents

that the electrodes in a fuel cell from coming in contact with each other and provides the isolation between the fuel and oxidant gas streams which are essential for energy conversion in electrochemical reactions. As an electrolyte, the membrane acts as an ionic medium allowing the protons generated at the anode in the hydrogen oxidation reaction to migrate to the cathode where they are needed for the oxygen reduction reaction.

The Nafion which is perfluorosulfonate cation exchange membrane developed by E. I. du Pont de Nemours and Co is recently the most widely used because it has chemical and thermal stability, and high proton conductivity. [20] The construction steps of the electrolyte material are as follows. The first step is the perfluorination. This process is that the polyethylene is modified by substituting fluorine for hydrogen. The modified polymer from the process is called PTFE or Teflon. The second step is the sulphonate process. In this step, a side chain, ending with sulphonic acid HSO_3 is added into PTFE. The end of side chain is an SO_3^- because HSO_3 group is ionically bonded with PTFE. There is a strong mutual attraction between the cation and the anion because of the presence of SO_3^- and H^+. The result is that the side chain molecules tend to cluster within the overall structure of the material [3, 20]. The process is illustrated in figure 5.

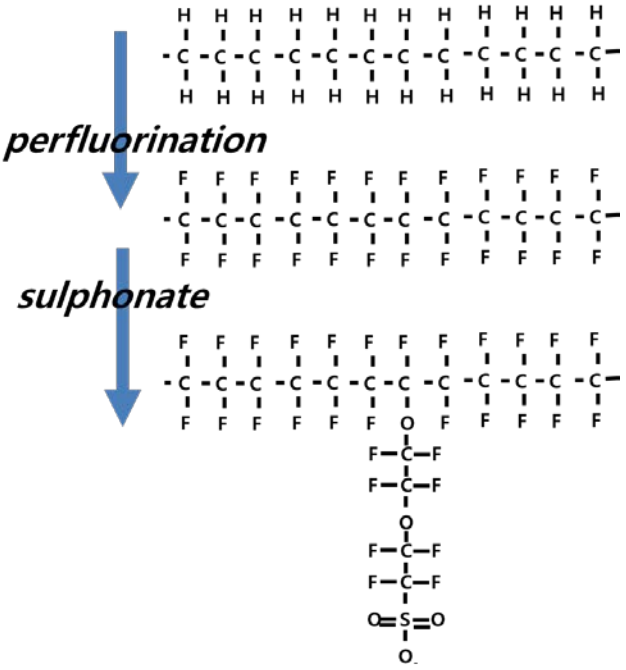

Figure 5. Synthesizing process of Nafion®

Because the sulphonated side chains are highly hydrophilic, one end of molecules mixes with water. The absorption of large quantities of water is brought to the hydrophilic region near the sulphonic acid group. Within this region, protons weakly attracted by the $SO3^-$ groups and they can easily move and dilute acid created. So, the membrane contains two different phases which are dilute acid region and strong hydrophobic structure. The chemical structure of Nafion® is given below.

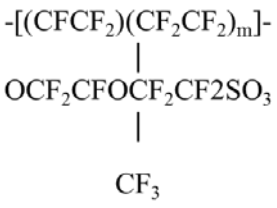

Since the uniqueness of the Nafion chemical structure due to phase separation such as

hydrophobic backbone and hydrophilic side chain, understanding of morphology of the Nafion is important. The morphological structure of the Nafion has been studied and debated since the 1970's. In that decade, the structure of ionomers models, the interpretation of ionic domain morphology, was established based on a small angle X-ray scattering experiment for studying for morphological characterization. [23, 24] The morphology of Nafion is described by these models which are a cluster-network model, modified core-shell, lamellar model, sandwich like model, and rod like model.

Gierke and co-works studied morphological structure of the Nafion in the unhydrolyzed sulfonyl fluoride precursor form, the hydrolyzed sulfonic acid form, and neutralized metal sulfonate form using small angle X-ray scattering (SAXS) and wide-angle X-ray diffraction (WAXD) [25, 26, 28]. From this study, they found crystalline organization within the fluorocarbon matrix from the un-hydrolyzed sulfonyl fluoride precursor form and it contained ionic cluster within a semi-crystalline matrix from the hydrolyzed sulfonic acid form [26]. Also, other groups' result also showed ionomer peak intensity variation and shift water contents by SAXS and WAXD results. [25-27]

Based on these studies, they insisted that the ionic cluster model is the best description of the water swollen morphology of Nafion®. [25-30] From the ionic cluster model, the ionic cluster is roughly 2 nm radius spherical shape with an inverted micellar structure as shown in figure 6. They proposed that the spherical ionic clusters are interconnected by 1 nm diameter narrow channels, the ionic cluster network, in considering of the high ionic permselectivity and the requirement of a percolation pathway for ionic transport in the Nafion.

A schematic of the cluster network model is as shown in figure 6. However, it is not

the best description of actual morphology of the Nafion because the geometry of cluster adopts an expedient such as spherical shape for the ionic cluster [25]. Also, the other studies including transmitting electron microscopy did not show actual geometry of the cluster. Thus, there are no experimental evidences of the existence of the ionic channels and clusters. Nevertheless, the model did provide a crude picture of the microscopic morphology of the Nafion it has been improved in subsequent years by others. [25]

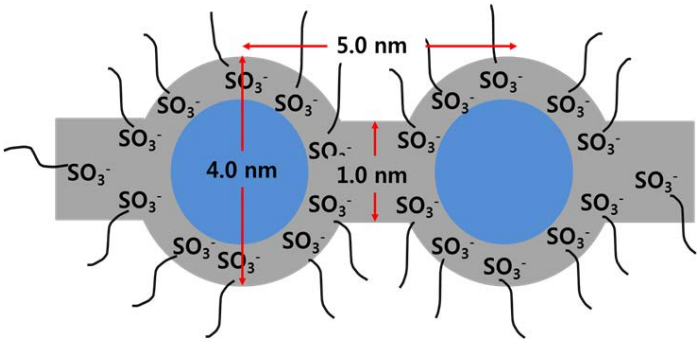

Figure 6. Cluster network model of the morphological structure of Nafion®

Fujimura and co-works studied the origin of two maxima known from the study of the Nafion morphology and the origins of the ionomer peak using SAXS and WAXD. The two maxima from the different origins are that the scattering maximum at small angles and the scattering maximum at large angles, relatively which can be assigned to interface between crystalline structures and can be assigned to the ionic cluster [19]. The result agrees well with the previous scattering studies except finding of the sulfonate form of ionomer, ionic cluster, at dry state and microscopic degree of swelling was found rather than

macroscopic degree of swelling as the water contents increases. [23-25]

Based on their study, Fujimura et al. conclude that the core-shell model is the best description of the Nafion morphology. Figure 7 illustrates the core shell model. In this model the ionic cluster consists of two phases such as the core and shell. The ion-rich core is surrounded by the ion-poor shell which consists of perfluorocarbon chain. The core-shell particles are distributed on the in a matrix of fluorocarbon chain [23-25].

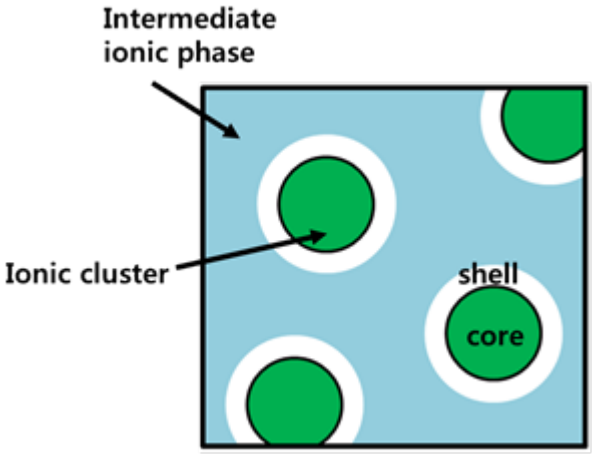

Figure 7. Core shell model of the morphological structure of Nafion®

During the swelling and de-swelling process, the morphological and dimensional changing of the Nafion was observed from the SXAS analysis. Based on the observation, the cluster network model and the core-shell model were proposed. However, the explanations are required for the linear variation of Bragg spacing changing with water content and recoverable plastic flow in swelling/de-swelling. Thus Litt proposed a reevaluation of Nafion

morphology, lamellar model. [25, 26] Litt showed that the d spacing is proportional to the volume of absorbed water. [25, 26]

By this observation, Starkweather suggests bilayer structure of Nafion morphology. [27] In this model, the ionic domains are defined as hydrophilic “micelle” layers separated by thin, lamella PTFE-like crystallites. As water absorbs between the lamella and separates them, the increase in d spacing between ionic domains is expected to be proportional to the volume fraction of water in the polymer and the swelling behavior should be completely reversible, thus eliminating the requirement of morphological reorganization.

The lamellar model provides a simple and convenient explanation of the swelling morphology of the Nafion, However, the lamellar model is over simplified since Litt ignored low maximum from the crystalline which is inter-lamellar long spacing. [25] Also, the other studies showed that the inter-lamellar long spacing is not identical with inter cluster spacing. [28] Recently, a modified model was proposed based on the lamellar model by Houbold et al. They proposed a sandwich model by synchrotron SAXS studies using acid form of the Nafion® 117 samples. [25, 29]

In this result, the scattering cross section data is fitted to a layered model whose basic structure element is a sandwich as sown figure 8. The outer portion of this sandwich consists of the side chains, including the sulfonic acid groups (shell region), and inner liquid portion consists of the water/methanol molecules (core region). Using the model fit, they calculate lateral dimension a and b and total thickness (core (c) + shell (s) region) of the model. Then a and b is between 15 and 45 Å and total thickness is about 60 Å. From their result, c and s thickness varies as concentration of methanol in the water. In the methanol swollen membrane, core the region becomes smaller and shell region is extended. [29]

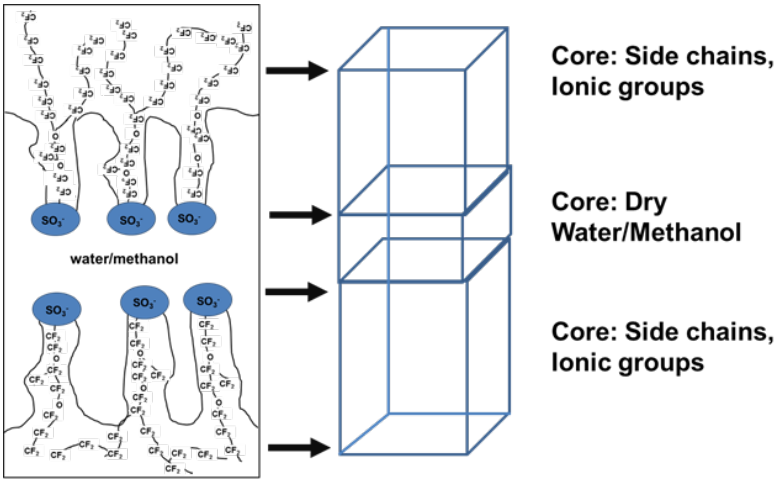

Figure 8. Sandwich model of morphological structure of Nafion®

Gebel et al. studied the structural evaluation of the Nafion from dry state to swollen state by SAXS and SANS. The result reveals several things in the swelling and de-swelling process. First, a structural inversion occurs at 0.5 water fraction. Second, the structure of the Nafion® varies with the amount of water contents. At low water contents, spherical domains of water is embedded in the polymer matrix and at high water contents, the structure is a connects the network of polymer rods. [35] Based on the small angle analysis and energetic consideration, he proposed the conventional swelling and de-swelling mechanism.

The mechanism is illustrated in figure 9. In the dry membrane, the spherical ionic clusters are distributed on the membrane. The diameter of each cluster is 1.5 nm and center to center distance of two clusters is 2.7 nm. With absorption of water, the clusters become spherical water pool for minimizing the interfacial energy between polymer and water as shown in figure 9. The diameter of the spherical water pools is 2nm and inter aggregate distance is 3nm. In this case, the inter-aggregate distance refers that each cluster still

separated and ionic conductivity is extremely small. Between 0.3 to 0.5 water fractions, the spherical ionic domains are connected with cylinders of water dispersed in the polymer matrix. As the diameter of the ionic domain increases from the 4nm to 5nm, ionic conductivity is also increased. At 0.5 water fractions, the structure is inverted and then network of rod-like polymer aggregate appears. Between 0.5 and 0.9 water fraction, the connected rod-like network swells. Due to increasing of the water swollen, the distance between rods is decreased. Thus, the overall number of rods is decreased. [25, 35]

Nevertheless this model explained well the swelling and de-swelling mechanism. There is no thermodynamic justification for phase inversion process at 0.5 water fraction. Also, they did not explain the drastic change near phase inversion point. [25] Further study was done by Rollet and Lubatat. [25, 36, 37] Rollet et al. studied phase behavior in the hydrated Nafion by SANS. Based on the observation, he concluded that the best description of the hydrated Nafion is that aggregated polymer surrounded by water. [25, 35]

Lubatat studied hydrated Nafion® by SAXS and SANS. This study supported the assumption that the swelling process simply involves a dilution of the scattering entities as suggested earlier by Gebel. The result indicated that the structure between 1 nm and 100 nm of the Nafion can be described in terms of elongated polymeric aggregates connected at larger scale to form a film. During the water swelling process two separated regimes were found in agreement with the result of Litt et al. The elongated polymeric aggregate is coherent with the evolution of the structure as a function of the water content change to solution. [25, 37]

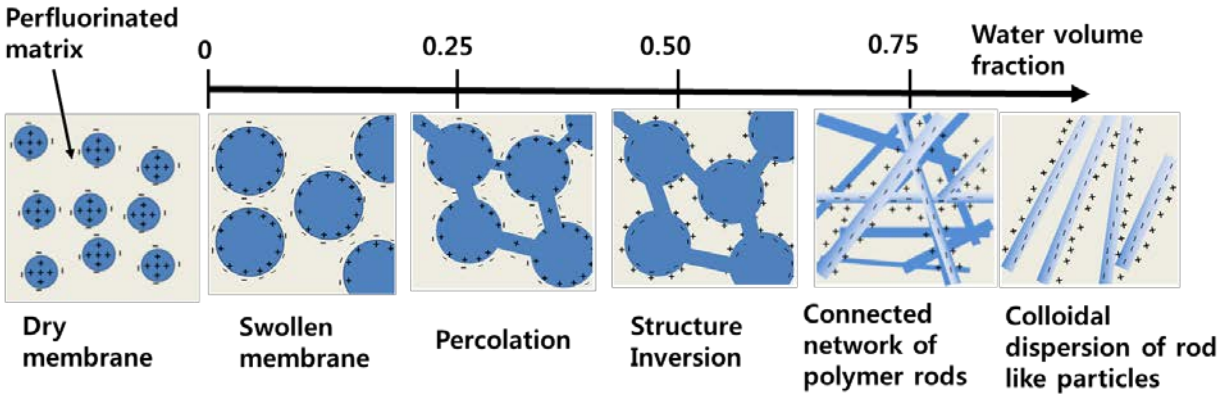

Figure 9. Rod like model of morphological structure Nafion®

The most widely accepted microscopic morphological model of Nafion® is the water channel model which was proposed by Klaus et al. The water channel model was established based on the simulation. Using the previous SAXS, WASX, and NMR data, he calculated the morphological structure of Nafion® by numerical fast Fourier transformation method. [34] This model explains good proton conductivity and mechanical properties of Nafion well. The structure of ionic channels is cylindrical inverted micelles. The ionic channels are parallel with their neighbor. The densely packed ionic channels are stabilized by the relatively straight helical backbone segment as shown in figure 10. The diameter of water channel distributed between 1.8 nm and 3.8 nm with an average 2.4 nm. The channel diameter of the water channel model is relatively larger than other models. The relatively large diameter in the water channel model can explain good proton conductivity of Nafion well. The diffusion of water in Nafion at H_2O = 20% is only one order of magnitude slower than in bulk water. The previous models could not explain the diffusion of water in Nafion® at 20% because in relatively narrow channels, the significant obstacles to water diffusion presents. The ionic

channel diameter in the water channel model is relatively wide compare with other models. The relatively wide, parallel channels have a large hydrodynamic component of water/methanol transport.

The crystallites, which are repeated at 10-20 nm, are crucial component of the structure of the Nafion membranes. The repeat is perpendicular to the chain axis, given that the scattering intensity is on the equator for oriented Nafion samples. The thickness of crystallite is 2-5nm and the cylindrical crystallite is elongated. The crystallites are physically linked with backbone and give good mechanical properties in the membrane. The crystallites are 13% of volume in the membrane. Even though the water channel model explains well good proton conductivity and mechanical properties of Nafion, the experimental evidences for the model is not enough.

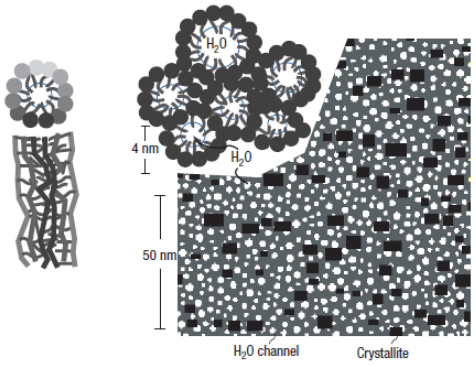

Figure 10. The Water Channel Model of morphological structure of Nafion® [38]

1.3 Aging Mechanism of the Nafion Membrane

Over the past decade, the significant progress of highly efficient and reliable technologies of PEMFC has been achieved. [1, 3, 5, 6, 12, 22, 39-48] However, there are still many technical and economic barriers such as relatively high cost, lack of durability, and reliability of wide operating conditions. [49] One of most important technical barriers is the durability of PEMFCs under a wide range of operating conditions. For different applications, the requirements for fuel cell lifetime vary significantly, ranging from 5000h for cars to 20000h for buses and 40000h of continuous operation for stationary applications. For automobile, because of harsh operation conditions of dynamic load cycling such as frequently startup/shutdown and freeze/thaw, the goal is very challenging for current fuel cell technology. [12]

The PEMFCs are structurally stable system because it does not have mobile parts. So degradation of its component is crucial for stability of fuel cell system. [12] Among many components of fuel cell, the polymer electrolyte membrane is most essential component. The durability and reliability of membrane are strongly depending on the membrane aging. So, understanding of the membrane aging is crucial to solve the rack of durability and reliability of the PEMFC. The aging is classified as thermal, mechanical, and chemical aging.

The mechanical aging is related to failure of each element of the PEMFC. Major failure is a result of the membrane imperfection, catalyst migration, and electrode and electrolyte interface decomposition. [12] They usually occur as a result of congenital membrane defects and the improper membrane electrode assembly fabrication process. The local areas corresponding to the interface between the lands and channels of the flow field or the sealing edges in the PEMFC, which are subjected to excessive or non-uniform

mechanical stresses, are also vulnerable to small perforations or tears. Overall dimensional changes under various humidification conditions also contribute to performance deterioration while the fuel cell is operating. Also, this mechanical aging induces the chemical and thermal aging. For instance, the gas crossover in the membranes increases when the membranes have a small amount of pinholes. The increasing of the gas crossover induces the chemical aging of the membranes. So it can be ameliorated by improving the membrane fabrication condition and the fuel cell assembling process. Thus, understanding mechanical aging process is very important to prevent the failure and improve the manufacturing process of the Nafion®.

Cleghorn et al. did a life time test of the PEMFC under high humidification. The PEMFC continuously operated under 70^{o}C and 100%RH. The result was that 66% of the original cathode electrochemical area was lost due to increasing transport losses in the fuel cell. [36] The MEA performance was tested under mid humidification, non-saturated humidification, by Jingrong Yu et al. [51] The experiment was conducted under 75^{o}C and fully humidified H_2 and air at 70^{o}C. The result showed a decrease of active surface area of Pt catalysts became the cause of significant increment of H_2 crossover. [51]

Several studies of PEMFC were performed under low humidification. They reported that the decreasing of cell performance occurs between membrane cell interfaces. Eiji Endoh et al. reported that carbon radicals generated under continuous operation will become a reason of cell failure. [52] Jingroung Yu et al. showed that agglomeration of Pt particles is due to the cell degradation. [51] The constrained membrane in an assembled fuel cell experiences in-plane tension resulting from shrinkage under low RH and in-plane compression during swelling under wet conditions.

Local pinholes and perforations are the crucial reason of physical aging of the membrane. The pinholes are produced during fuel cell operating process. Mechanical stress induces degradation at weak part of the membrane because of wet/dry cycling of the fuel cell. As a result of the degradation, the pinholes in the membranes are created. [51] A several studies report that even development of single pinhole affects cell performance. The pinholes caused by degradation creates a hot spot (temperature of hot spot is 4-5K higher than surroundings) and the hat spot causes a significant performance drop. After creation of the pinholes, if this happens, hydrogen diffuses through the pinhole and creates hydrogen oxide at the cathode. Then, a local hotspot is created and cell performance drops. [53-55] The results of Huang et al. suggested that mechanical failure of the membrane starts as a random, local imperfection that propagates to catastrophic failure. [56]

Usually, the chemical aging is due to the chemical attack by peroxide ($HO^{\cdot}$) and hydro-peroxide ($HOO^{\cdot}$) radicals from the chemical reaction on the anode and cathode catalysts. These radicals react with the membrane backbone and break H-F bonding. As a result of the radical attack, the membrane becomes thinner and the pinholes are created. Eventually, the membrane performance is decreased. In low humidity condition, the membrane degradation is accelerated under open circuit voltage (OCV). [12] This process is listed below.

$$\text{Rf-}CF_2COOH + HO\cdot \rightarrow \text{Rf-}CF_2 + CO_2 + H_2O$$

$$\text{Rf-}CF_2\cdot + HO\cdot \rightarrow \text{Rf-}CF_2OH + \text{Rf-COF} + HF$$

$$\text{Rf-COF} + H_2O \rightarrow \text{Rf-COOH} + HF$$

Many research groups proposed the radical formation mechanism. [57-59] The researches showed the radicals formed the anode [47], the cathode [48], or both. From the

study of Hong Wang et al. the hydro peroxide is produced at the anode by oxygen crossover. Minoru et al. introduced hydro peroxide forming both anode and cathode. Under OCV, hydro peroxide formed at the cathode. The reaction is

$$O_2+2H^++2e\rightarrow H_2O_2$$

The hydro-peroxide makes that the membrane decomposes at the cathode site and then oxygen partial pressure drastically is increased due to the increasing of decomposition. Thus, oxygen crossover is increased and the peroxide is produced at the anode voltage. [59] Also, the existence of metal ions such as Fe^+ and Cu^+ creates a more severe effect of decomposition of the membrane. These metal ions act like catalyst and produce the peroxide radicals which are most reactive species. [59] The forming of the peroxide by the metal ions are givens as

$$H_2O_2+Fe_2+\rightarrow HO\cdot+OH-+Fe_3+$$

$$Fe_2++HO\cdot\rightarrow Fe_3++OH^-$$

$$H_2O_2+HO\cdot\rightarrow HO_2\cdot+H_2O$$

$$Fe_2^++HO_2\cdot\rightarrow Fe_3++HO_2^-$$

$$Fe_3^++HO_2\cdot\rightarrow Fe_2^++H^++O_2$$

Previous studies about the aging mechanism provided precious information to prove optimizing the design of the fuel cell and choosing operation conditions. However, the fundamental understanding of the aging process is required to slow down degradation and improving durability of the membrane.

Over the past decade, many studies report that thermal aging is related to the decomposition ether backbone, side chain, or both in the membrane at high temperatures. Surowiec and Bogoczek reported that the Nafion begins to decompose via its side sulfonate

acid groups at 280^{o}C from the study of the thermal stability of the Nafion which was investigated by using thermal gravimetric analysis, differential thermal analysis, and Fourier transform infrared spectroscopy. [60] A similar mechanism is proposed by Wilkie et al [61]. From the study of Bauer et al. the back bone of the Nafion starts to decompose around 400^{o}C. [62] However, understanding of the membrane aging under low temperature is crucial due to proper working temperature of the PEM between 60^{o}C and 80^{o}C for promising the maintaining well-hydrated PFSA. Also, around glass transition temperature (80^{o}C) membranes, the critical breakdown of membrane is pronounced.

The stability of the polytetrafluoroethylene (PTFE)-like molecular backbone below 150^{o}C has been well known because of the C-F bond and the shielding effect of the electronegative fluorine atoms. [63] From the study of F.M. Collette, when the Nafion membrane annealed between 80^{o}C and 120^{o}C in the water, 80% of conductivity dropped off at 80 days. [64] The NMR result from the Collette's study shows the SO_3H group of membrane loss. The results supported as result the decreasing of band at 1060 cm^{-1}, corresponding S-O stretching. Moreover, the intensity and the frequency of the band at 1630 cm^{-1}, corresponding to the bending frequency of water, decreased with aging time whereas the frequency of the band at 3500 cm^{-1}, corresponding to the stretching frequency of water, increased with aging time. The observation of these water absorbance bands (1630 and 3500 cm^{-1}) leads us to conclude that the strength and the number of the hydrogen bonds decreases upon aging. As anhydrides are much less hydrophilic and polar than sulfonates, less water is absorbed by the polymer and the hydrogen bonds formed between sulfonic anhydrides and water are weaker compared to those formed with sulfonic acid. The conclusion of the study is that the chemical structure of Nafion membrane changes to sulfonic anhydrides formation,

creating a crosslink between two side chains. This leads to the decrease of the polymer hydro-philicity with a proton conductivity drop off. [64]

From the study of Alexandra Alentiev, chemical composition changes of the Nafion were studied by FTIR. The Nafion® was thermal treated at 95^{o}C. The bands at 1440cm^{-1}, which can be attributed to the vibration of ether (–$S(O)_2$–O–) groups, are absent in native Nafion®. Also, the Nafion film, which was stored for 14 years, shows same result. Apparently, sulfo-ethers and cross-linking can appear during storage, exploitation and thermal treatment. [65] Liang et al. studied Nafion® 115 which is thermal treated at 40^{o}C, 120^{o}C, 150^{o}C, and 180^{o}C respectively for 1.5h. The result was analyzed by FTIR. From the study, thermal treated Nafion membranes show that the macromolecule remains micelle structure and SO_3H is free from the surrounding of the main chain.

Thermal treatment causes the membrane to change in structure and physical properties. At temperature above glass transition temperature, side chain movement brings the -SO_3H group out of the bulk to the surface to decrease the surface energy. [66] Yuji Shibahara et al. reported that sulfonic acid side chain decomposed around 100^{o}C, which is near glass transition temperature. [67] The thermal aging process of Nafion 117 membrane was analyzed with age moment correlation (AMOC) method and the four-electrode AC impedance method. The membrane was thermally treated at 373 K for 12 hours. In the lifetime spectra and the FT-IR spectra of the heated and the non-heated samples, significant difference does not find from both samples. However, the overall S-parameter, which is the ration of the area of the central region of the photo peak and the total photo peak area, was increased by heating. The S-parameter from the AMOC data is directly related annihilation process of the samples. So the increase of overall S-parameter was found to be the increase

of direct annihilation of positrons with low energy electrons. This result manifest that the decreasing of proton conductivity is caused by hydrogen bond and chemical bond affected production of the sulfonic radicals. The AMOC data refers that pick-off annihilation occurs in space forming by the backbones and side chains. This can be possibly explained by several reasons. The first, the inverted micellar structure is formed in Nafion. The second estimated averaged spherical space diameters for the heated and the non-heated samples were close to each other and the evaluated lengths were about 0.74 nm, which is similar to the length of side chains. The third, the S-parameter corresponding to the pick-off annihilation showed good agreement between both samples. [67] Nevertheless many studies [61-67] reported the sulfonic acid side chain decomposition due to thermal annealing other studies [59, 75-85] reported the structural changes without the sulfonic acid side chain of the Nafion.

In spite of many efforts to understand thermal aging mechanism of the Nafion, the aging mechanism of the Nafion® near the glass transition temperature have been still incomprehensible and many explanation about the Nafion thermal aging are co-exist such as decomposition of the sulfonic acid side chain and the surface reorganization without decomposition of the side chain.

The aging of the Nafion membrane induces significant failure on the membrane. The mechanical aging of Nafion is mostly related imperfection of membrane such as crack, perforation, pinhole due to improper manufacturing process. The mechanical aging is usually causes of catastrophic failure at early life. Also, the mechanical aging induces chemical and thermal aging. The chemical aging process is due to backbone decomposition in the membrane by peroxide or hydro-peroxide attack. The decomposition of the backbone induces serious failure of PEMFC. The peroxide or hydro-peroxide is chemically reacting with

carboxylate, which is impurity in the backbone of Nafion®. Thus, carboxylate groups cause of the chemical aging. The carboxylate groups are attacked in the PTFE is during the membrane synthesizing process. The mechanical and chemical aging strongly relate to the manufacturing process. Thus, the failures PEMFC due to mechanical and chemical aging of the Nafion® can be mitigated by optimize the synthesizing or manufacturing process of the Nafion®.

Thermal degradation of a PEM is directly related to the structure and the fundamental properties of the membrane. The membranes are operating at certain temperatures or going through temperature cycles that are close to their glass transition temperatures reveal accelerated degradation behaviors. The significant structural changes, including decomposition of sulfonic acid chains and morphological changes of the ionic channels were observed during the thermal aging by many studies. [61-68] Thermal aging is usually induced by the PEMFC operating because operating temperature of the PEMFC is close to the glass transition temperature of the Nafion. Thermal aging is closely related microscopic structural variation in the membrane. Thus, the mitigation of the thermal aging of Nafion is impossible without a fundamental understanding of the microscopic morphological structure of the Nafion®.

CHAPTER 2

EXPERIMENTAL SETUPS

In this chapter, I will give a detailed description of the experimental setups and experimental techniques used in this study. I will first describe atomic force microscopy (AFM). Then I will describe the details of a current sensing microscopy (CSAFM) and humidity control system. Finally, I will describe the experimental procedure.

2.1 Atomic Force Microscope

The revolutionary development of the Scanning Tunneling Microscope (STM) has given rise to an entire family of Scanning Probe Microscopes (SPM). [69] These atomic resolution instruments are differentiated by how the probe tip interacts with the scanned surface. The Atomic Force Microscope (AFM) is the most widely utilized member of the SPM family. With AFM, a tip mounted on a micro fabricated cantilever scans a substrate; the interaction between the tip and the substrate causes the cantilever to deflect. [69] The deflection of cantilever was quantified by the measurement of a laser beam which is reflected from the end of cantilever to a position sensitive photo detector (PSPD), as shown in Fig 11. The cantilever can be directly attached to a XYZ scanner which is made of piezoelectric materials so that the tip can move in three dimensions with sub-nanometer resolution. The scanner can also be attached to the sample stage directly. In this way, instead of scanning the tip, a sample is moved in the horizontal direction (X-Y direction) and in the vertical direction (Z-direction) by the scanner. While the scanner scans line by line, the feedback loop which controls vertical movement of scanner was controlled by signal from the PSPD. In addition

to high-resolution topography, a variety of other signals can be collected from the AFM tip. [70]

An Atomic Force Microscope (AFM) can be operated in a number of different modes, depending on the application. The primary modes of operation are contact and non-contact modes. In contact mode the AFM tip makes soft physical contact with the sample. As the tip approaches the sample surface the inter-atomic forces become very strongly repulsive and since the cantilever has a low spring constant, the forces will cause the cantilever to bend following the topography of the sample. Therefore, the detection of the position of the cantilever leads to a topographic map of the sample surface. In a contact mode, AFM can generate the topographic data set by operating in one of two modes: constant-height or constant-force mode. In constant height mode the spatial variation of the cantilever deflection can be used directly to generate the topographic data set as the scanner height is fixed during the scan. In the constant mode the deflection of the cantilever can be used as an input to a feedback circuit that moves the scanner up and down in Z, responding to the topography by keeping the cantilever deflection constant. [71]

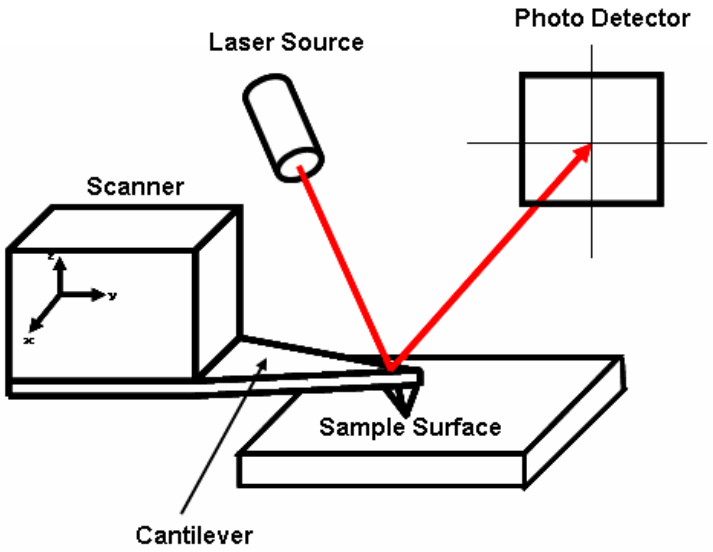

Figure 11. Schematic of an atomic force microscope

2.2 Current Sensing Atomic Force Microscopy

Current sensing atomic force microscopy (CSAFM), a novel AFM technique, can be used to probe simultaneously the surface morphology and the local conductance variation of a sample. The essential component in a CSAFM, aside from those in conventional AFMs, is a sensitive electric current measuring loop which connects a conducting probe tip and the sample. The probe tip is usually a conventional AFM tip coated with a uniform metal layer which acts as the current sensor. As a CSAFM probe tip scans across the surface of a membrane in contact mode, the tip traces out the surface morphology and, at the same time, senses current flow between the contact of the tip and the plane electrode on the other side of the membrane, generating simultaneously a surface morphology and current sensing images. The sensed current depends sensitively on the contact between the probe tip and conductivity in the membrane. Figure 12 shows the simple schematic of CSAFM which used in this study. CSAFM has 10^{-12}A sensitivity in current measurement. AFM tip is coated with uniform a Pt

layer.

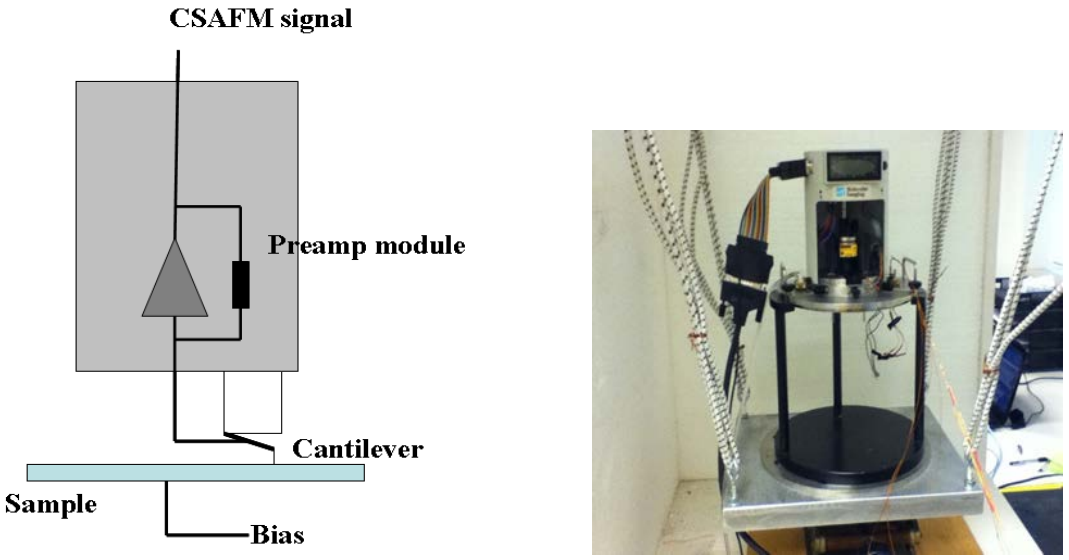

(a) (b)

Figure 12. The current sensing atomic force microscope used for this work. (a) Preamp module added to a conventional AFM displayed figure 12 (b). (b) Pico Scan CSAFM system.

2.3 Humidity Control System

Relative humidity (RH) in the environmental chamber can be controlled using the humidity control system. The humidity control system is constructed of the series connection of the dry air inlet and the water vapor supplier as shown in figure 13. The Honywell HIH-4010 humidity sensor is used as measuring accurate RH. The accuracy of the sensor is ±3.5% RH. RH controlling procedure is following several of steps. First, from the water vapor supplier, sufficient water vapors are produced by boiling of the distilled water. Second, the water vapors are pushed into the environmental chamber by dry air flow from the dry air inlet.

When the RH in the environmental chamber reaches the proper value, inflow of water vapor stopped.

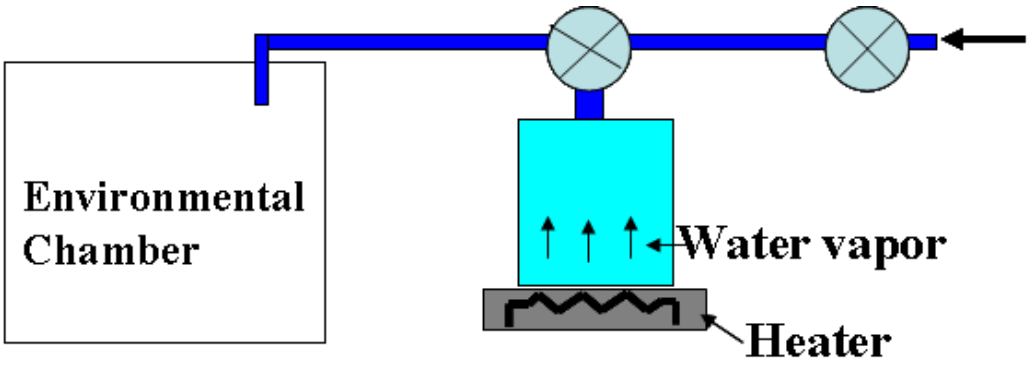

Figure 13. Schematic of humidity control system

2.4 Experimental Procedure

In this study, two types of the proton exchange membranes, which are Nafion®115 and Nafion® 212, were used. Table 1 shows basic mechanical, electrical, and other properties of both membranes. The names, Nafion® 115 and Nafion® 212, contain specific information about the membranes. The first two digits in the name following Nafion multiplied by hundred represent the equivalent weight of the membrane. The equivalent weight (EW) of Nafion is determined by the average distance between the side chains along the backbone, and is defined as the number of grams of dry polymer per mole SO^3 [25]. For instance, 11 from the Nafion 115 reveal 1100 equivalent weight. The last digit in the name following Nafion® multiplied by ten represents thickness of the membrane. For instance, 5 from the

Nafion® 115 is 50 micro inches. The Nafion® 115 has thicker than Nafion® 212; the thickness of Nafion® 115 is typically 127μm and Nafion® 212 is typically 50.8μm. The conductivity of the both membranes is 0.1 Scm^{-1}. Nafion® 115 has better mechanical properties compared to Nafion® 212 because the tensile strength of Nafion® 115 is 46 MPa and Nafion® 212 is 23 MPa. Both membranes have roughly same specific gravity. Specific gravity is the ratio of the density (mass of a unit volume) of a substance to the density (mass of the same unit volume) of a reference substance. Nafion® 212 has larger sulfonic acid groups compare with Nafion® 115 because equivalent weight of Nafion 115 membrane is 1100 and 212 membrane is 2100. Water content of Nafion® 115 is 5% and Water uptake is 38% and Water content of Nafion® 212 is 5.0±3.0% and water uptake is 50.0±5.0%. All properties of Nafion 115 and 212 are measured at 50% RH and 23^{o}C.

	Thickness (μm)	Conductivity (Scm^{-1})	Tensile Strengths (MPa)	Specific Gravity	Equivalent Weight (g/mol)	Glass Transition Temperature (^{o}C)
Nafion 115	127	0.1	46	2.98	1100	90-150
Nafion 212	50	0.1	23	2.97	2100	90-150

Table 1 Mechanical and chemical property of the Nafion® 115 and Nafion® 212 membranes

In this measurement, the current sensing atomic force microscope (CSAFM) was used for obtaining information of the proton conductance and the ionic cluster variation in the Nafion 115 and Nafion 212 membranes during thermal aging. Figure 15 illustrates the

experimental setup of the current sensing atomic force microscope for this study. A pristine Nafion membrane is gently adhered to a sample holder using conductive carbon paint. The carbon paint is used for two purposes: one is adhesion to a membrane and a sample holder and another is applying bios voltage to the membrane. The membrane is placed on a heater which is embedded in a sample stage. The schematic of sample holder is as shown in figure 14.

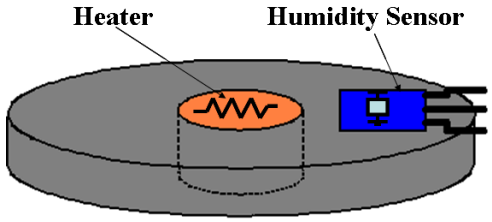

Figure 14. Schematic of a sample holder

The sample holder which includes Nafion membrane is installed into CSAFM. The Pt coated tip and the catalyzed membrane consist of the mini fuel cell as shown in figure 15. An ionic current can flow from the AFM tip across the membrane reaching the electrode on the opposite of the membrane. As the CSAFM tip scans on a membrane surface, the directly detected ionic current probes the ionic conducting properties in the local region of the membrane in contact with the AFM tip. Conductance images, which are obtained using the CSAFM on a Nafion®, reveal local ionic conductivity variations on the membrane. In this configuration, the Pt-coated tip works as a catalyst and an electrode. As a catalyst, the Pt-

coated tip supplies protons into the membrane by oxidization of hydrogen.

The electrolysis of water is used for supplying fuel into the mini fuel cell. The electrolysis is performed applying by DC 1.5 V to the tip and the membrane. In order to verify the performance of the mini fuel cell, three different mini fuel cell configurations were tested: the non Pt-coated tip and the catalyzed membrane, the Pt-coated tip and the non-catalyzed membrane, and the Pt-coated tip and the catalyzed membrane. Figure 16 (a) is a result of the performance of the fuel cell with the non-Pt coated tip and the catalyzed membrane. In this setup, the conductance on the membrane is under the resolution limit of the CSAFM system. The result indicates that the mini fuel does not work because there is no catalyzing reaction at the tip. Figure 16 (b) is a result of the performance of the mini fuel cell with the Pt-coated tip and the non-catalyzed membrane. In this setup, the fuel cell also does not show any performance because of no catalyzing reaction at the catalyst layer next to the cathode. Figure 16 (c) is a result of the performance of the fuel cell with the Pt-coated tip and the catalyzed membrane. The image from this setup well displays local conductance variation on the membrane. These results clearly show that the mini fuel cell with the Pt-coated tip is the effective method to study the membrane.

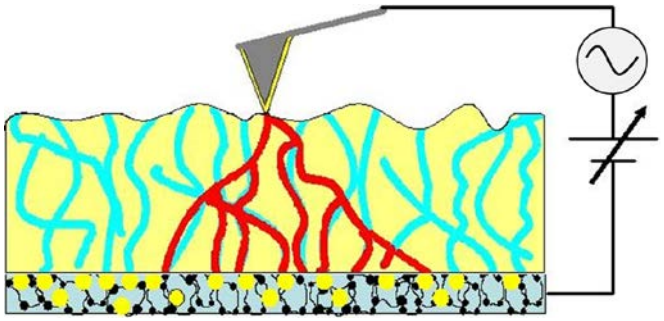

Figure 15. Schematic of CSAFM in measurement

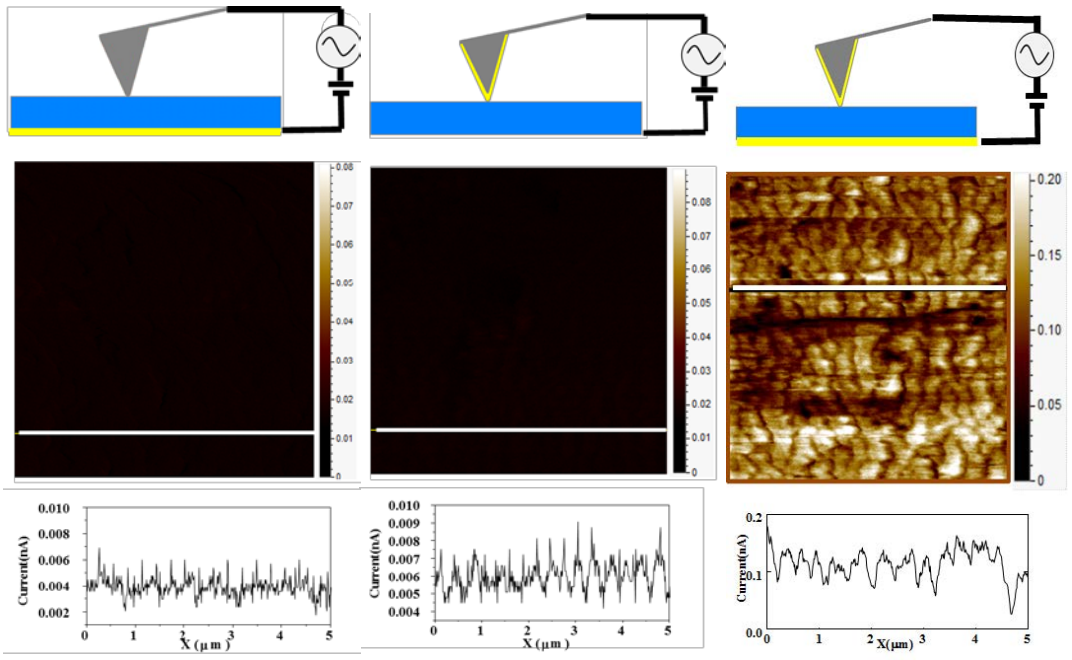

(a) (b) (c)

Figure 16. Different configurations for mini fuel cell performance test. (a) The figures illustrate the mini fuel cell configuration which consists of the non-Pt coated tip and catalyzed membrane (top), a corresponding current sensing image (middle), and line profile (bottom). (b) The figures illustrate the mini fuel cell configuration which consists of the Pt-coated tip and non-catalyzed membrane (top), a corresponding current sensing image (middle), and line profile (bottom). (c) The figures illustrate the mini fuel cell configuration which consists of the Pt-coated tip and catalyzed membrane (top), a corresponding current sensing image, and line profile.

The samples were prepared in two steps in this study. The first step is that each sample is annealed at four different temperatures: 90°C, 100°C, 110°C, and 120°C. During the annealing process, the sample stage with the Nafion membrane is covered by an aluminum foil cap for maintaining constant temperature around the membrane. Then the membrane on the stage is placed to the environmental chamber and annealed at the proper temperature. In the second step is that the membrane is for cooled at least two hours in the environmental chamber after heater is turned off.

The humidity in the chamber is adjusted to 50% RH using the humidity control system. After RH stabilized at 50%, CSAFM obtained 5x5 μm topographic and current sensing images simultaneously. This cyclic process, annealing and measuring, was done until the conductance of the membrane became zero.

CHAPTER 3

EXPERIMENTAL RESULT

This experiment focused on the changing of the ionic channel network of the Nafion membrane due to the thermal aging process. For studying the thermal aging, the membranes were annealed at four different temperatures (90^{o}C-120^{o}C) until the membrane conductance approached to zero.

The series of images (from the 17 to 106) show the development of conductance variation of the Nafion 115 and Nafion 212 membrane surface at each thermal annealing temperature. There are about 10 images of each membrane at each temperature (90^{o}C-120^{o}C); they are labeled accordingly in the list of illustrations. The (a) and (b) from each figure indicate the conductance image (a) and the topography (b) by the CSAFM. The color bar in the (a) is a display the magnitude of the conductance (current, nA). So, the bright color indicates the high conductive region and dark color indicate the low conductive region. The conductance image expresses well the heterogeneous structure of the Nafion membrane due to phase separation as hydrophobic backbone and hydrophilic side chain. The bright color reflects the high density of the ionic clusters and dark color shows the low density of ionic cluster on the membrane surface. The color bar in the figure (b) is display the magnitude of the membrane height. The color changing from the dark to bright indicates the height changing from low to high region.

The images were a result of the contact mode AFM in which a constant force was applied to the membrane during the scanning by adjusting the vertical position of the probe tip. The mechanical stiffness variation caused by the heterogeneous structure of the

membrane does not affect the images because typically the effective contact area between the tip and the membrane is larger than the size of a typical ionic cluster (or domain) on the membrane. Constant contact area between the tip and the membrane surface was mostly maintained during the imaging process. Thus, the current sensing would reflect the variation of local conductivity on the membrane surface, and the variation is directly related to the ionic connection between the probe tip and the electrode across the membrane [68, 69].

Figures 17, 31, 45, and 55 are the pristine Nafion 115 membranes. Both the conductance and the topographic images of the membrane do not show any structural unity. Also, each conductance and topographic image do not show any relation. Thus, the convolution effect by the tip is ignorable of the study. The convolution is that the tip image is projected into an AFM image. The ionic cluster network structure of the pristine membrane should be randomly composed, which can be shown at the current sensing images (17, 31, 45, 55 (a)). The four different images do not show any structural resemblance. This is due to the quasi-crystallinity and the randomly close packed ionic clusters expressed from the water channel model. The maximum current of the pristine Nafion 115 membrane is roughly 0.5 except in figure 17 (a). The reason of the comparably low maximum current of figure 17 (a) might be due to an imperfection of the membrane during the manufacturing process. The topographic images (17, 31, 45, 55 (b)) do not show any particular structure on the membrane. Figures 63, 75, 87, and 99 are the images from the pristine Nafion 212 membranes. The current sensing and topographic images do not show any structural unity such as Nafion 115 membrane. The current sensing images of pristine Nafion 212 membrane also represent random structure. The maximum current is about 0.6 nA. The topographic images of the Nafion 212 membranes do not reveal any structural ordering.

The other images are annealed Nafion 115 and Nafion 212 membranes at different annealing temperatures. The specific information of each image is listed under the images. The annealing membranes show the development of the structural evolution from the current sensing images. After the membranes were annealed, the structure on the membrane clearly displays separation of the conductive and non-conductive regions such as filament structure. The filaments on the membrane are independent of the annealing times and temperatures. The width of a filament is approximately 100 nm. The filament shape might be explained by the re-organization of the cylindrical ionic cluster near the membrane surface by thermal annealing. This assumption is supported by many recent spectroscopy studies for the Nafion membrane near glass transition temperature. [75-85] Around glass transition temperature of the Nafion membrane, only the hydrophilic sulfonic acid groups have mobility because the side chain and back bone of the membrane have different relaxations due to the heterogeneous structure of the Nafion.

Kundu et al. studied mechanical properties of the thermally treated the Nafion 112 membranes using dynamic mechanical testing. [70] The dynamic mechanical testing measures stiffness loss of the membrane (storage modulus) and the increase of viscoelasticity (loss modulus). The results from their study represent that the storage modulus is continuously lost from 90^{o}C and the loss modulus shows variation between 90^{o}C and 150^{o}C. These result represent that the membrane is continuously loses stiffness while alpha transition is occurs between 90^{o}C and 150^{o}C. They insist that the reason of the change is the increasing mobility of the ionic clusters. The mobility increasing of the sulfonic acid groups induce the structural evolution on the

membrane.

The maximum current of each current sensing image varies with annealing temperatures. The maximum current variation of each current sensing image at each temperature follows the same trend. The maximum current on the membrane is initially increased by annealing and goes to the maximum approximately 10 hours annealing. After the current reaches a maximum, the current gradually decays and reaches to zero. There is no structural change in the topographic images by thermal annealing. It is clearly indicated by the topographic images of pristine and the annealed membrane.

Each image (c) refers to the line profile (cross-section of the selected region) of the conductance image and topography. The black solid line is from the conductance images and the red dot is from the topography. The line profiles offer a close view of the images. All the line profiles of current sensing and topographic images expose that these images do not have any similarity. The line profiles from the current sensing images display the evolution of filament structure on the membrane. After the filament structures have evolved, they do not show any changes because of annealing time as shown in the line profiles. Each line profile of the current sensing images from annealed membranes contains 10 to 20 filaments. The number and width of chains on the line profile are independent of annealing times and temperatures as shown in figure 17 to 106 (c). The line profile from the topographic images does not represent any morphological variation by thermal annealing.

The figure (d) from each image depicts the conductance distribution of the images. The conductance distribution from each CSAFM image is derived from each current sensing image. The conductance distribution mainly reflects the contact probability of the contact between the tip and the ionic clusters on the membrane surface, which connects to the proton

channel network in the membrane. When the tip is in contact with the membrane, the end of the tip is in contact with a small amount of the ionic clusters which connect to the ionic channel network over the membrane. Each ionic channel branches out or merges with others over a short distance in the ionic channel network in a Nafion membrane. The proton current flows out from the contact between the CSAFM tip and the membrane and then spreads over a large portion of the network before reaching the opposite electrode [62, 86]. Thus, the conductance distribution from each image shows the ionic clusters changing because of the thermal annealing of the membrane.

Almost all conductance distribution shows a Gaussian like distribution. Some of them show small peak near the zero conductance such as figure 20, 21, 22, and 23 (d). This zero peak could be affected by certain types of insulating materials on the membrane. These materials block contact between the tip and membrane. The CSAFM system only measured the conductance of the insulating materials. So, the system could not detect conductance at the position. Figures 21 (a) and (b) clearly proves this assumption. The black circle, which is in the bottom middle of the CSAFM image, corresponds with the white circle which is in the same position of the topography. The Gaussian like distribution of almost all images is explained by Poisson distribution. In probability theory and statistics, the Poisson distribution is a discrete probability distribution that expresses the probability of a given number of events occurring in a fixed interval of time and/or space when these events occur with a known average rate and independently of the time since the last event [87]. For specific intervals at such a distance, area or volume, Poisson's distribution also can be used. If the expected number of occurrences in this interval is μ, then the probability that there are exactly n occurrences is equal to

$$P_n = \frac{\mu^n}{n!} e^{-\mu} \qquad (1)$$

In this equation, the symbol μ has important meaning. The symbol μ is the average number of counts per unit time. For large number of μ, the Poisson distribution is approximated to be the normal distribution. [87]

$$\frac{\mu^x e^{-\mu}}{x!} \cong \frac{1}{\sqrt{2\pi\mu}} e^{-\frac{(x-\mu)^2}{2\mu}}, \text{ large } \mu \qquad (2)$$

In this study, we assume that each radius of the tip is always constant during scanning. Because of the constant tip radius, the current at each pixel on the current sensing image is related to the number of the ionic clusters in contact with the tip. Because it reflects contact probability between the ionic clusters and the tip, the conductance distribution mainly reflects the contact probability of the tip and ionic clusters on the membrane surface, which connects to the proton channel network in the membrane. The current sensing image is a collection of the expectation value of the fixed area (tip radius). So, conductance distribution should follow a Poisson distribution P(n,μ), where μ is the average number of clusters in contact with the tip. The contact radius of the tip is roughly 8 nm and the radius of the ionic cluster is approximated 2.4 nm. So, four or more clusters always keep in contact with the tip when the tip radius is constant. In this case, Poisson distribution can be approximated to be a Gaussian distribution. Thus, many images of conductance distribution of this study show a Gaussian-like distribution. However, this assumption cannot explain all conductance distributions, because it is over simplified. In actuality, the contact radius changes during scanning because of deformation of the tip. The cluster radius and distribution of clusters were approximated by the water channel model. These unexpected effects induce the non-

Gaussian-like distributions.

At all annealing temperatures, the variation of current distribution by annealing time shows the same patterns. During the annealing, the distribution shape is sustained and the peak value (mean value) is initially shifted to a high conductance for 10 hours and then gradually shifted to low conductance. The full width at half maximum of the conductance distribution becomes wider since annealing starts and it becomes widest after approximately 10 hours. After 10 hours the full width at half maximum becomes narrow.

Figure captions

From figure 17 to figure 106

(a). Current sensing images of Nafion® 115 and Nafion® 212. The imaging conditions were identical to all images (room temperature under a 50% relative humidity).

(b). Topographic images of Nafion® 115 and Nafion® 212. The imaging conditions were identical to all images (room temperature under a 50% relative humidity).

(c). Line profiles of current sensing and topographic images of Nafion® 115 and Nafion® 212. Red dot and black solid line represent, respectively, the cross section of selected line of current sensing and topographic images

(d). Conductance distribution of each current sensing image of Nafion® 115 and Nafion® 212.

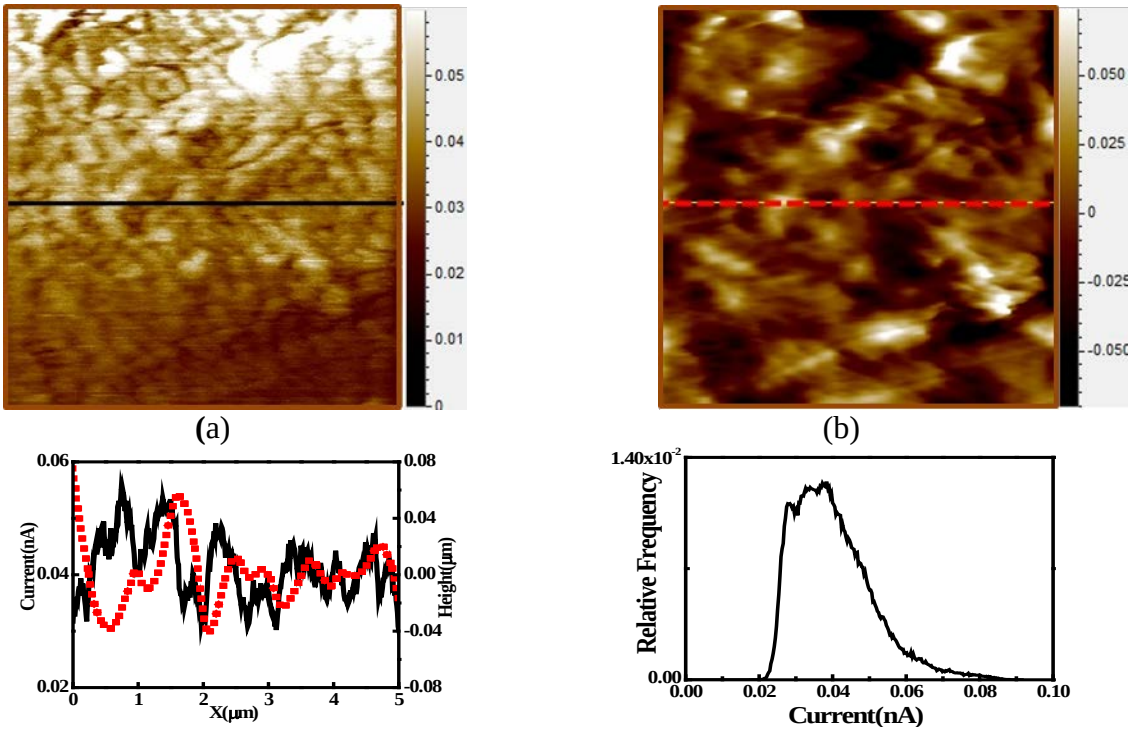

Figure 17. Nafion® 115, Pristine

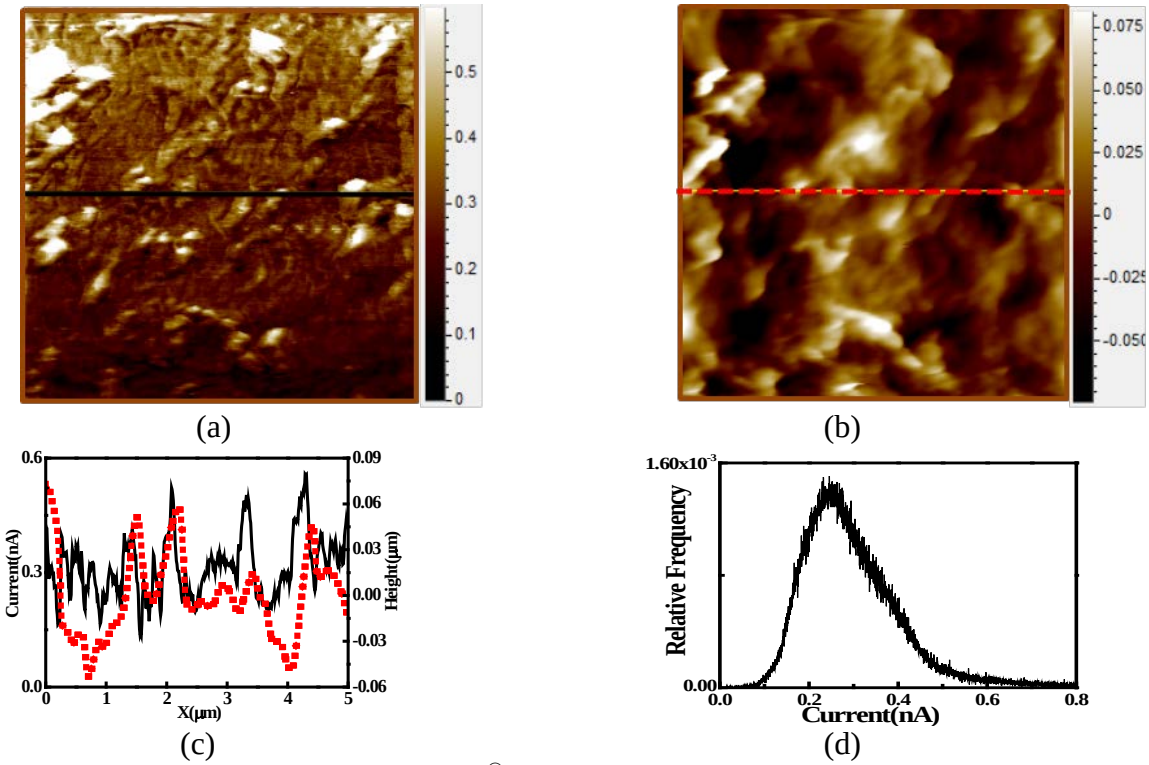

Figure 18. Nafion® 115 annealed at 90°C for 10 hours

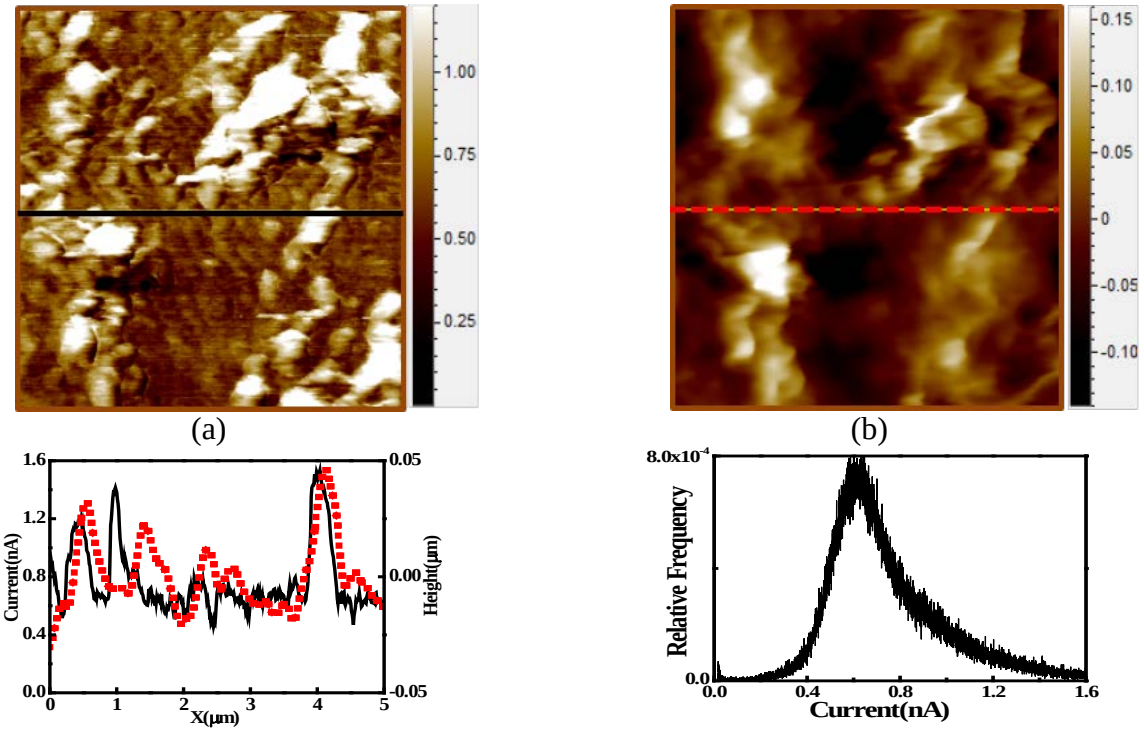

Figure 19. Nafion® 115 annealed at 90°C for 25 hours

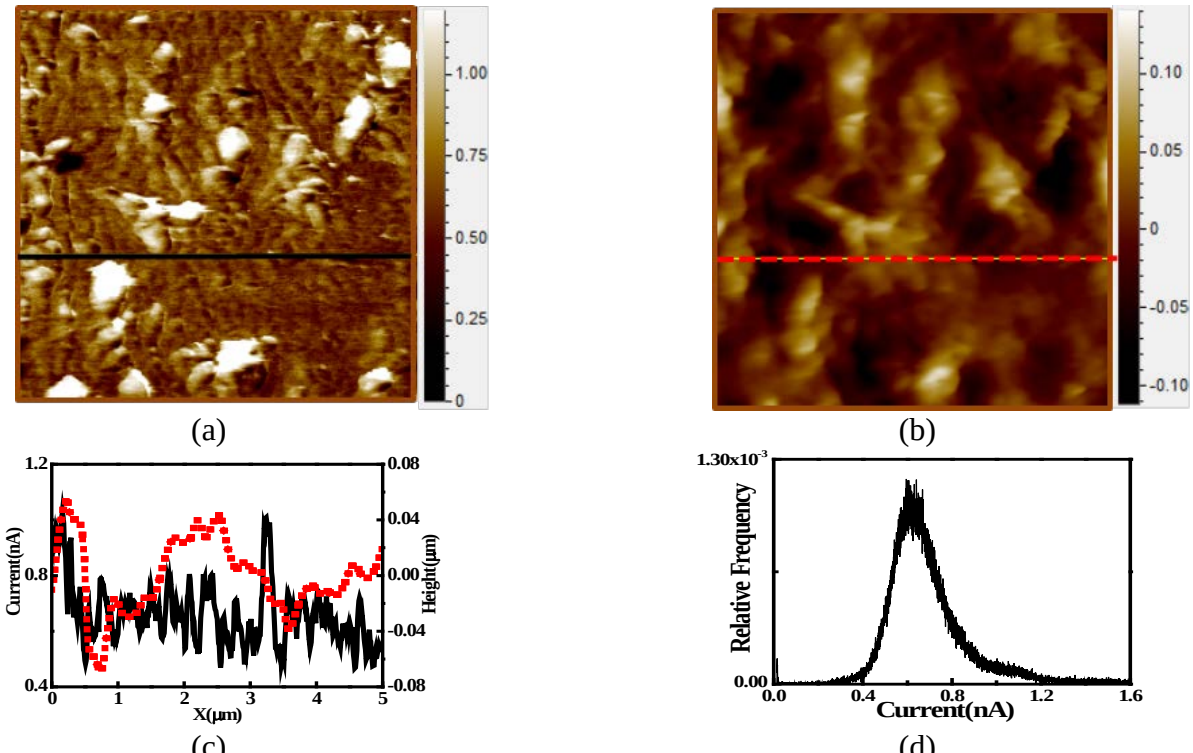

Figure 20. Nafion® 115 annealed at 90°C for 31 hours

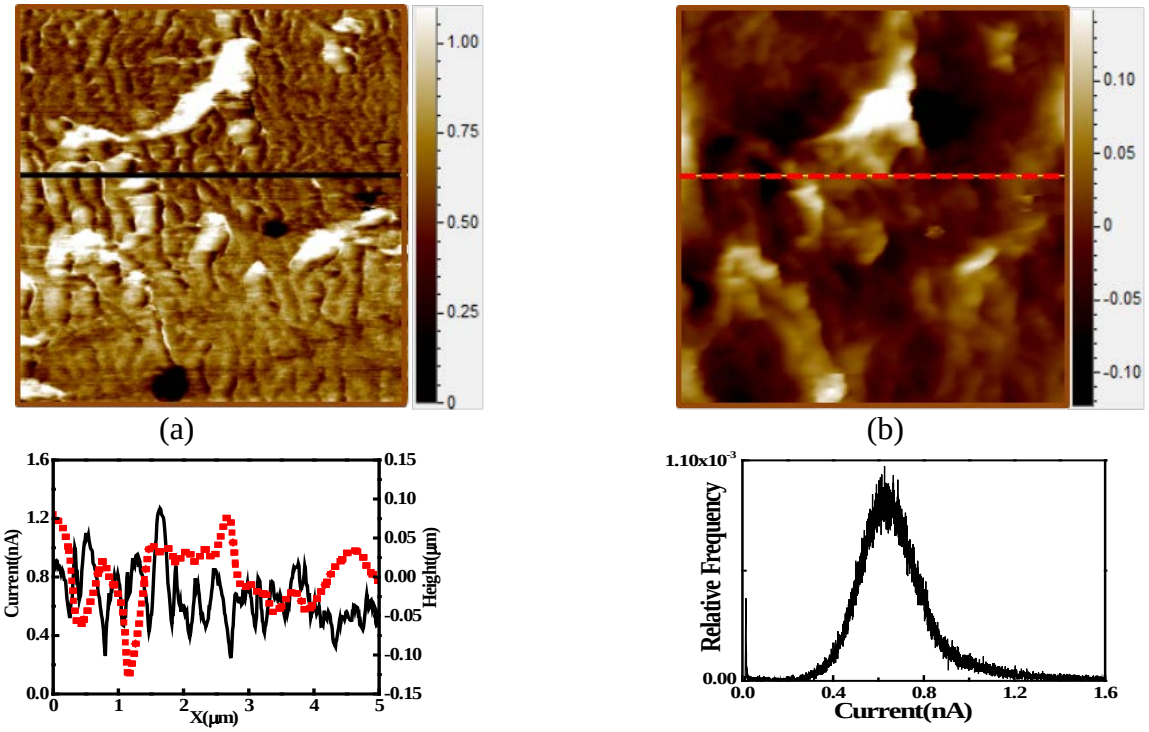

Figure 21. Nafion® 115 annealed at 90°C for 37 hours

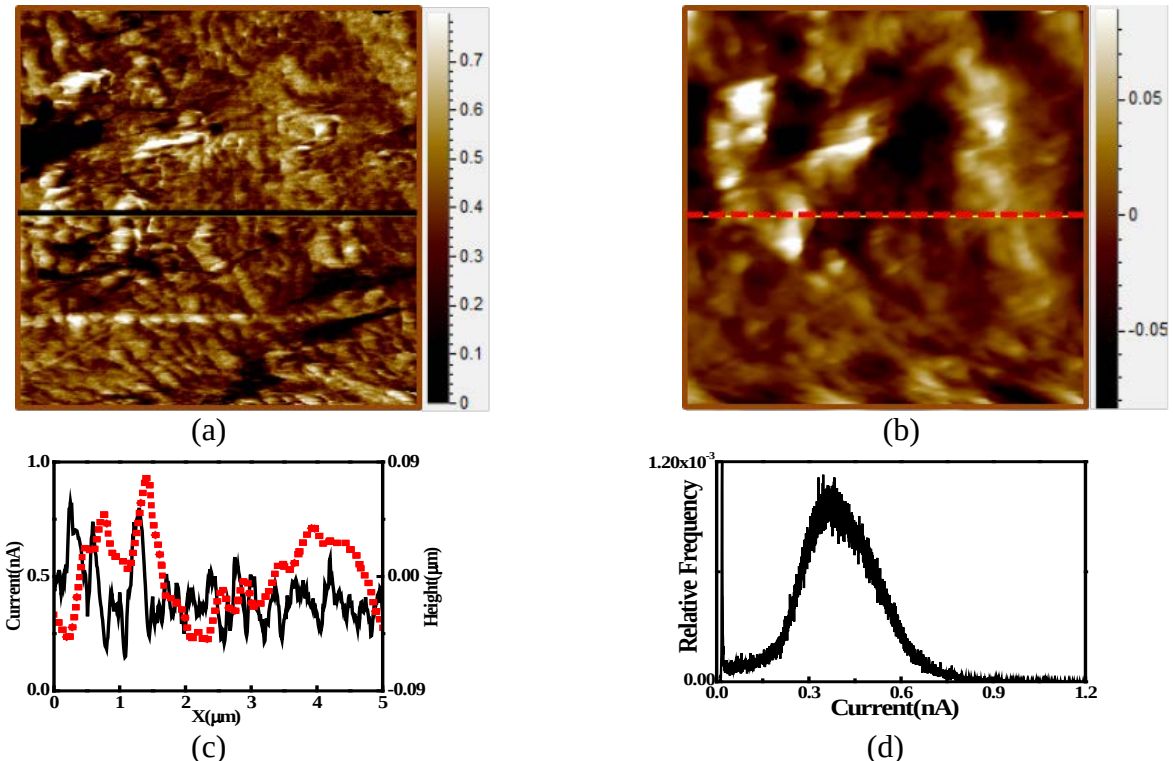

Figure 22. Nafion® 115 annealed at 90°C for 49 hours

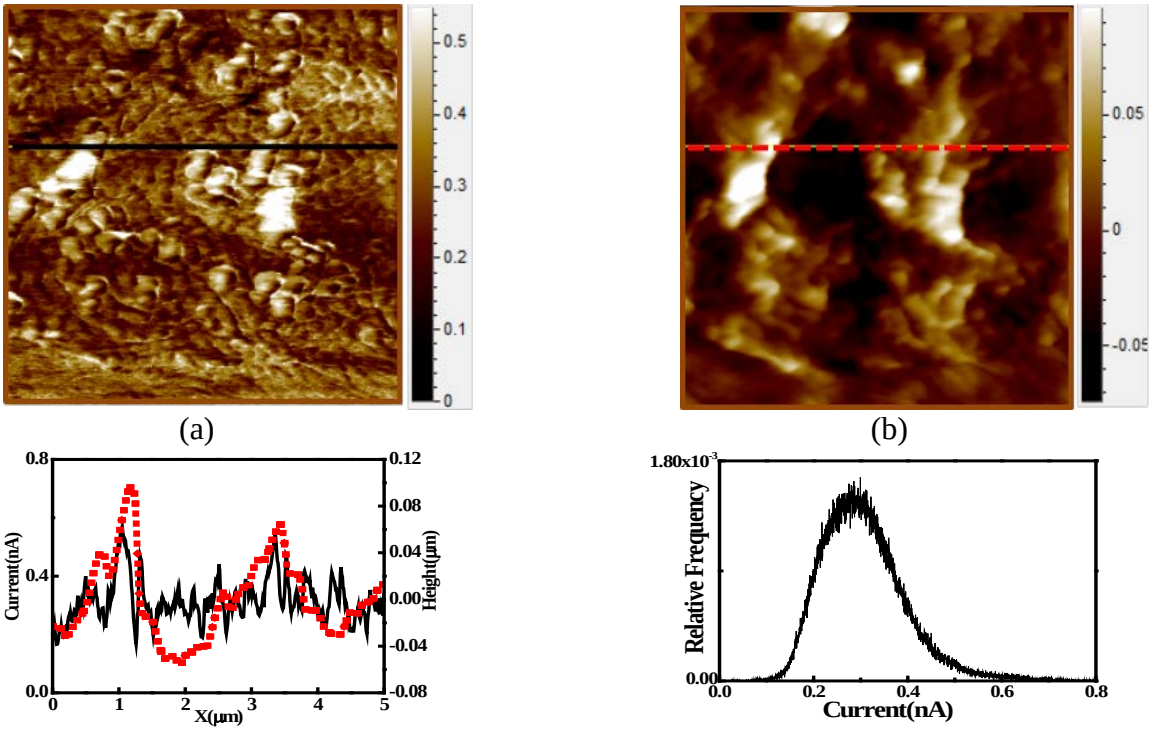

Figure 23. Nafion® 115 annealed at 90°C for 60 hours

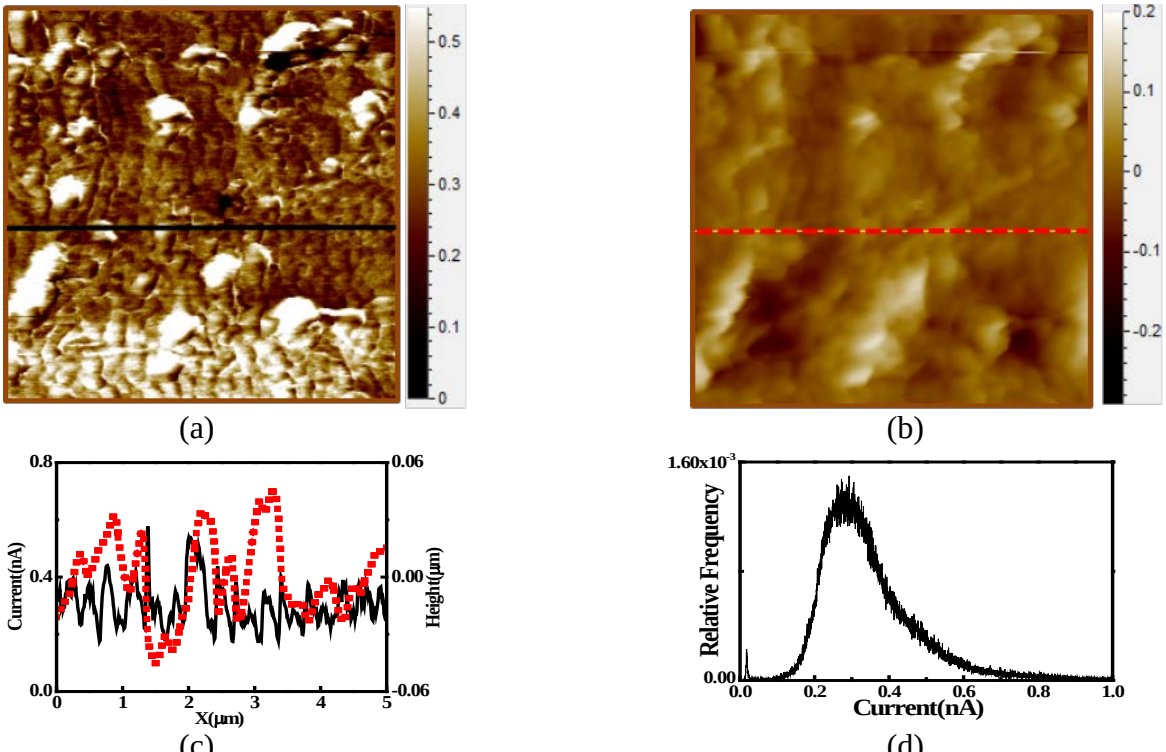

Figure 24. Nafion® 115 annealed at 90°C for 66 hours

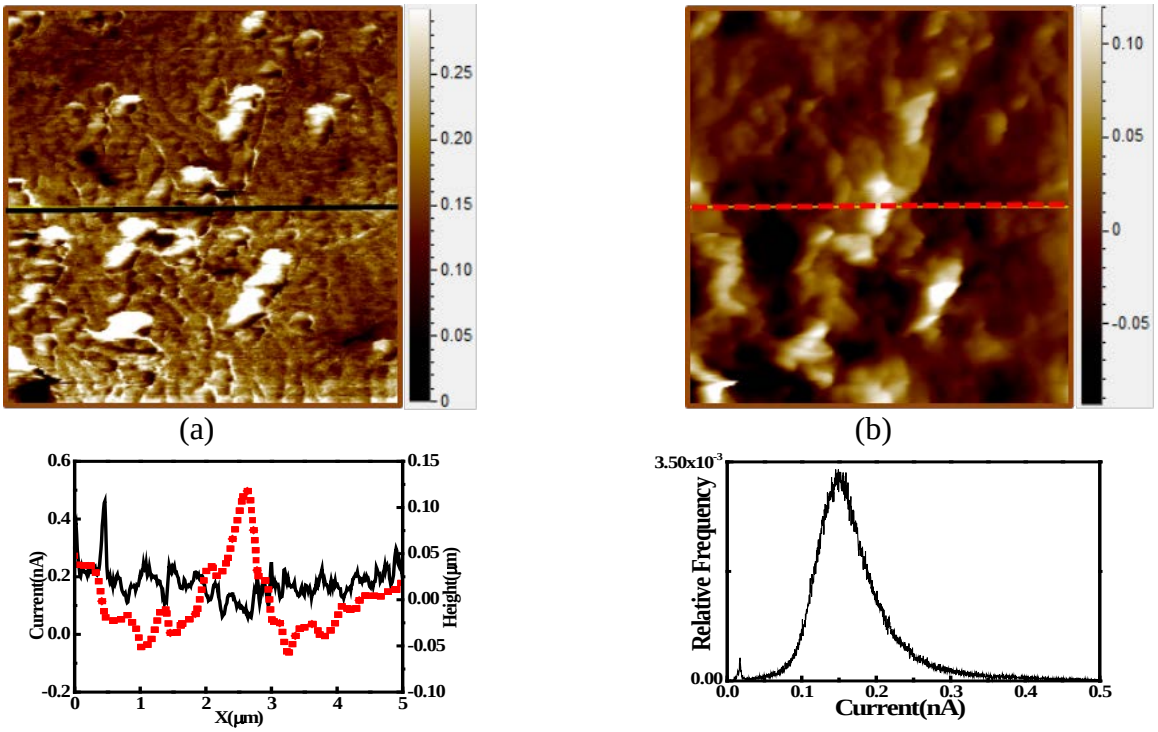

Figure 25. Nafion® 115 annealed at 90°C for 77 hours

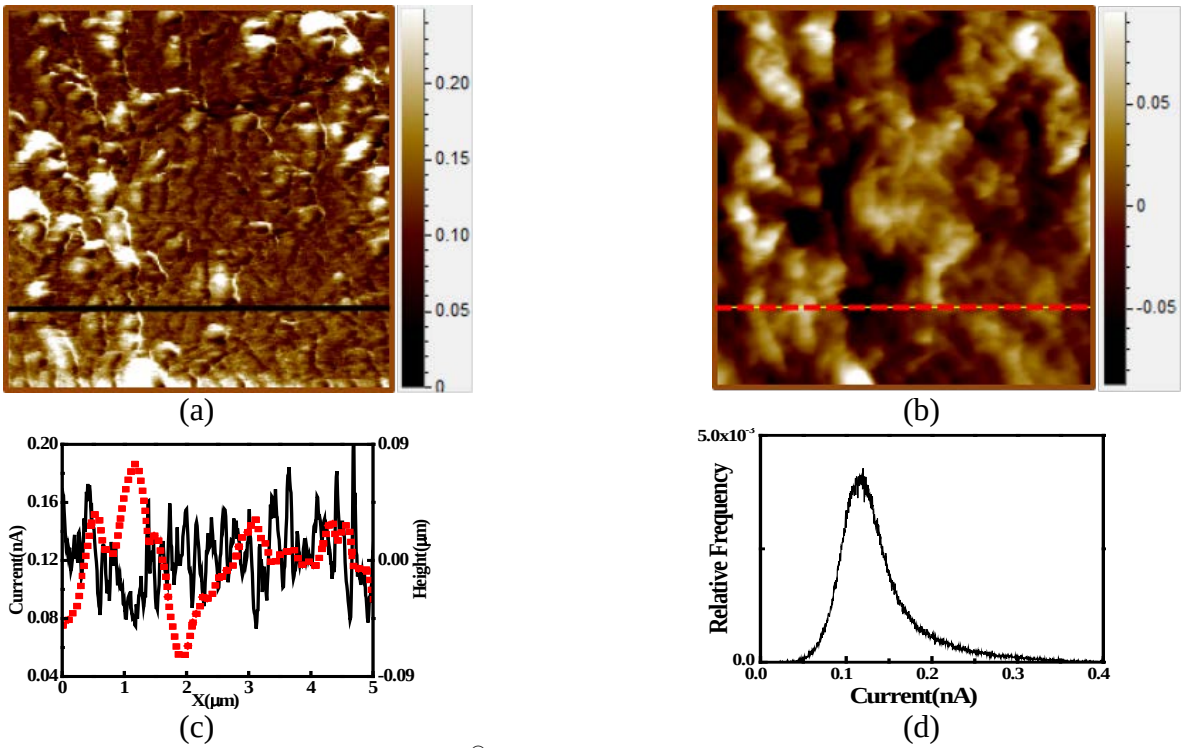

Figure 26. Nafion® 115 annealed at 90°C for 94 hours

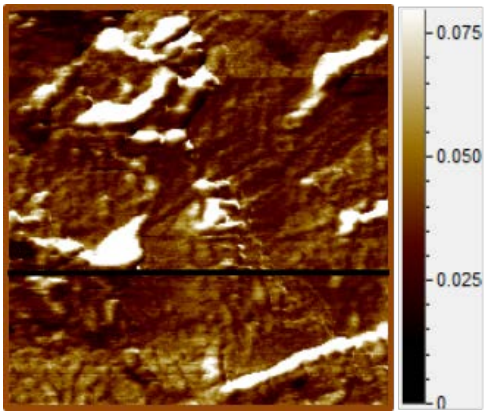

(a)

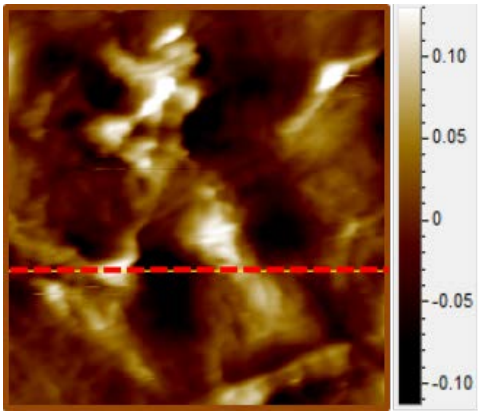

(b)

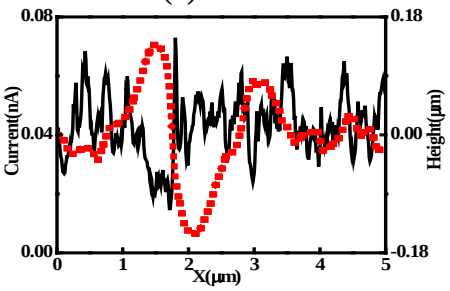

(c)

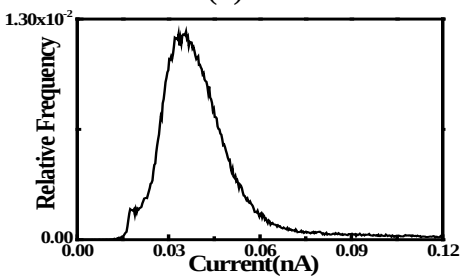

(d)

Figure 27. Nafion® 115 annealed at 90°C for 111 hours

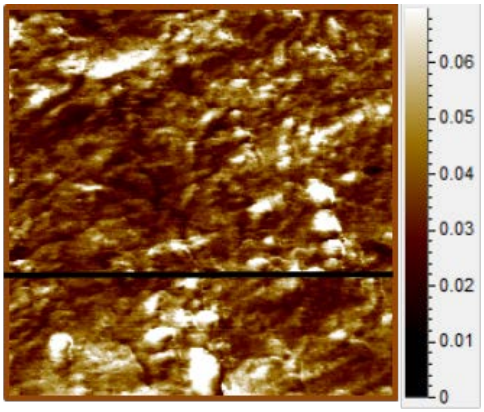

(a)

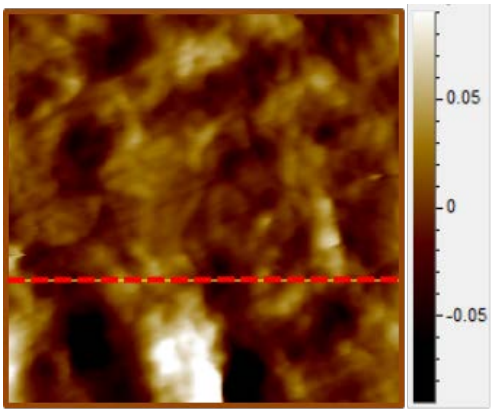

(b)

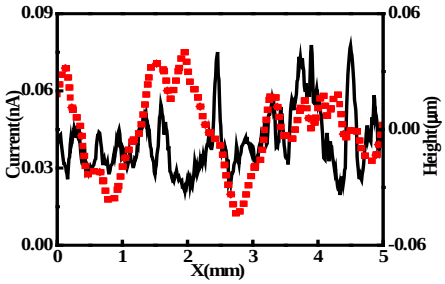

(c)

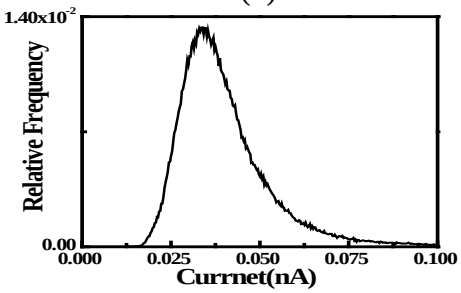

(d)

Figure 28. Nafion® 115 annealed at 90°C for 117 hours

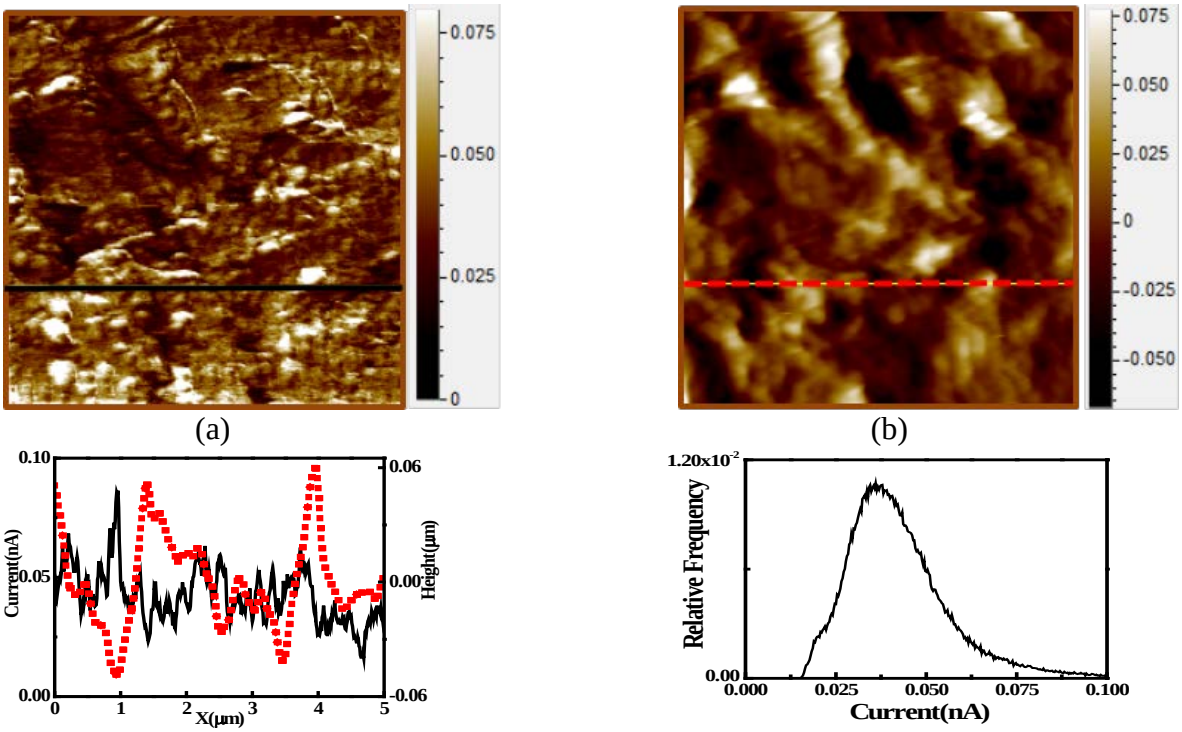

Figure 29. Nafion® 115 annealed at 90°C for 123 hours

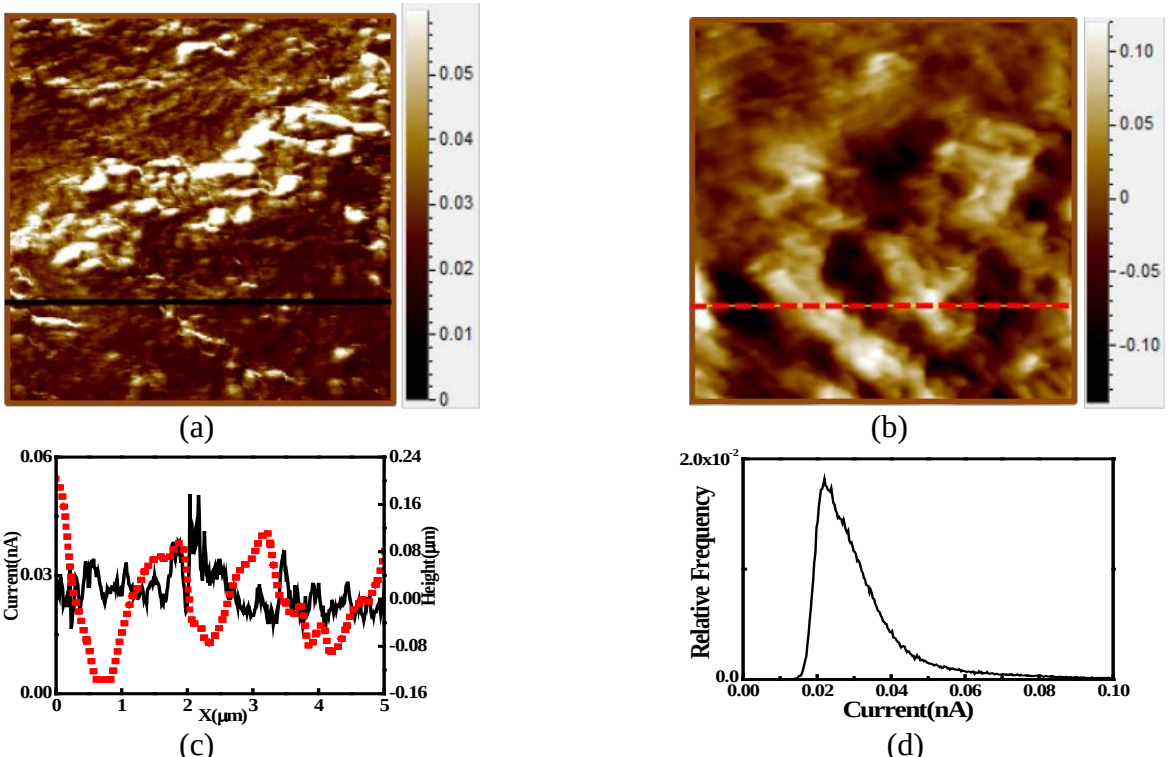

Figure 30. Nafion® 115 annealed at 90°C for 129 hours

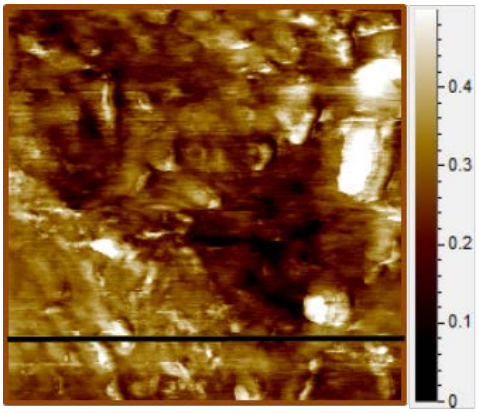

(a)

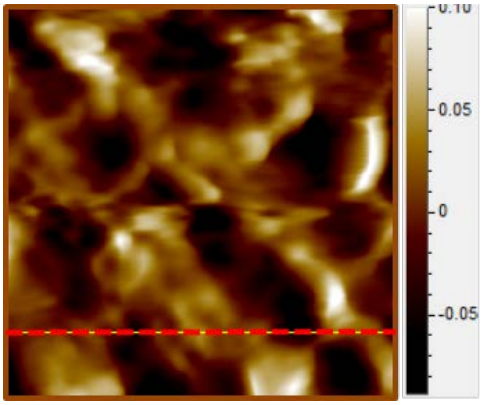

(b)

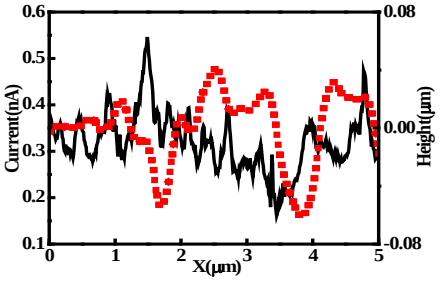

(c)

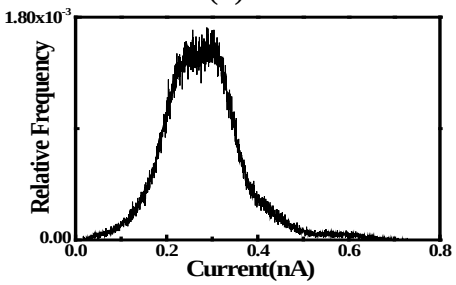

(d)

Figure 31. Nafion® 115, Pristine

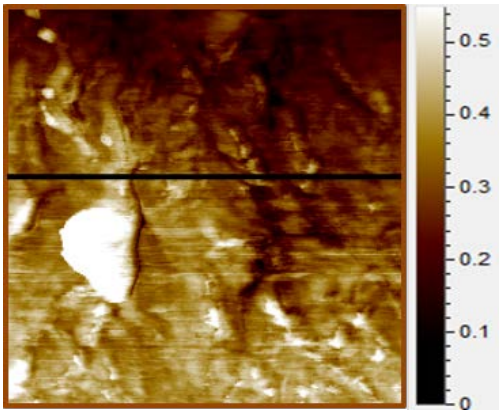

(a)

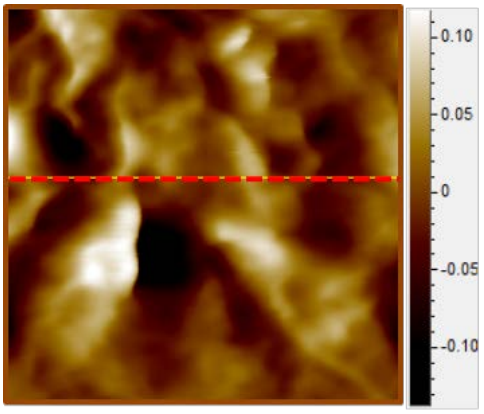

(b)

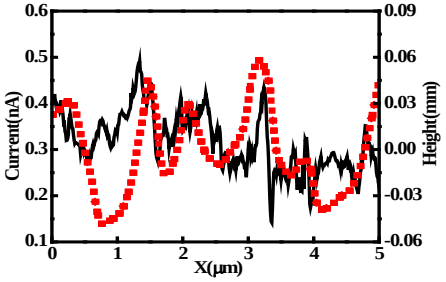

(c)

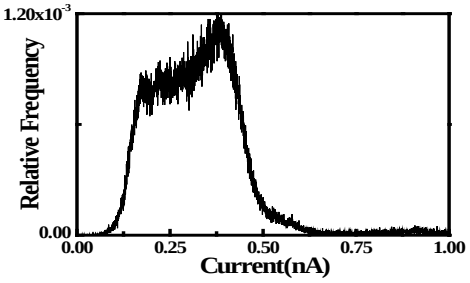

(d)

Figure 32. Nafion® 115 annealed at 100°C for 6 hours

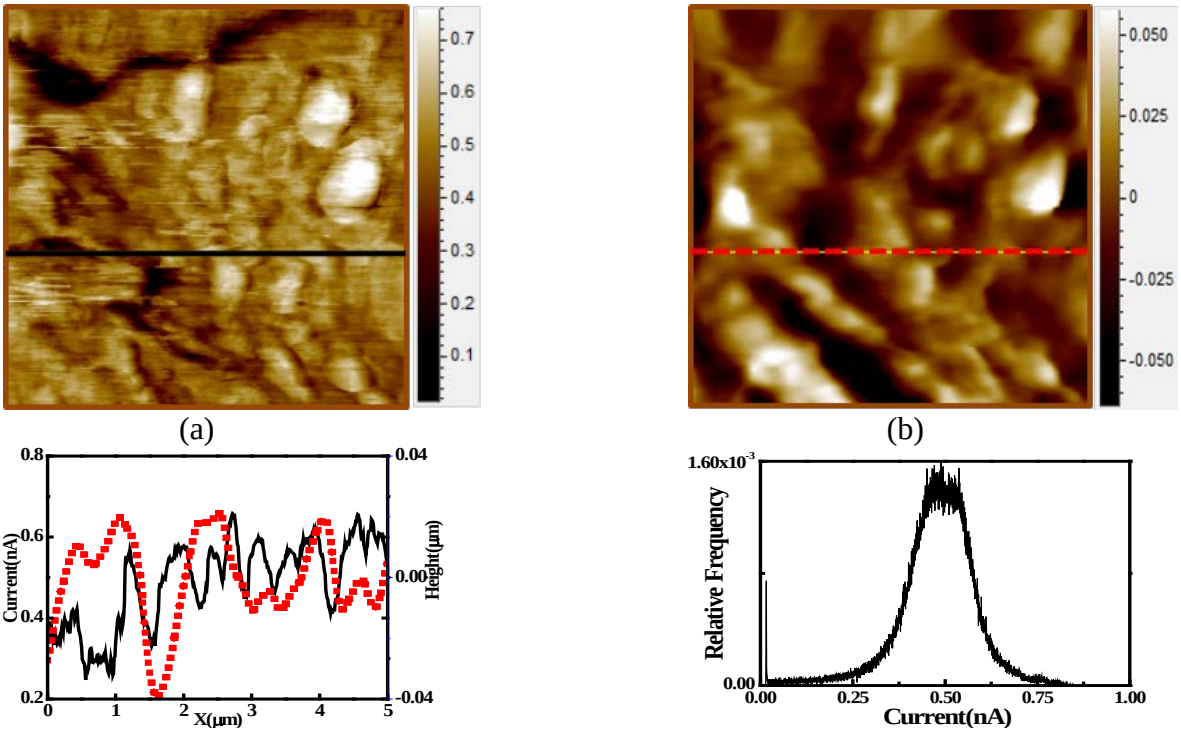

Figure 33. Nafion® 115 annealed at 100°C for 11 hours

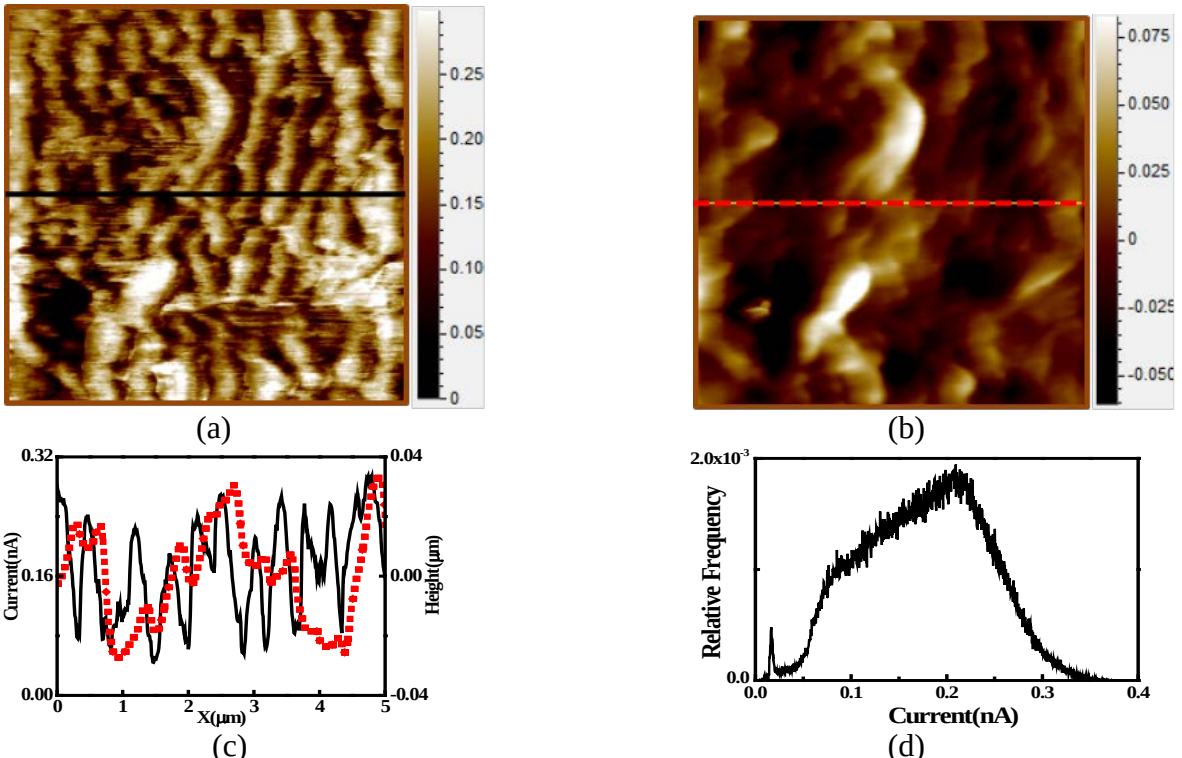

Figure 34. Nafion® 115 annealed at 100°C for 21 hours

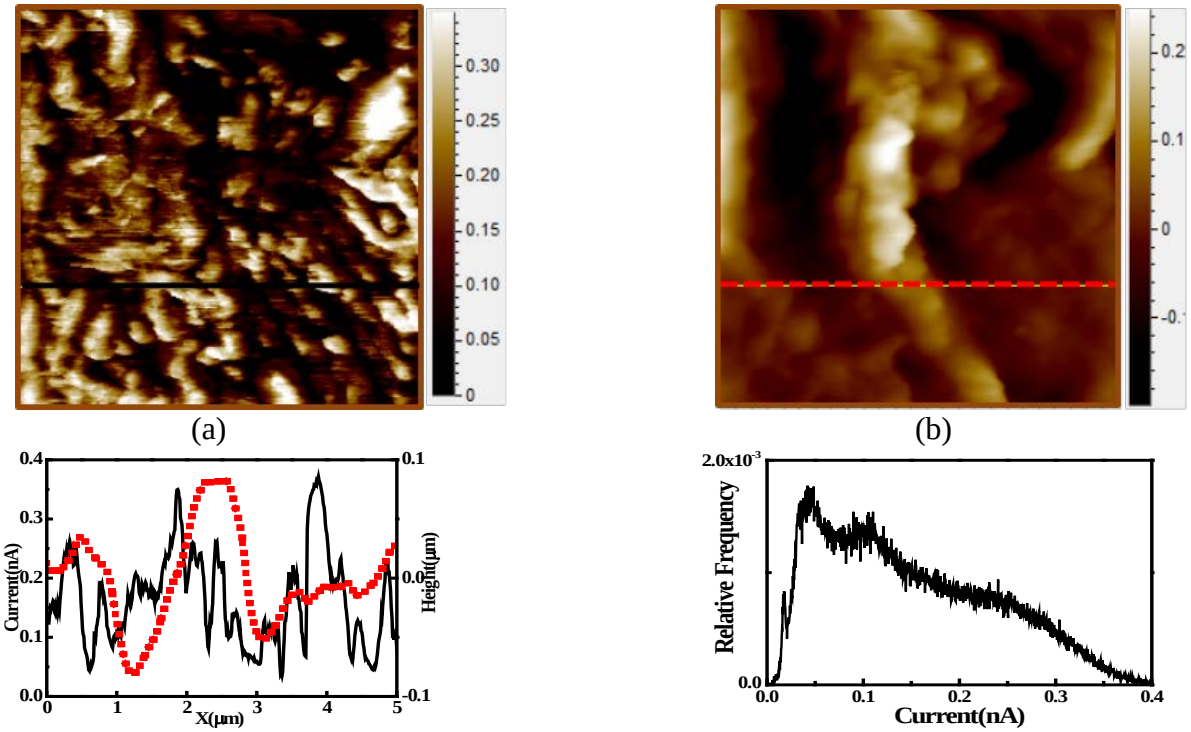

Figure 35. Nafion® 115 annealed at 100°C for 31 hours

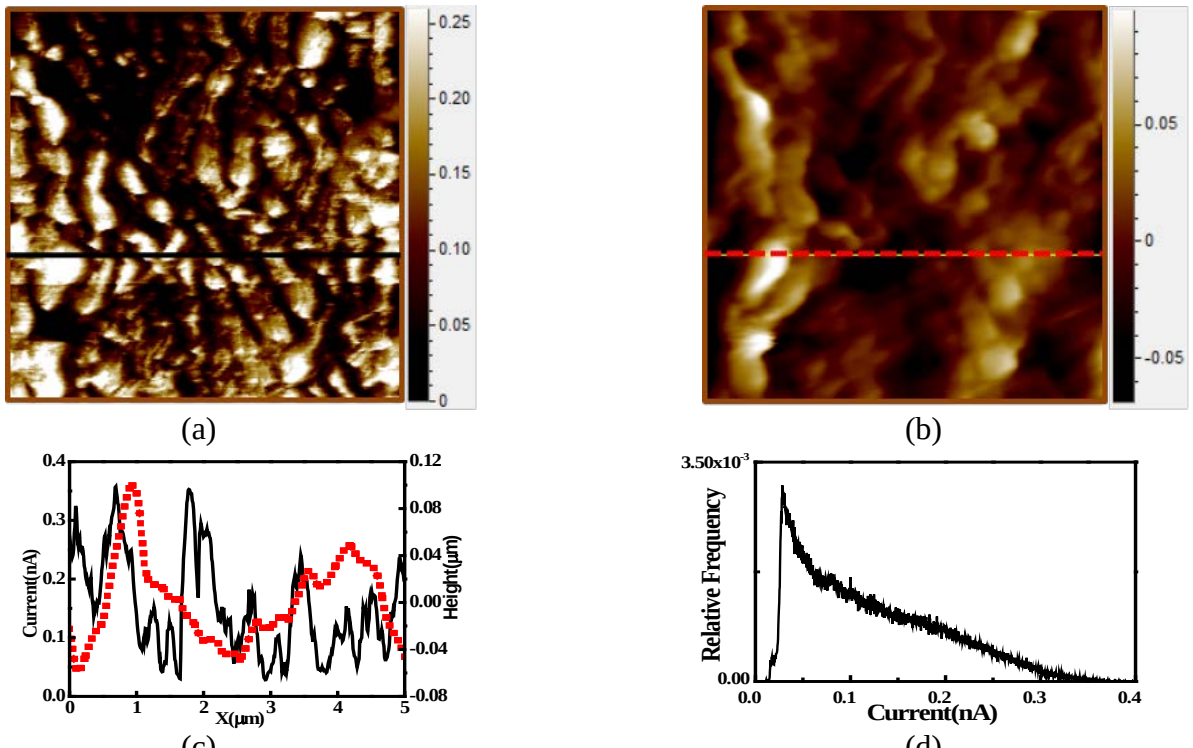

Figure 36. Nafion® 115 annealed at 100°C for 36 hours

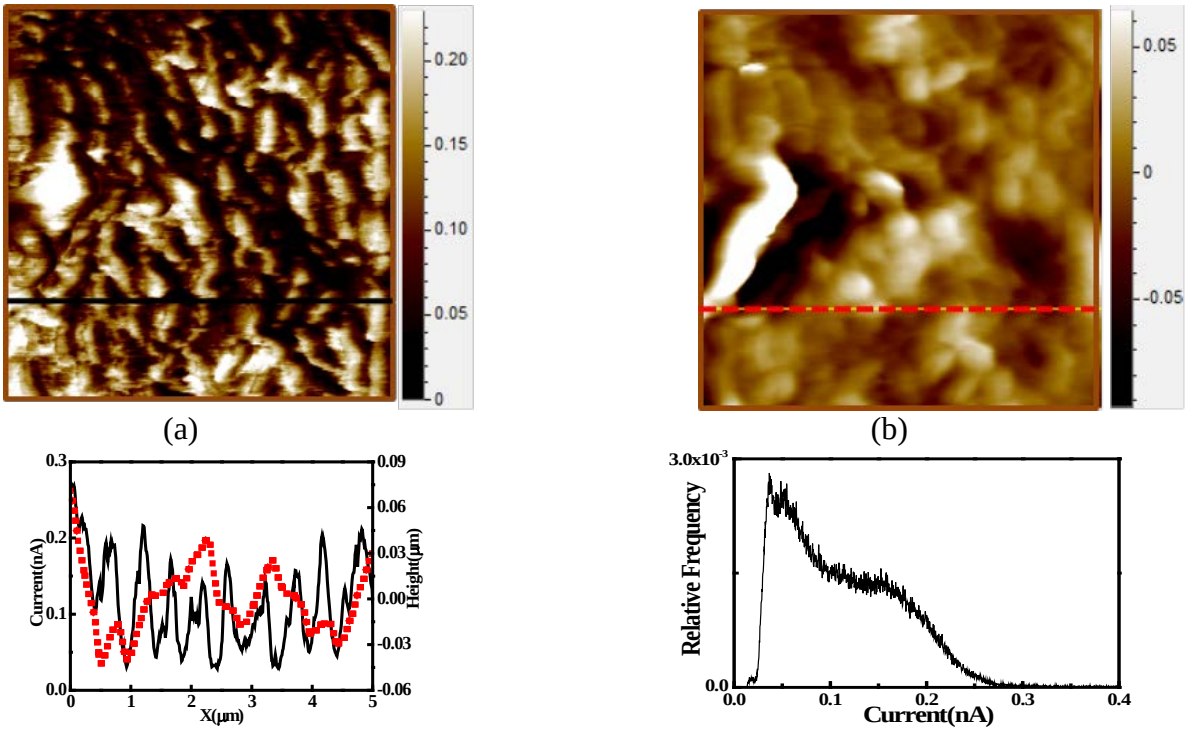

Figure 37. Nafion® 115 annealed at 100°C for 46 hours

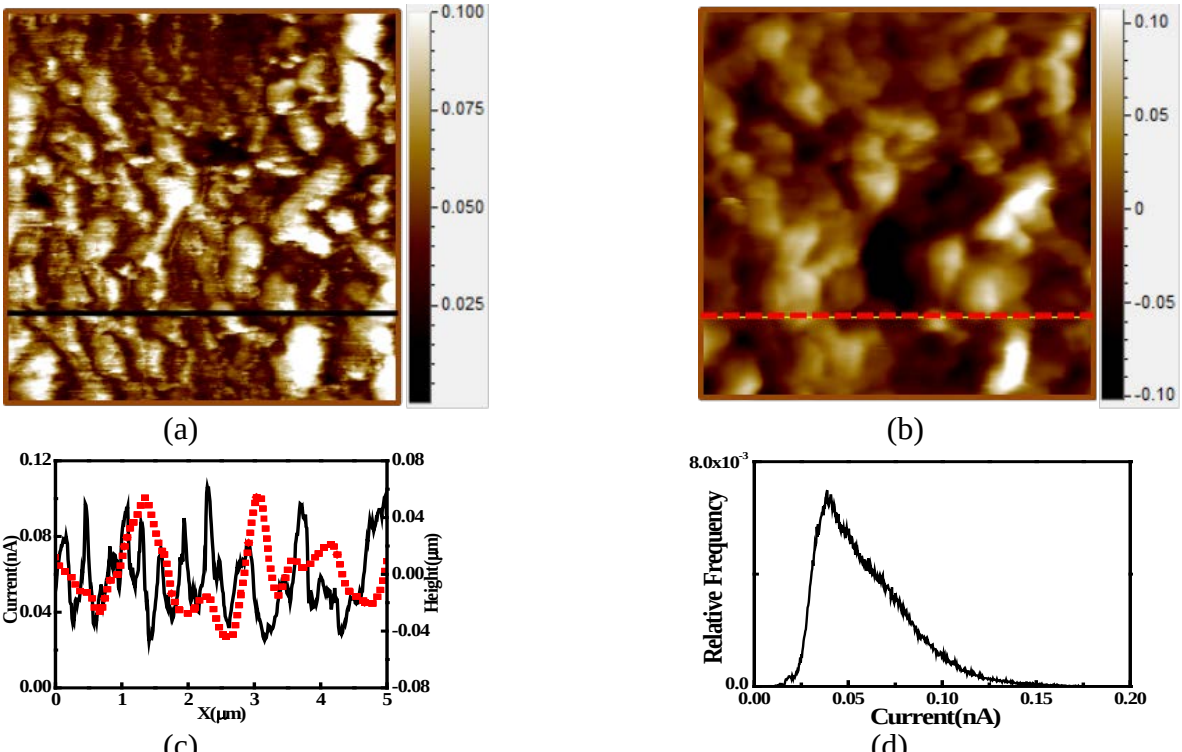

Figure 38. Nafion® 115 annealed at 100°C for 56 hours

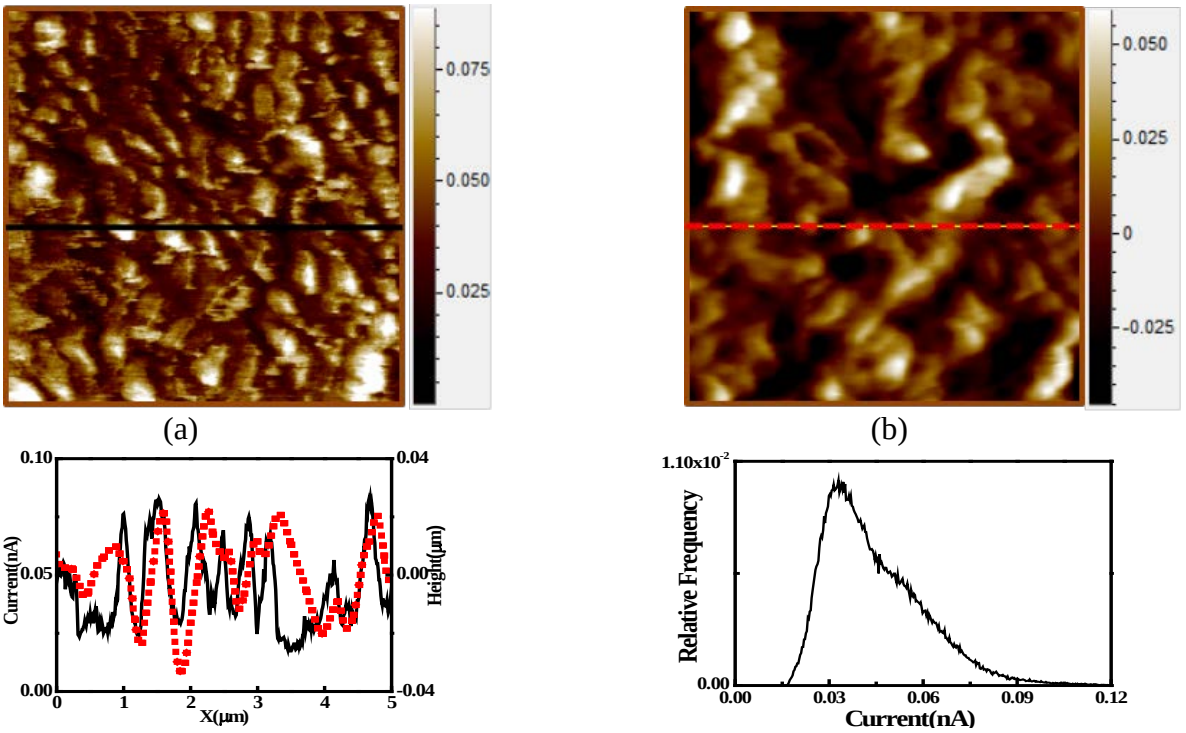

Figure 39. Nafion® 115 annealed at 100°C for 65 hours

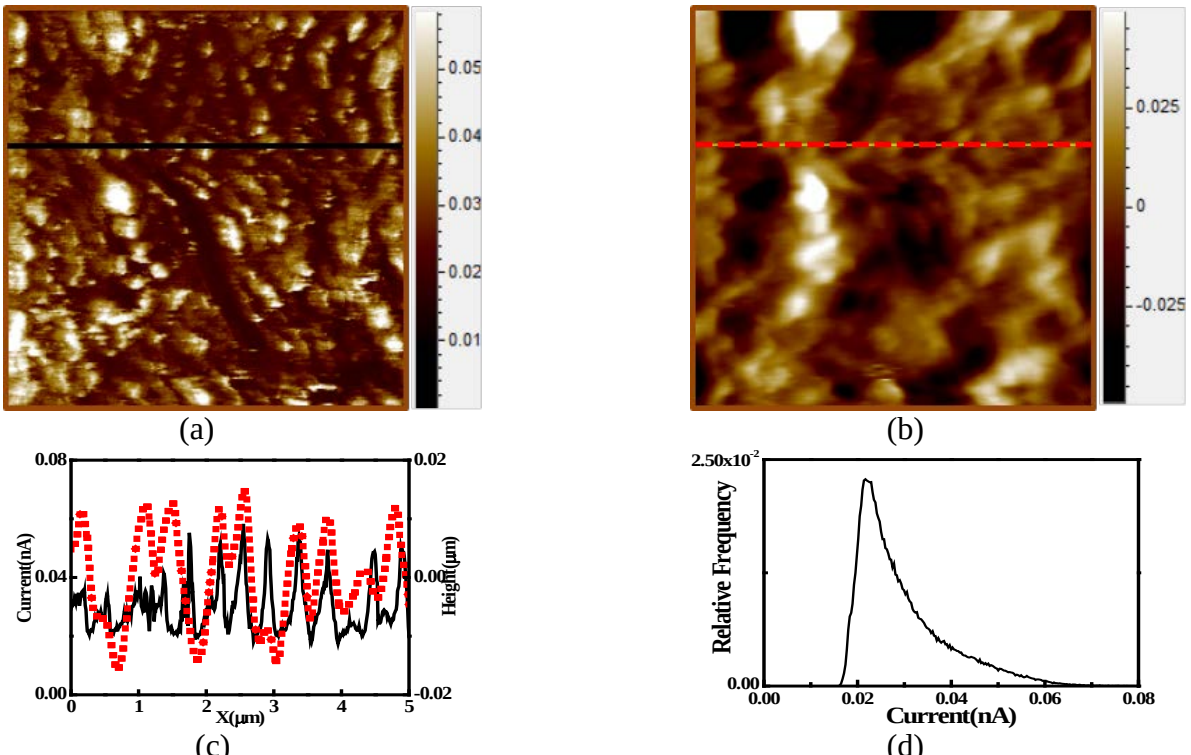

Figure 40. Nafion® 115 annealed at 100°C for 70 hours

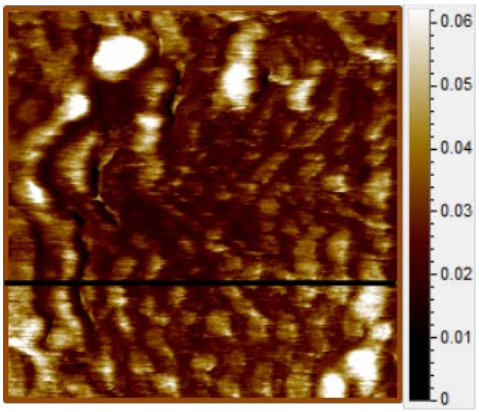

(a)

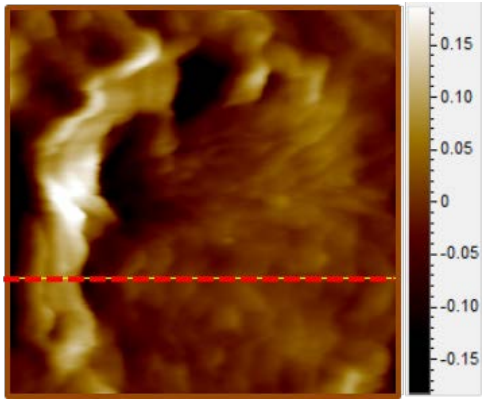

(b)

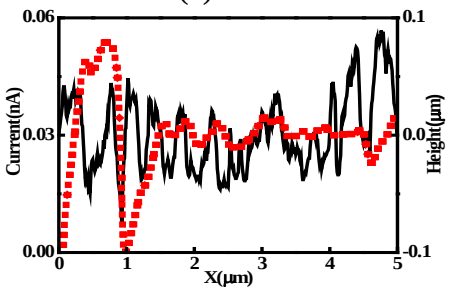

(c)

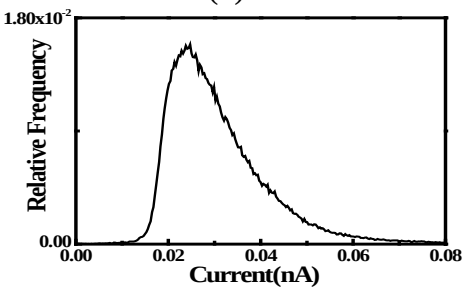

(d)

Figure 41. Nafion® 115 annealed at 100°C for 79 hours

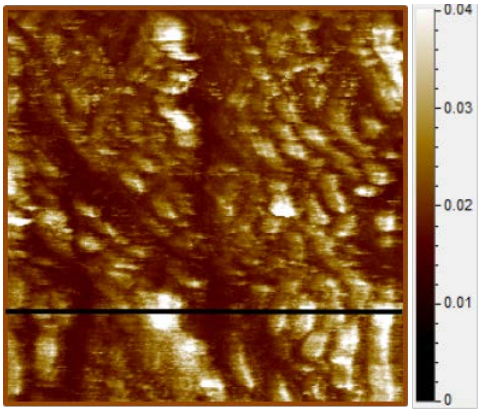

(a)

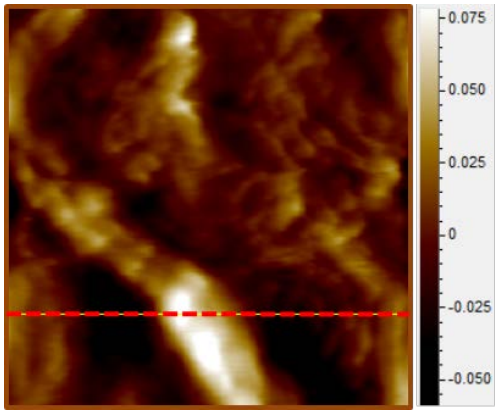

(b)

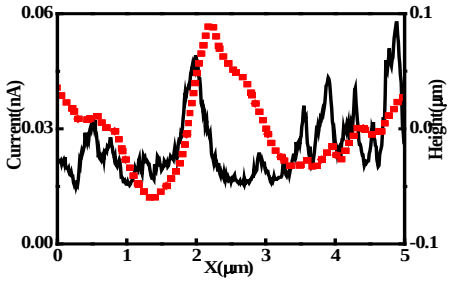

(c)

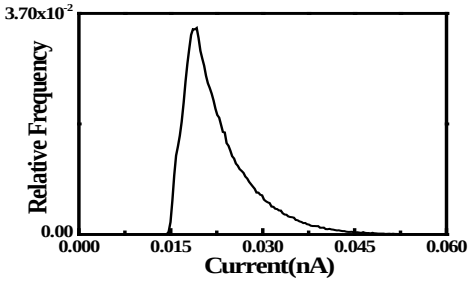

(d)

Figure 42. Nafion® 115 annealed at 100°C for 84 hours

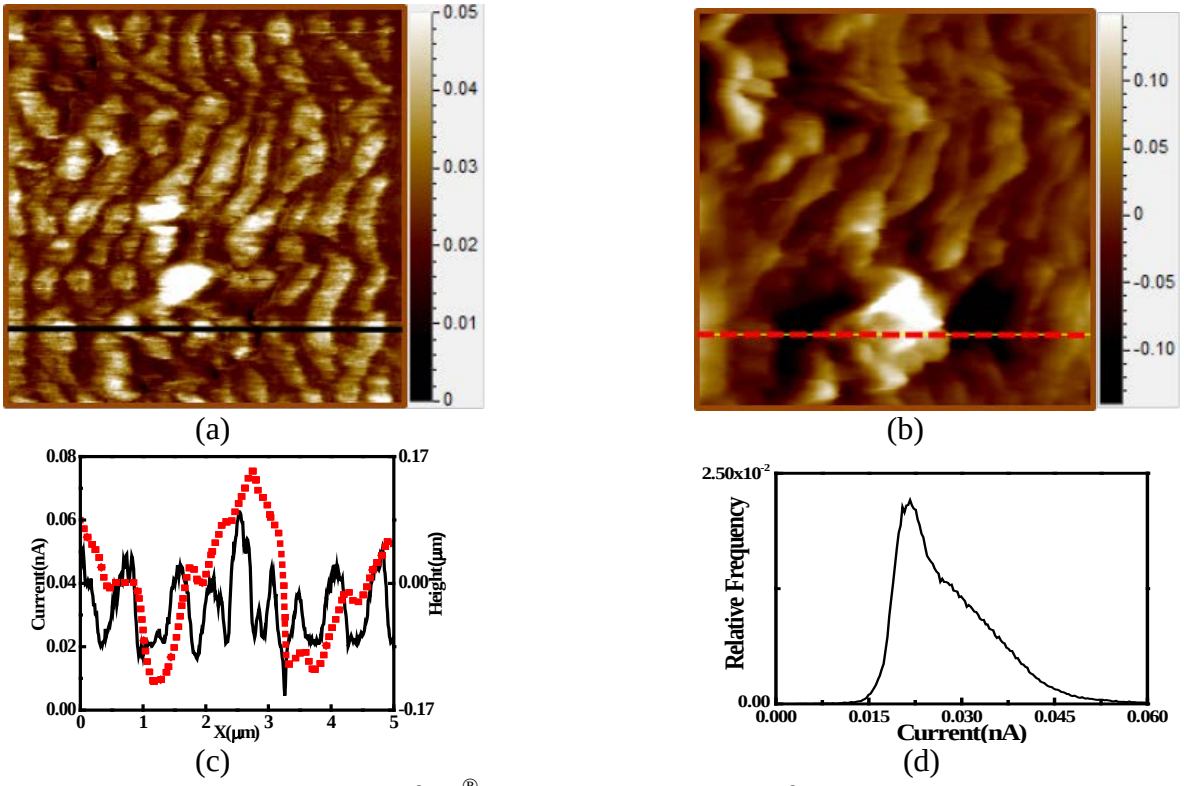

Figure 43. Nafion® 115 annealed at 100°C for 94 hours

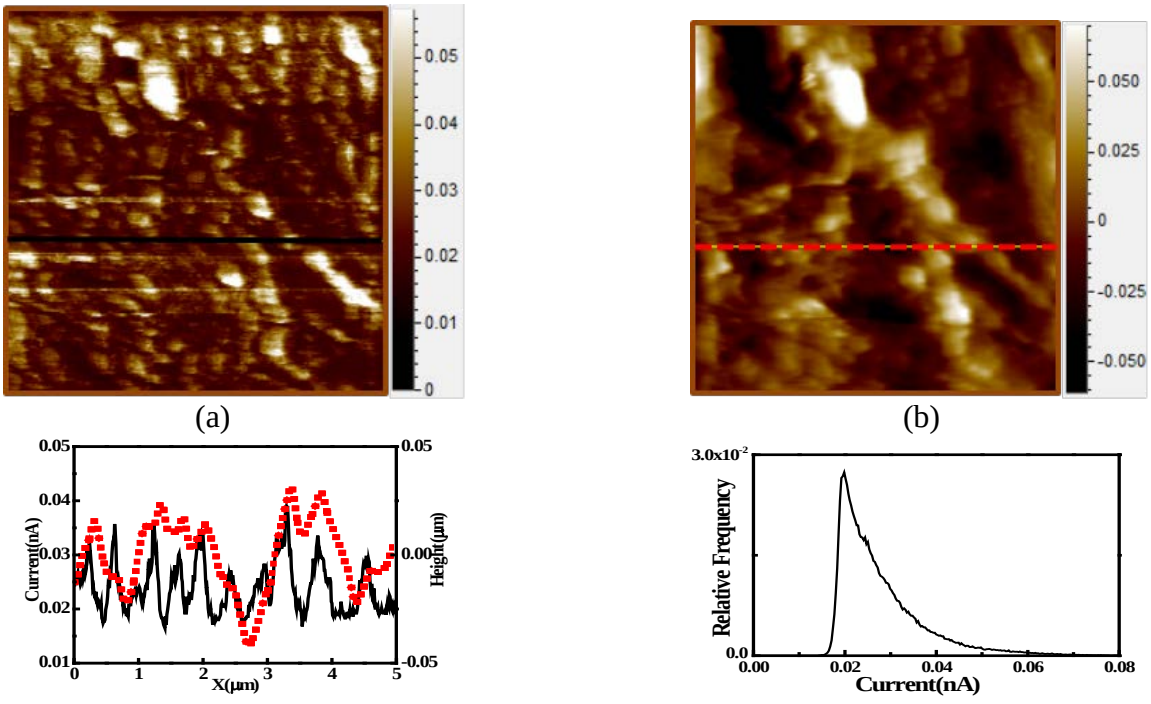

Figure 44. Nafion® 115 annealed at 100°C for 89 hours

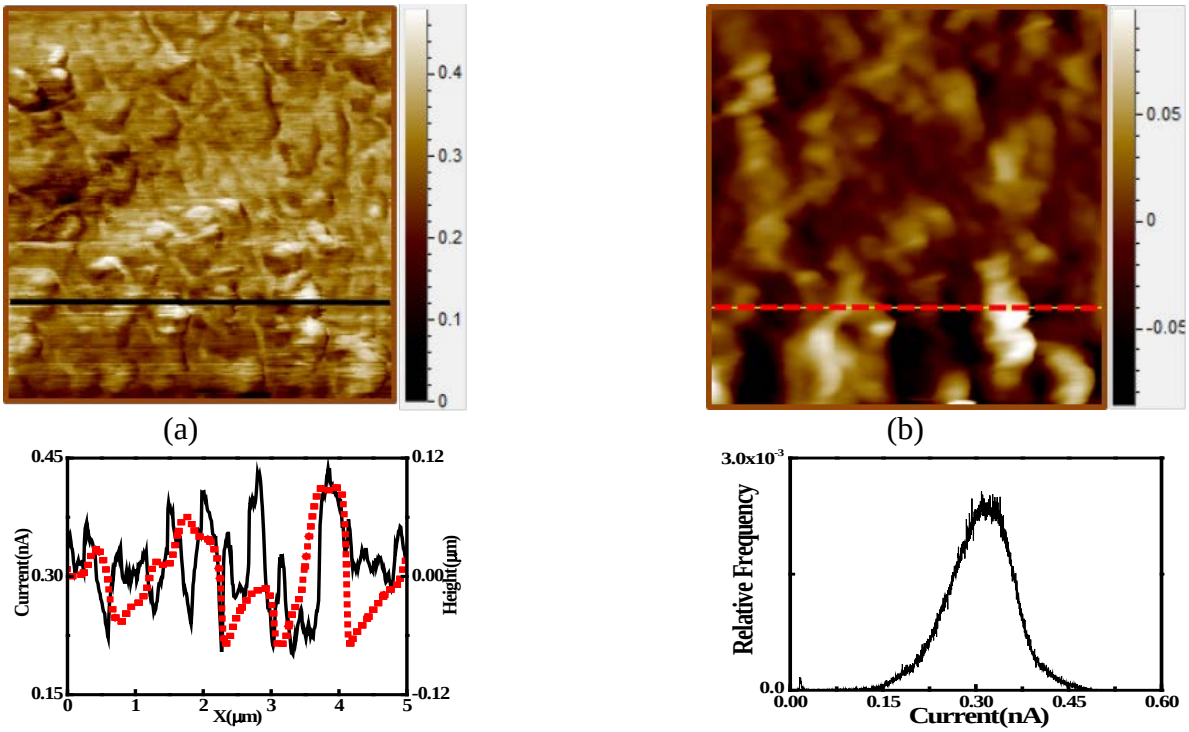

Figure 45. Nafion® 115, Pristine

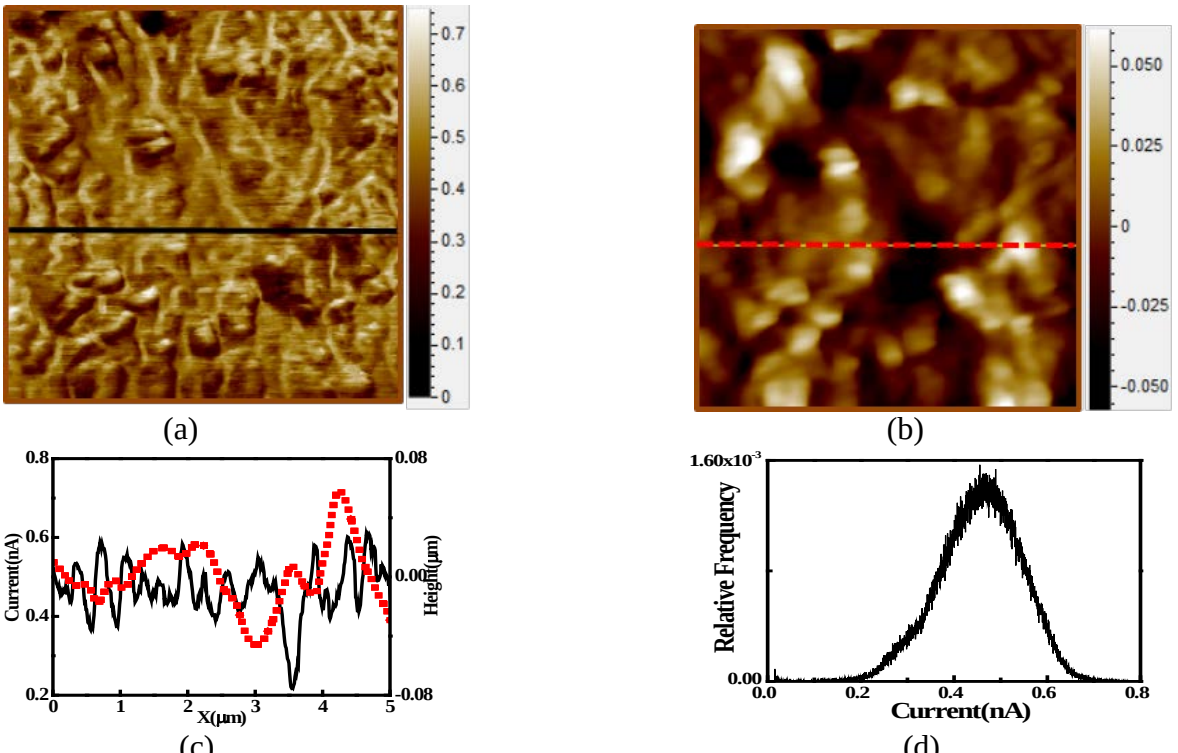

Figure 46. Nafion® 115 annealed at 110°C for 6 hours

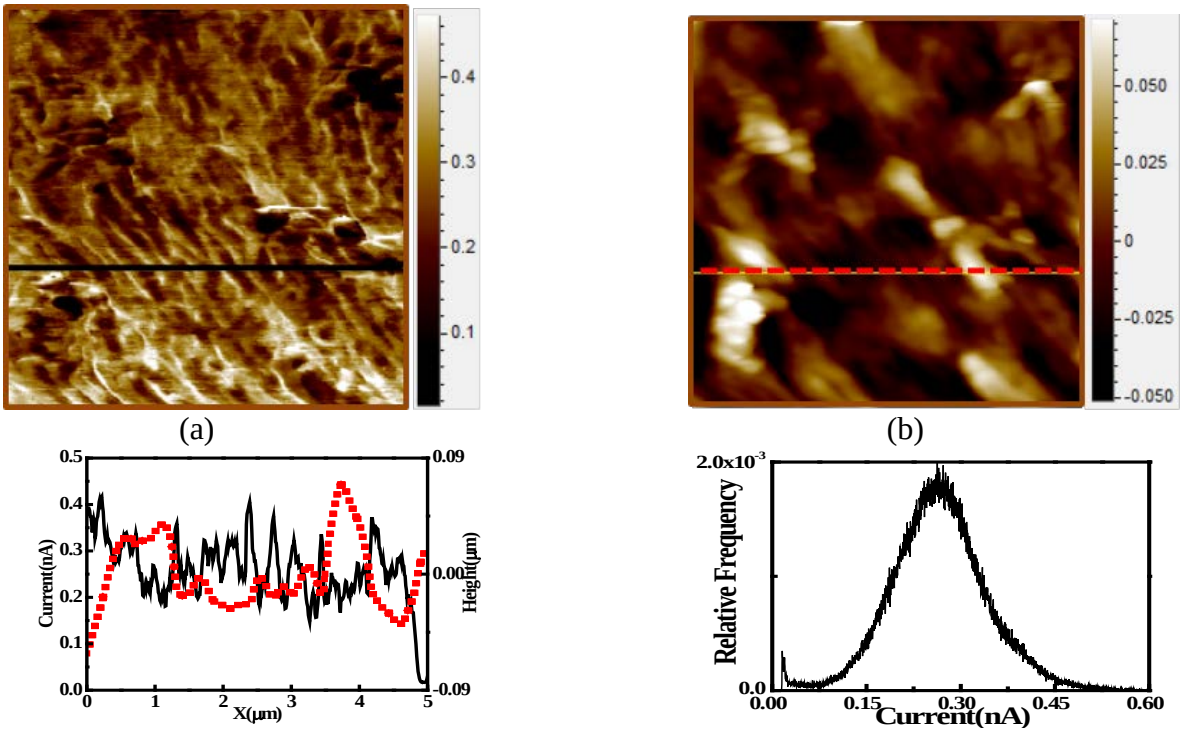

Figure 47. Nafion® 115 annealed at 110°C for 14 hours

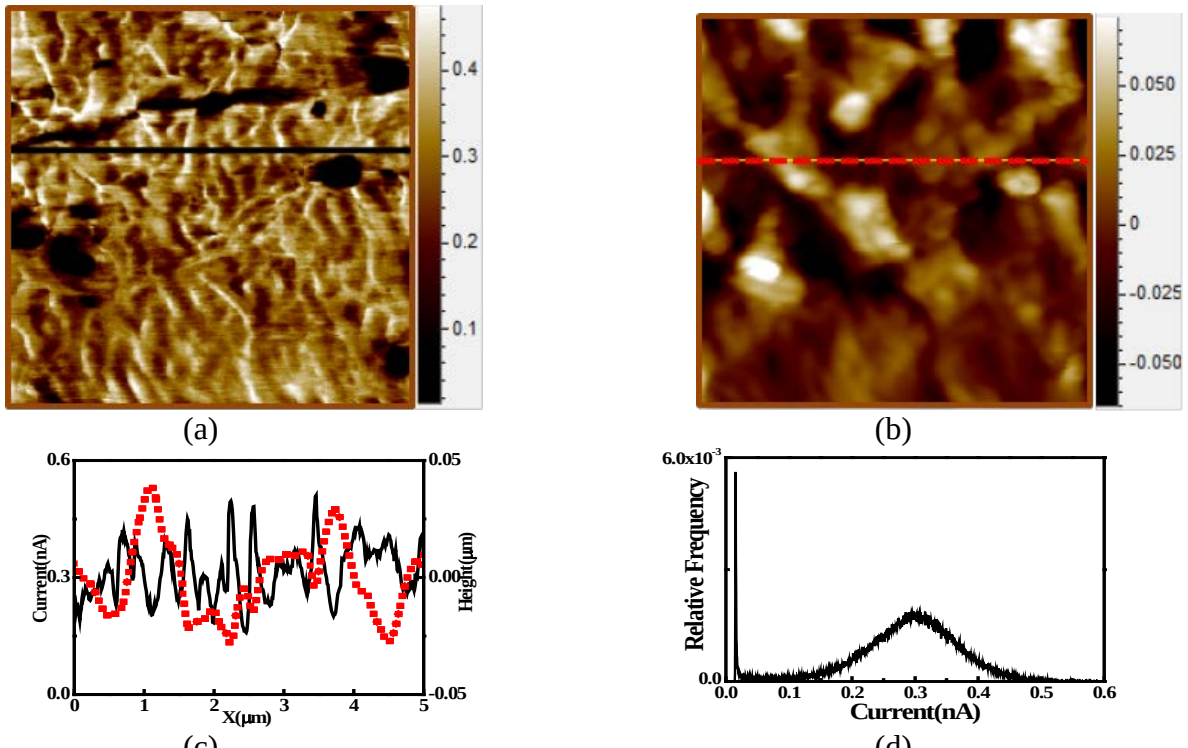

Figure 48. Nafion® 115 annealed at 110°C for 17 hours

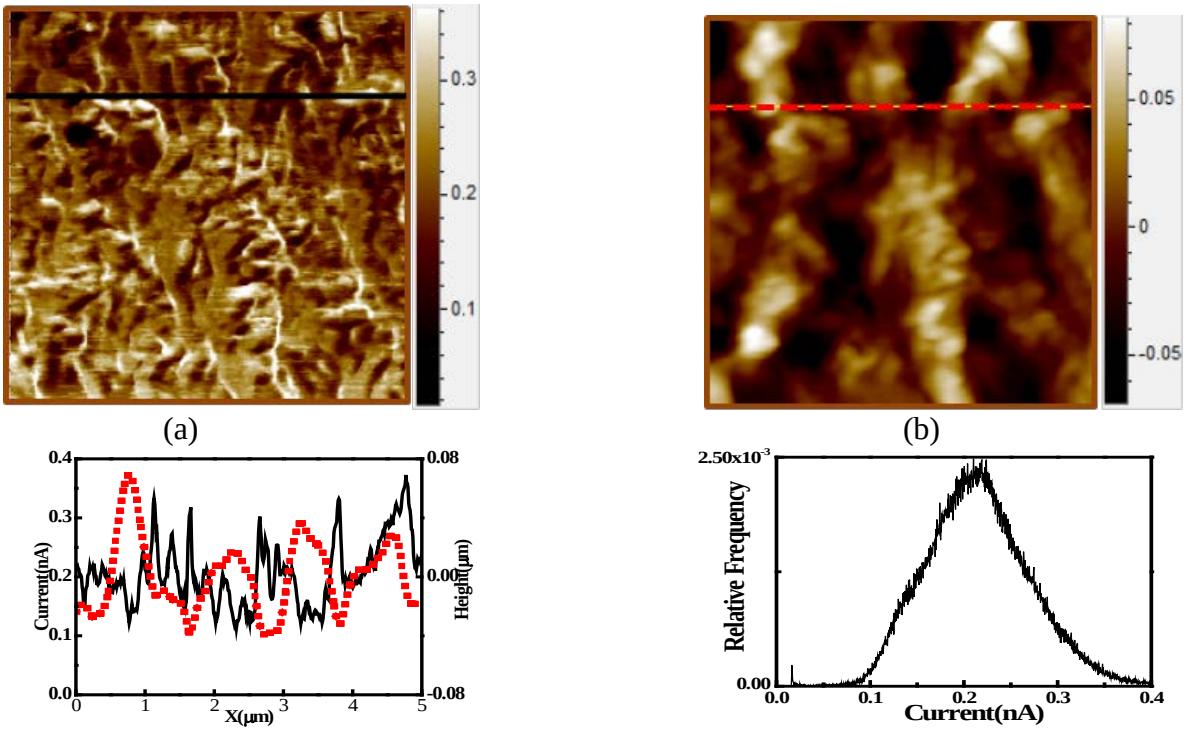

Figure 49. Nafion® 115 annealed at 110°C for 21 hours

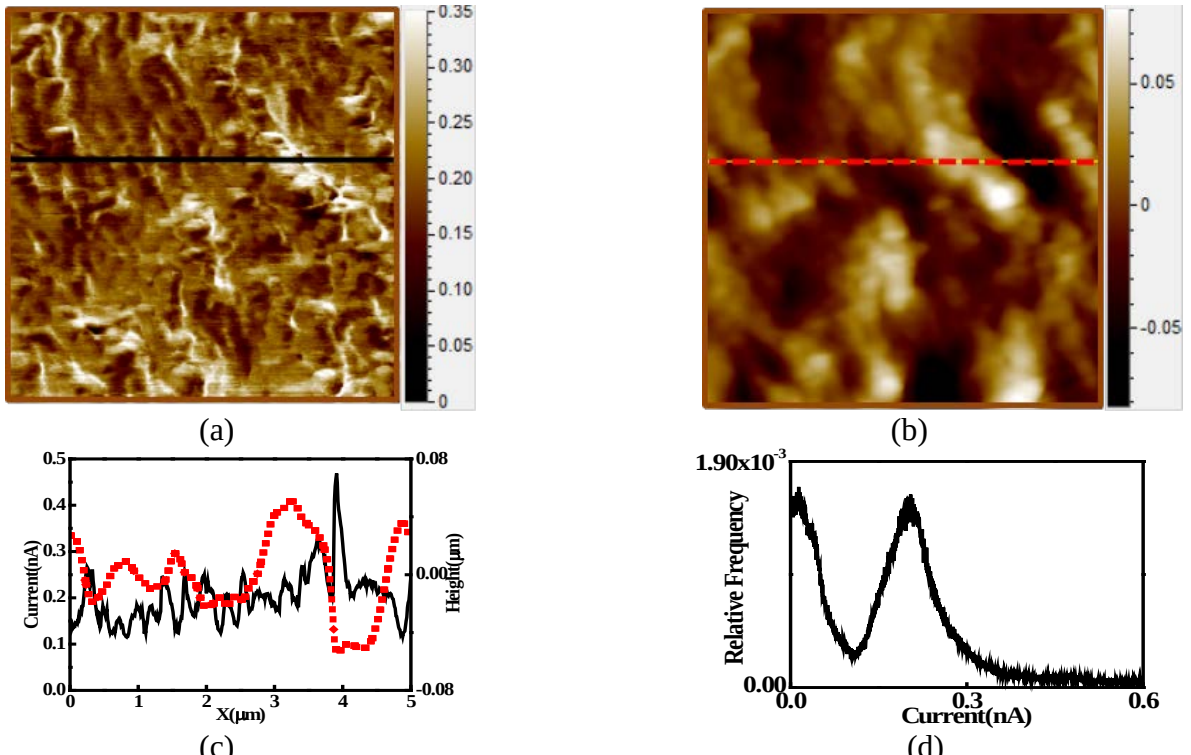

Figure 50. Nafion® 115 annealed at 110°C for 25 hours

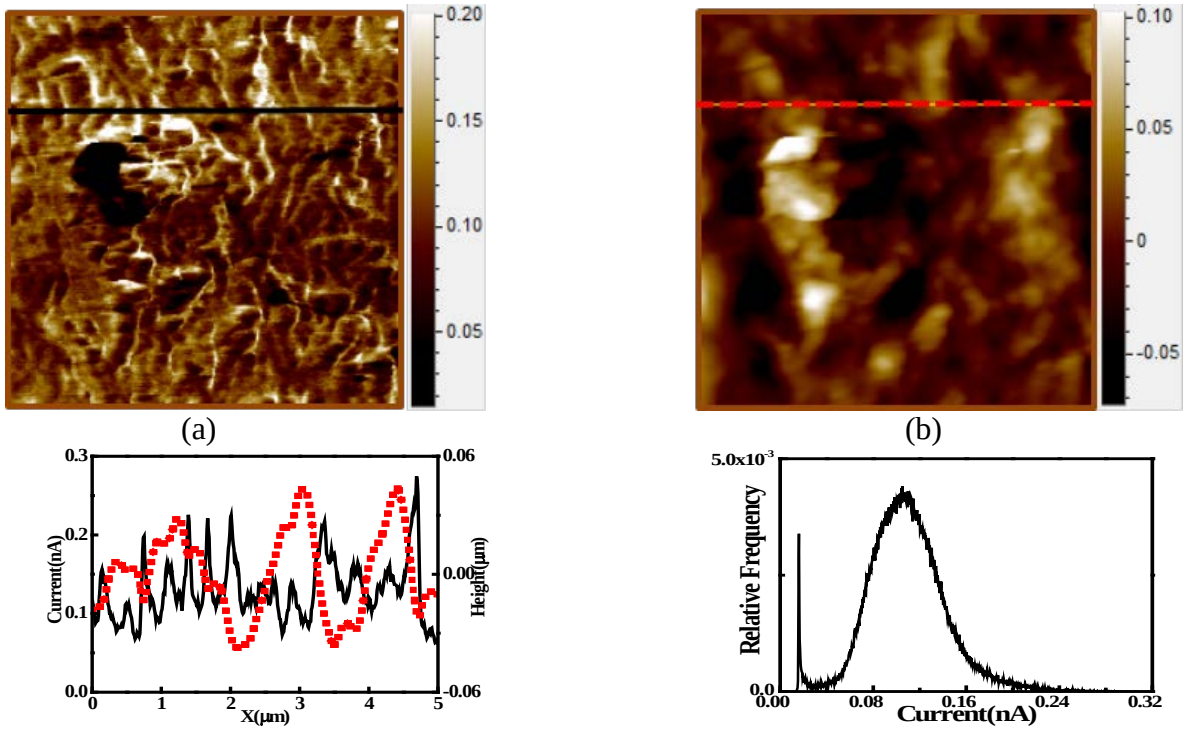

Figure 51. Nafion® 115 annealed at 110°C for 33 hours

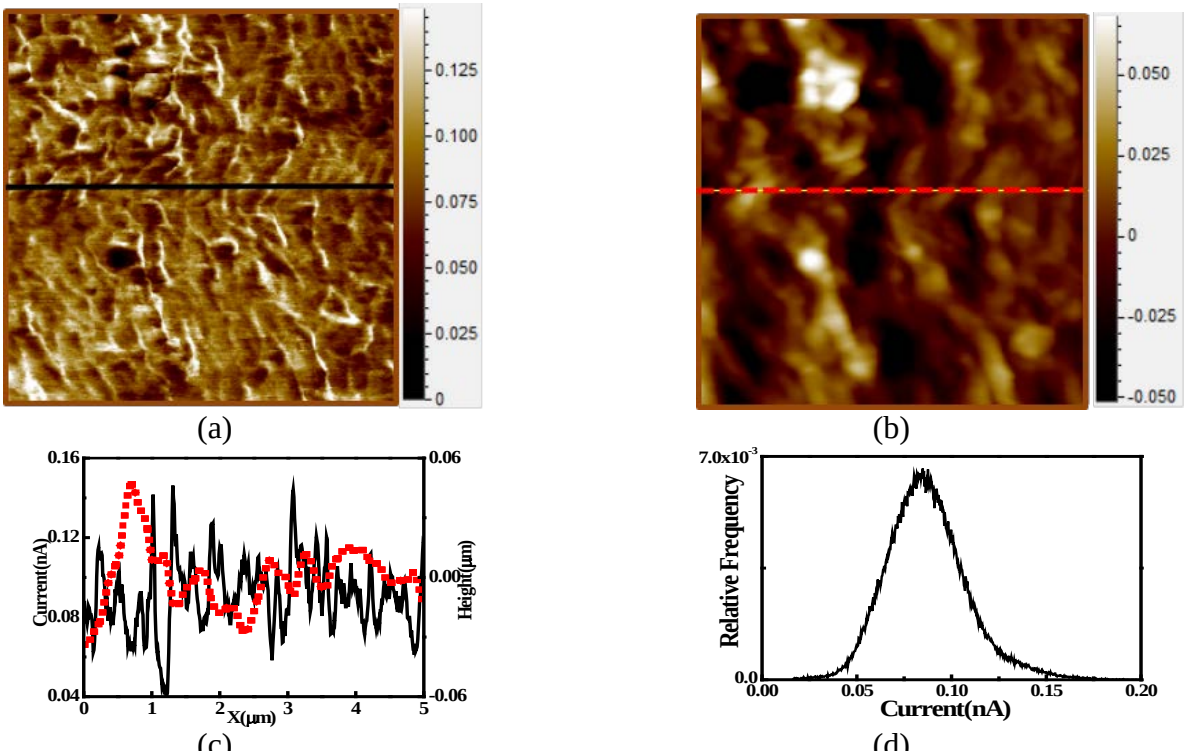

Figure 52. Nafion® 115 annealed at 110°C for 37 hours

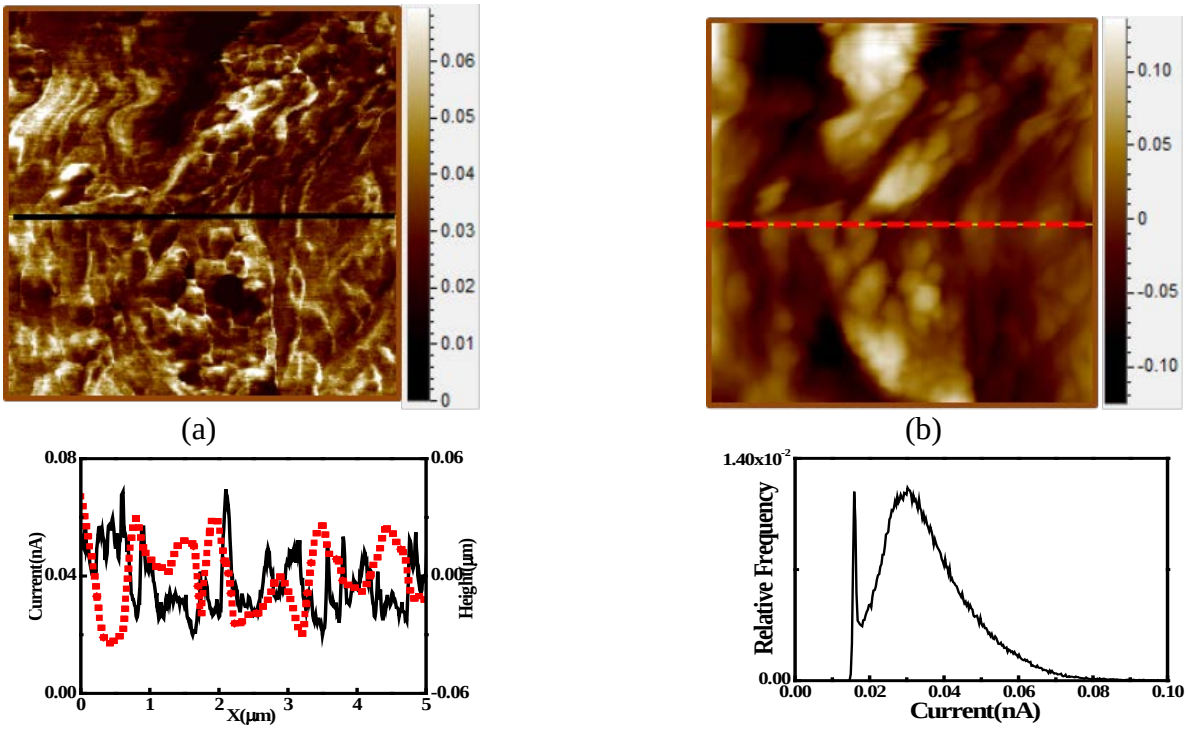

Figure 53. Nafion® 115 annealed at 110°C for 45 hours

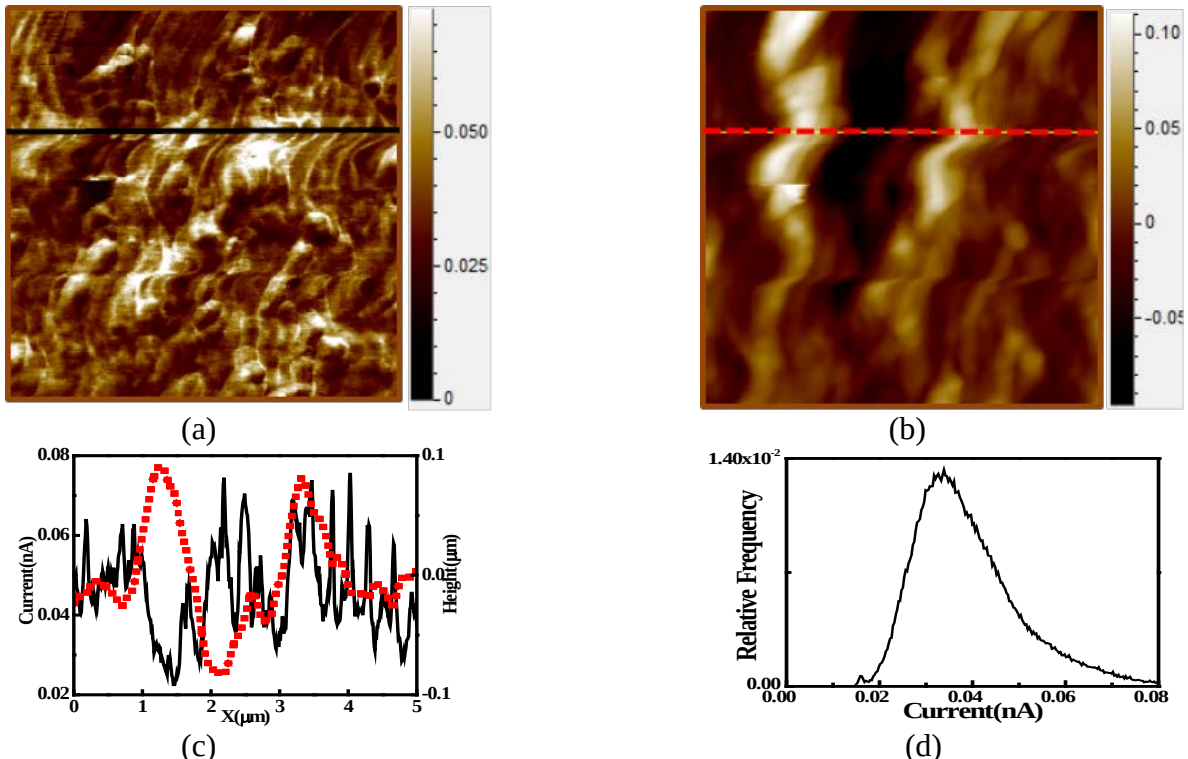

Figure 54. Nafion® 115 annealed at 110°C for 49 hours

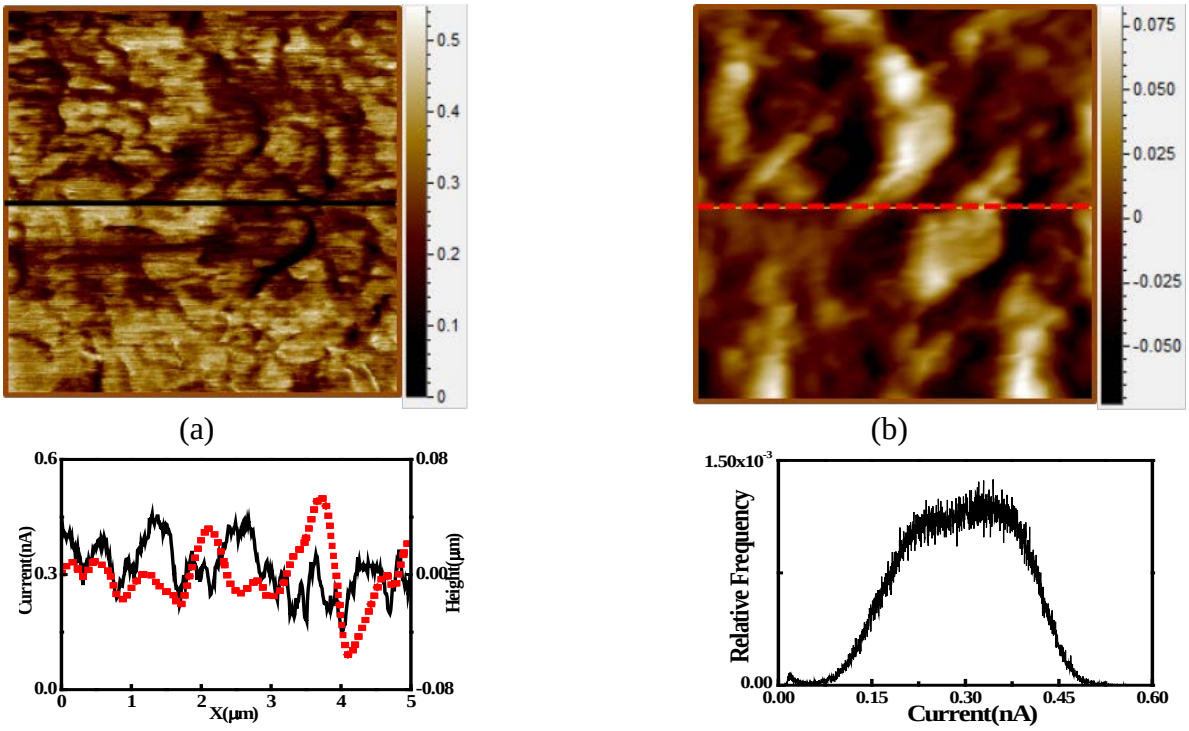

Figure 55. Nafion® 115, Pristine

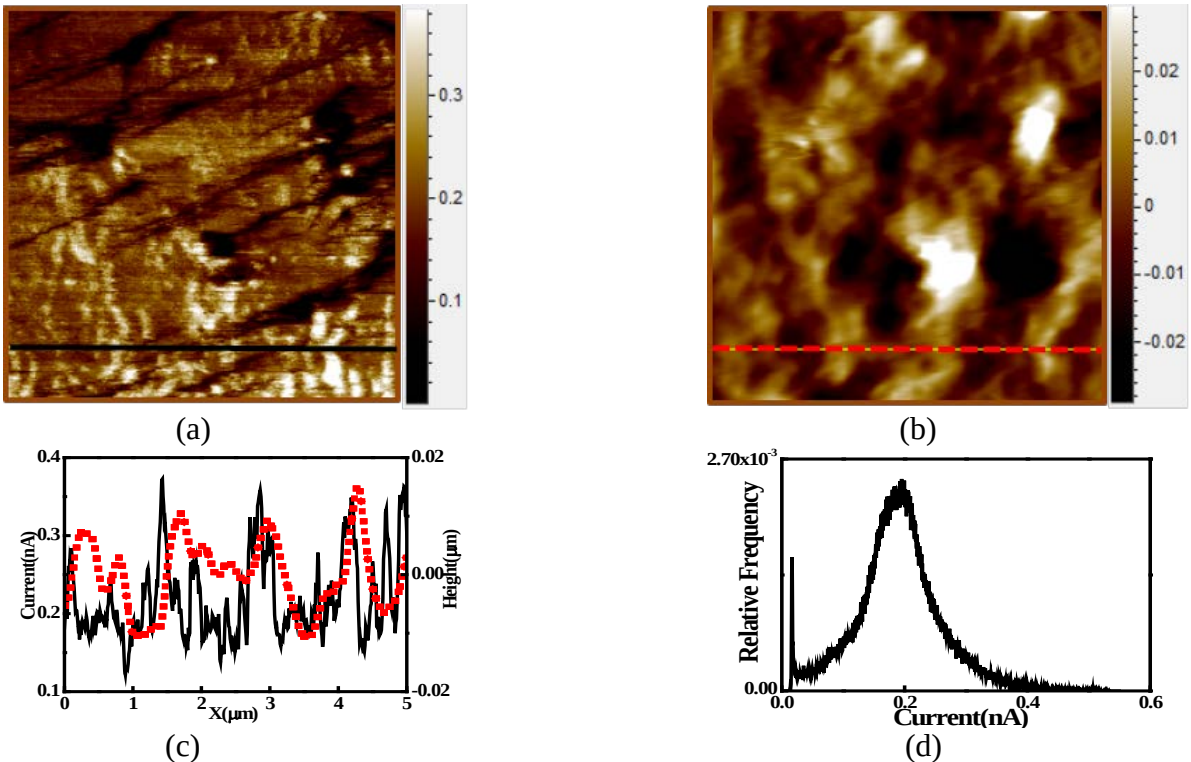

Figure 56. Nafion® 115 annealed at 120°C for 4 hours

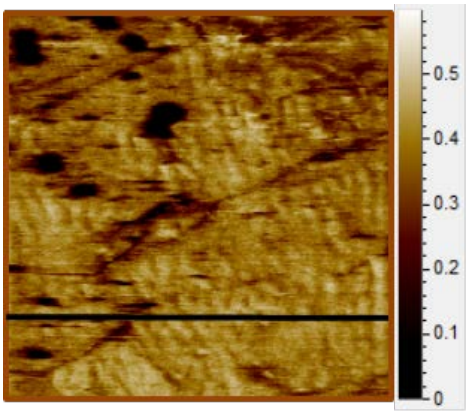

(a)

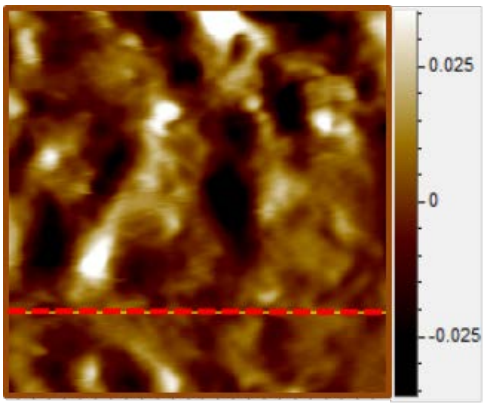

(b)

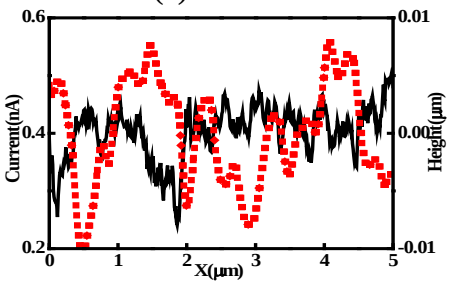

(c)

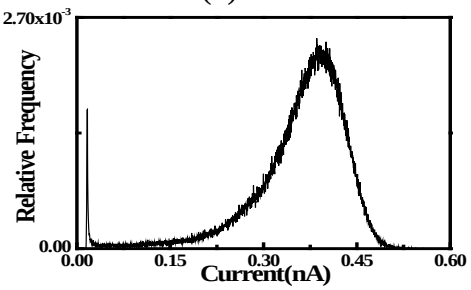

(d)

Figure 57. Nafion® 115 annealed at 120°C for 10 hours

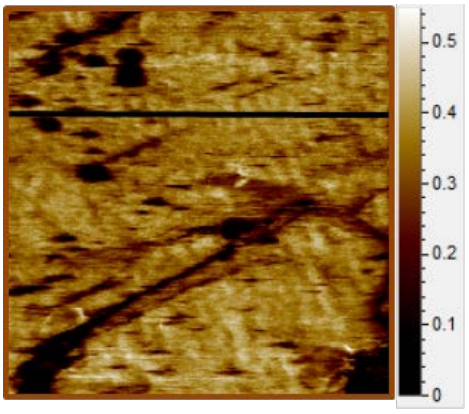

(a)

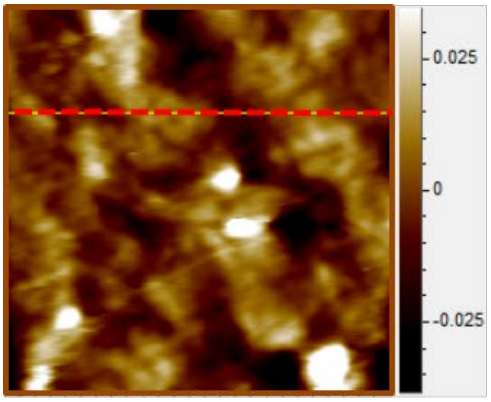

(b)

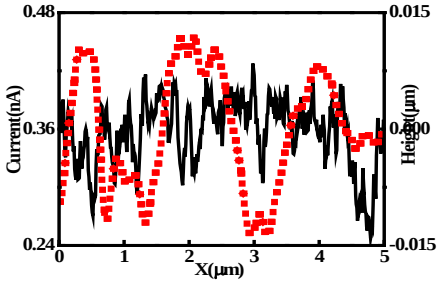

(c)

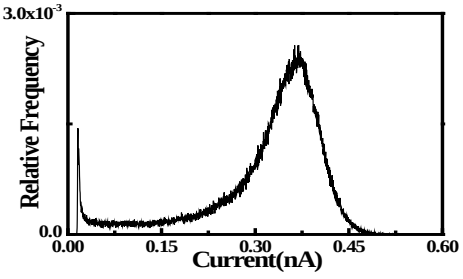

(d)

Figure 58. Nafion® 115 annealed at 120°C for 13 hours

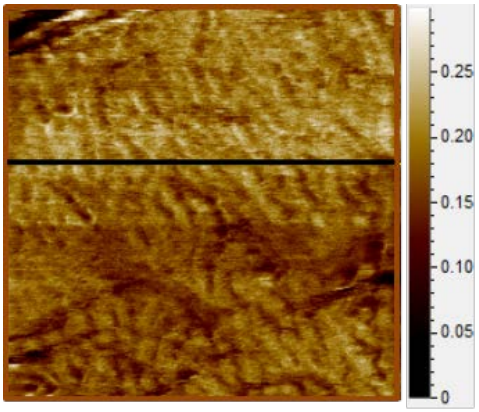

(a)

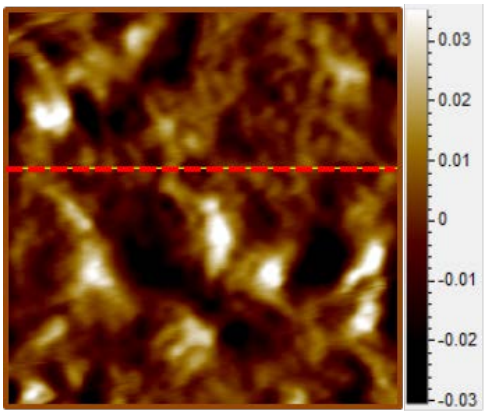

(b)

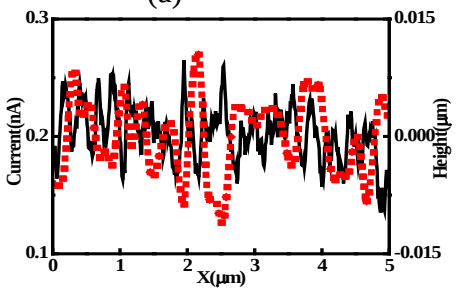

(c)

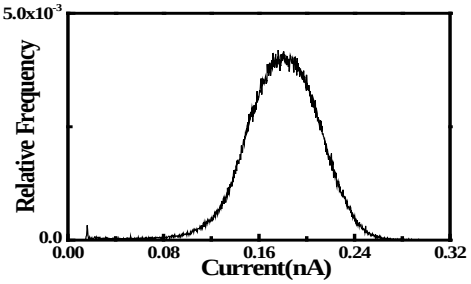

(d)

Figure 59. Nafion® 115 annealed at 120°C for 19 hours

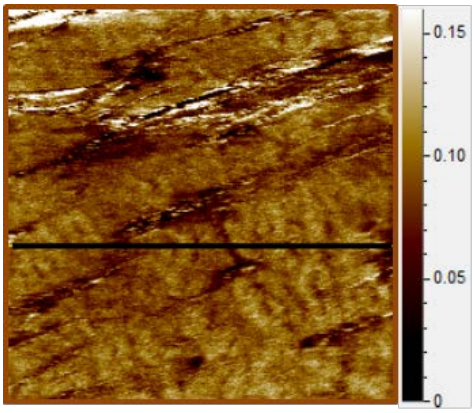

(a)

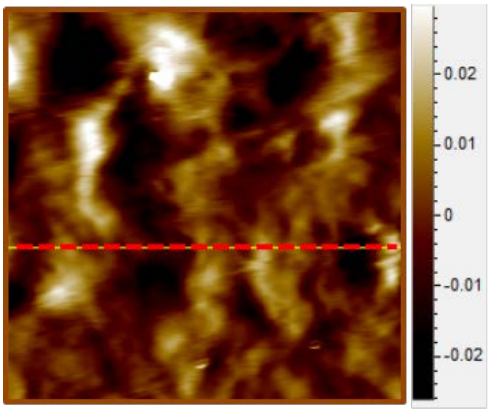

(b)

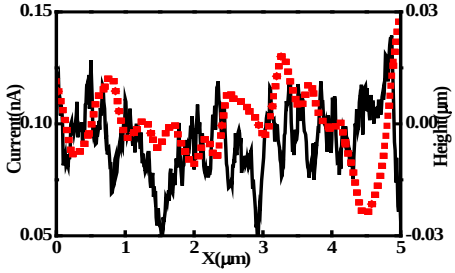

(c)

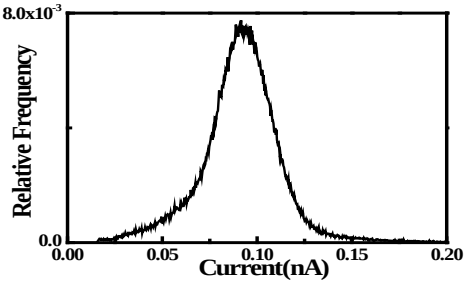

(d)

Figure 60. Nafion® 115 annealed at 120°C for 22 hours

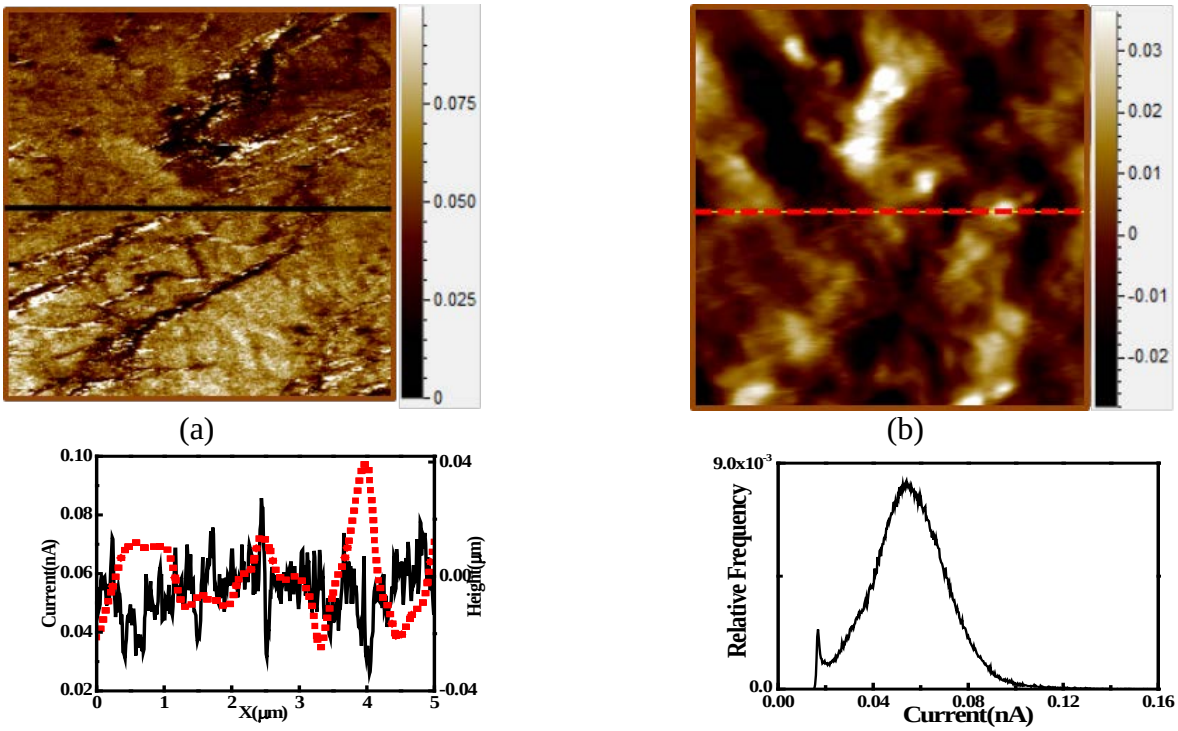

Figure 61. Nafion® 115 annealed at 120°C for 25 hours

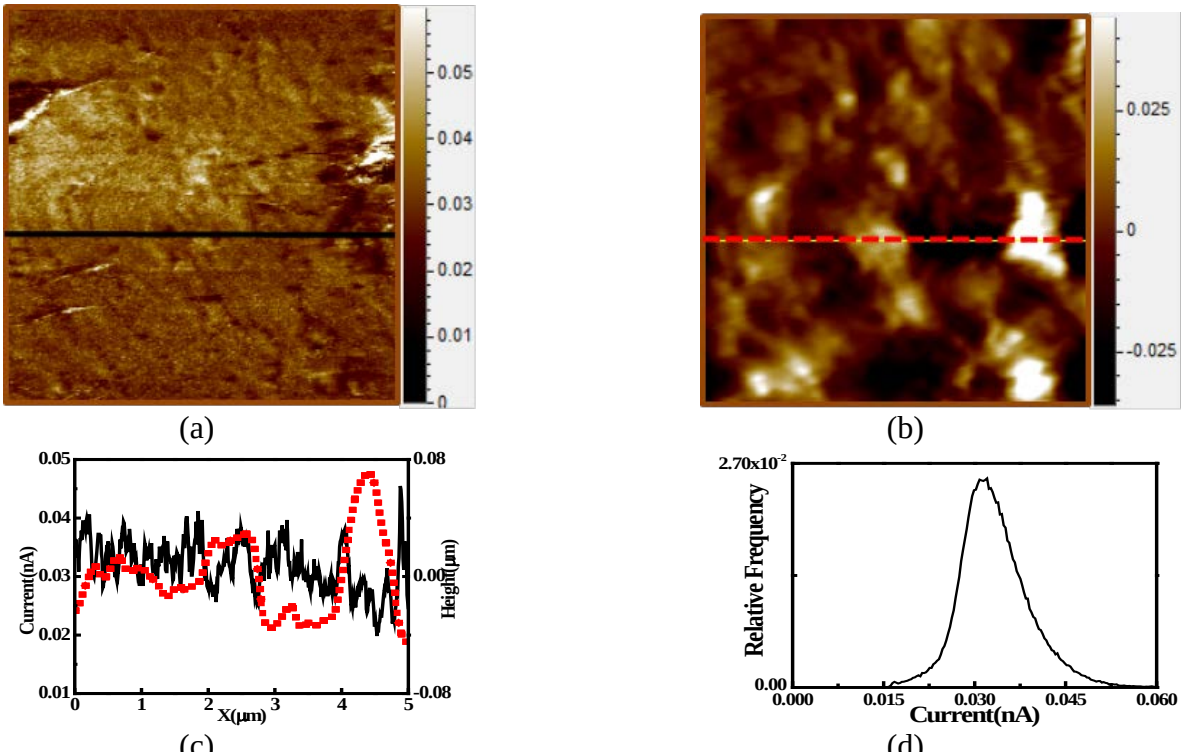

Figure 62. Nafion® 115 annealed at 120°C for 34 hours

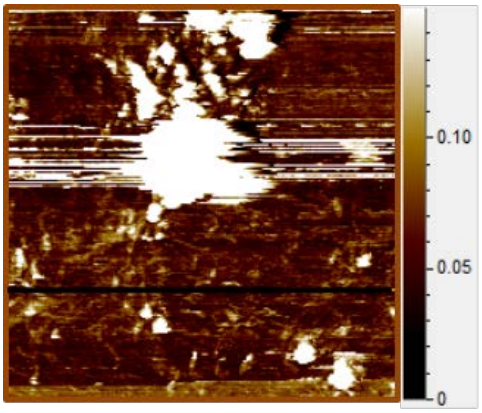

(a)

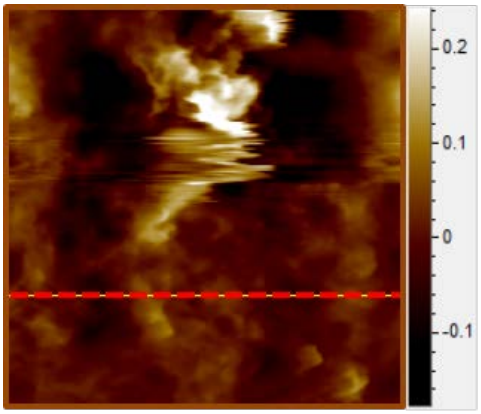

(b)

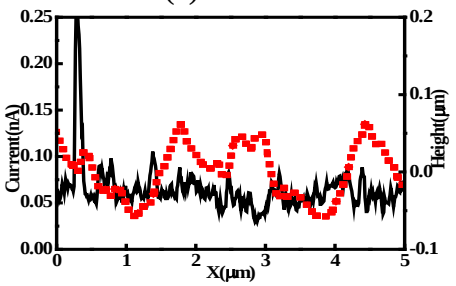

(c)

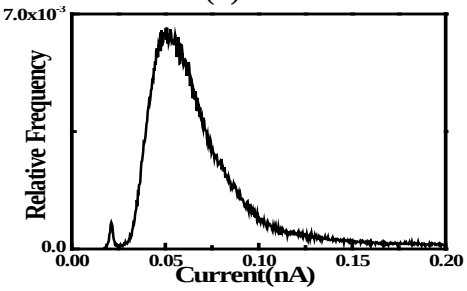

(d)

Figure 63. Nafion® 212, Pristine

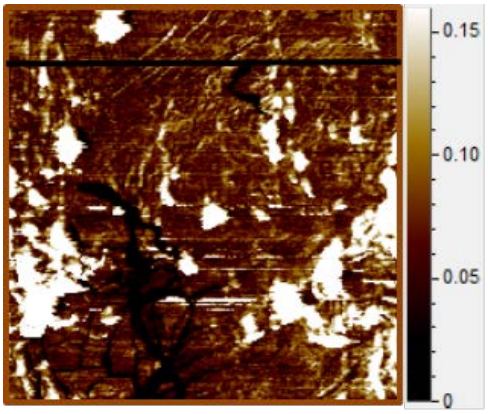

(a)

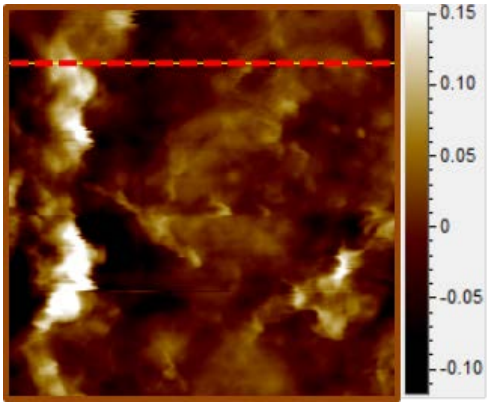

(b)

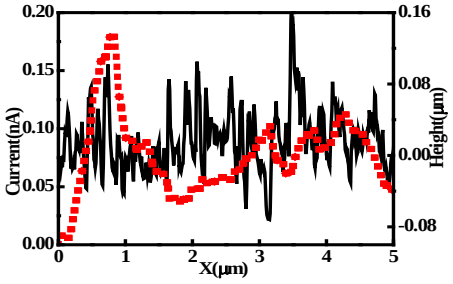

(c)

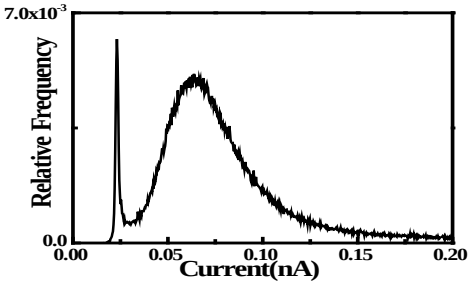

(d)

Figure 64. Nafion® 212 annealed at 90°C for 5 hours

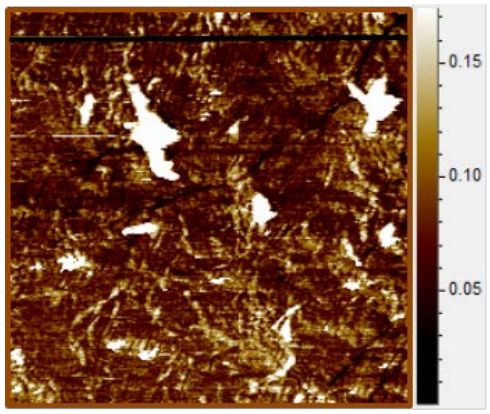

(a)

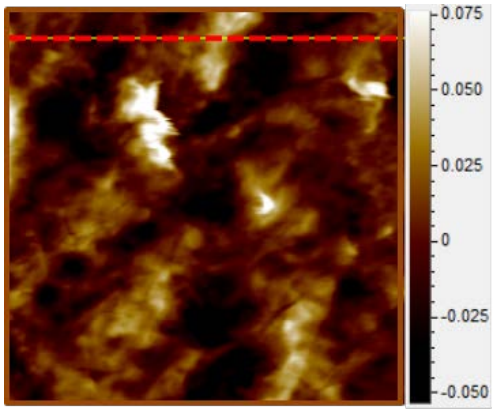

(b)

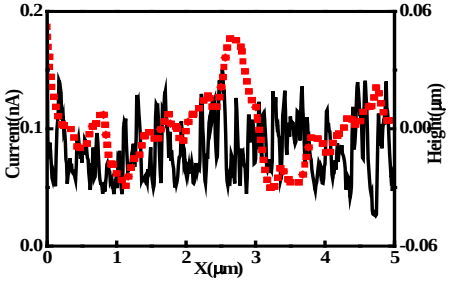

(c)

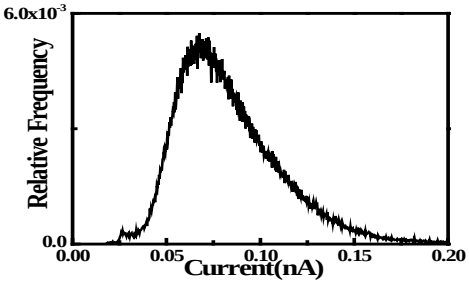

(d)

Figure 65. Nafion® 212 annealed at 90°C for 19 hours

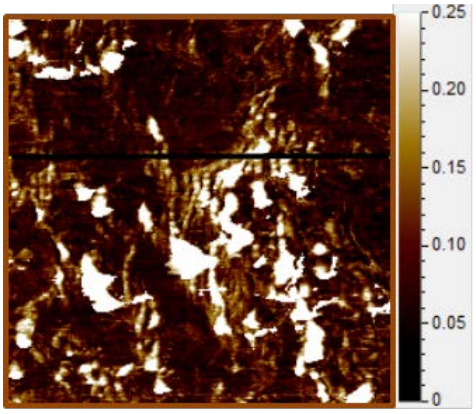

(a)

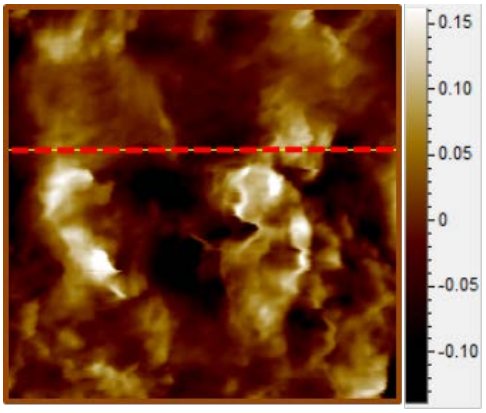

(b)

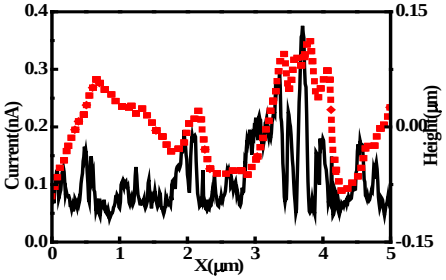

(c)

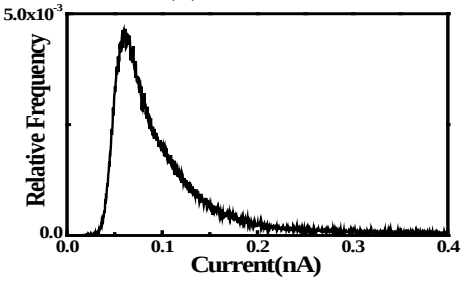

(d)

Figure 66. Nafion® 212 annealed at 90°C for 26 hours

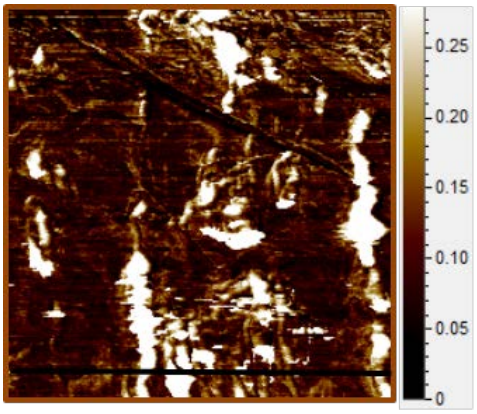

(a)

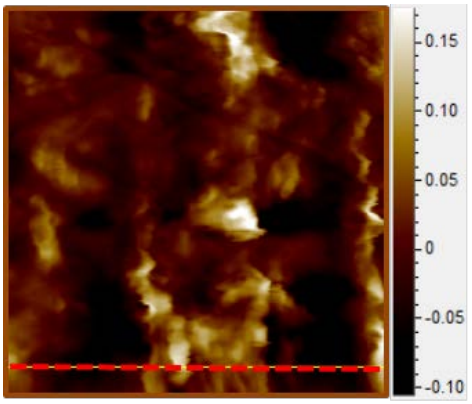

(b)

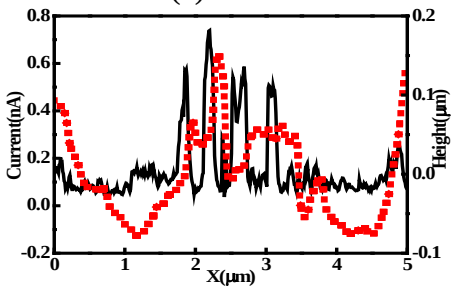

(c)

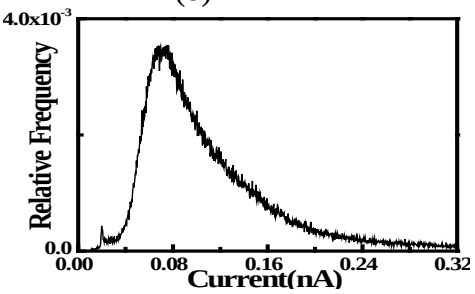

(d)

Figure 67. Nafion® 212 annealed at 90°C for 37 hours

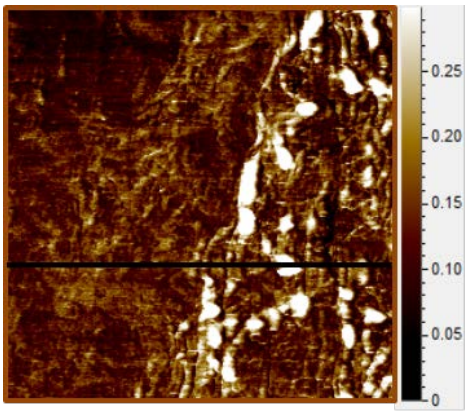

(a)

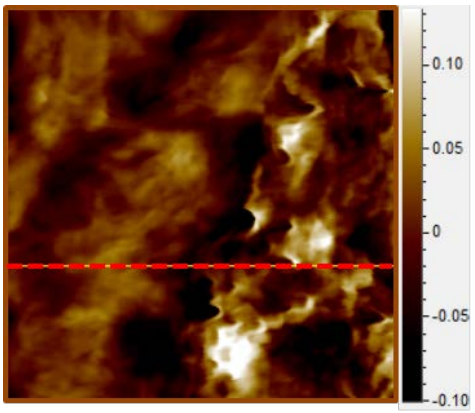

(b)

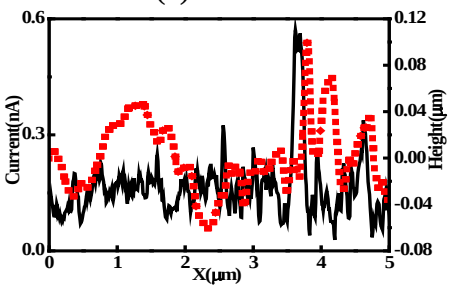

(c)

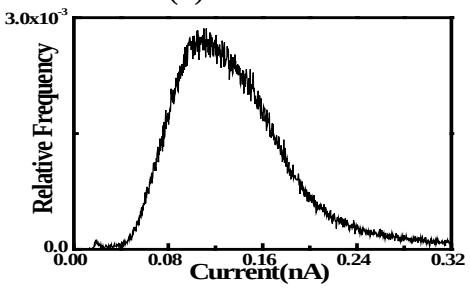

(d)

Figure 68. Nafion® 212 annealed at 90°C for 60 hours

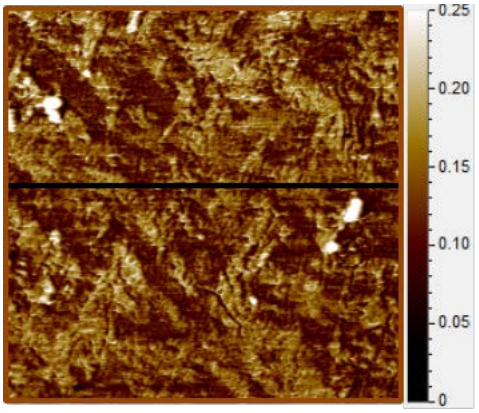

(a)

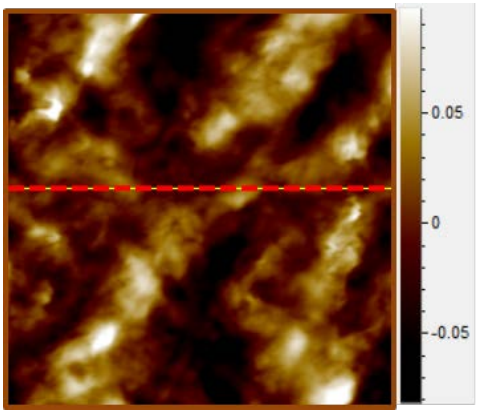

(b)

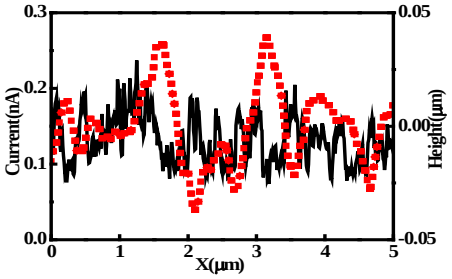

(c)

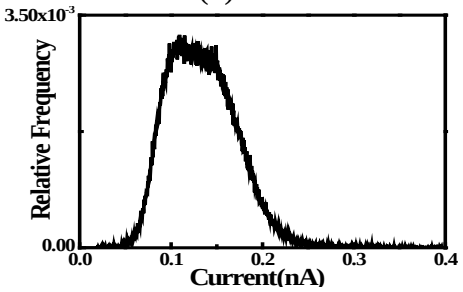

(d)

Figure 69. Nafion® 212 annealed at 90°C for 70 hours

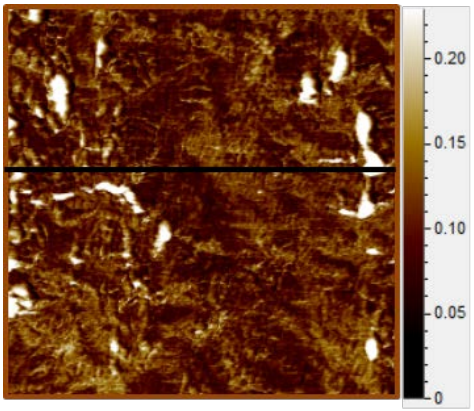

(a)

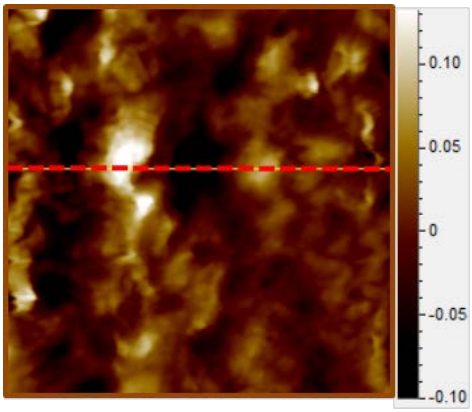

(b)

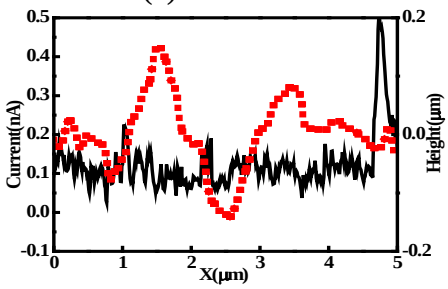

(c)

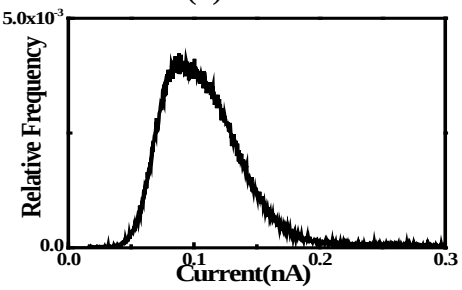

(d)

Figure 70. Nafion® 212 annealed at 90°C for 89 hours

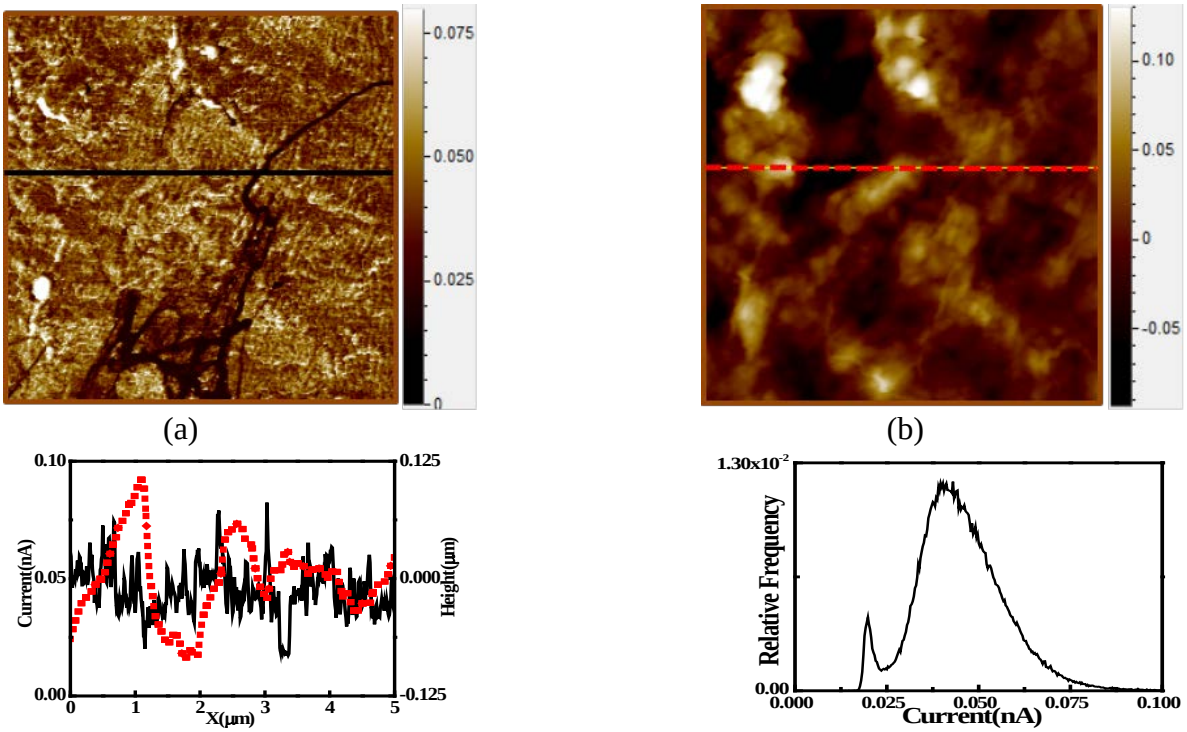

Figure 71. Nafion® 212 annealed at 90°C for 99 hours

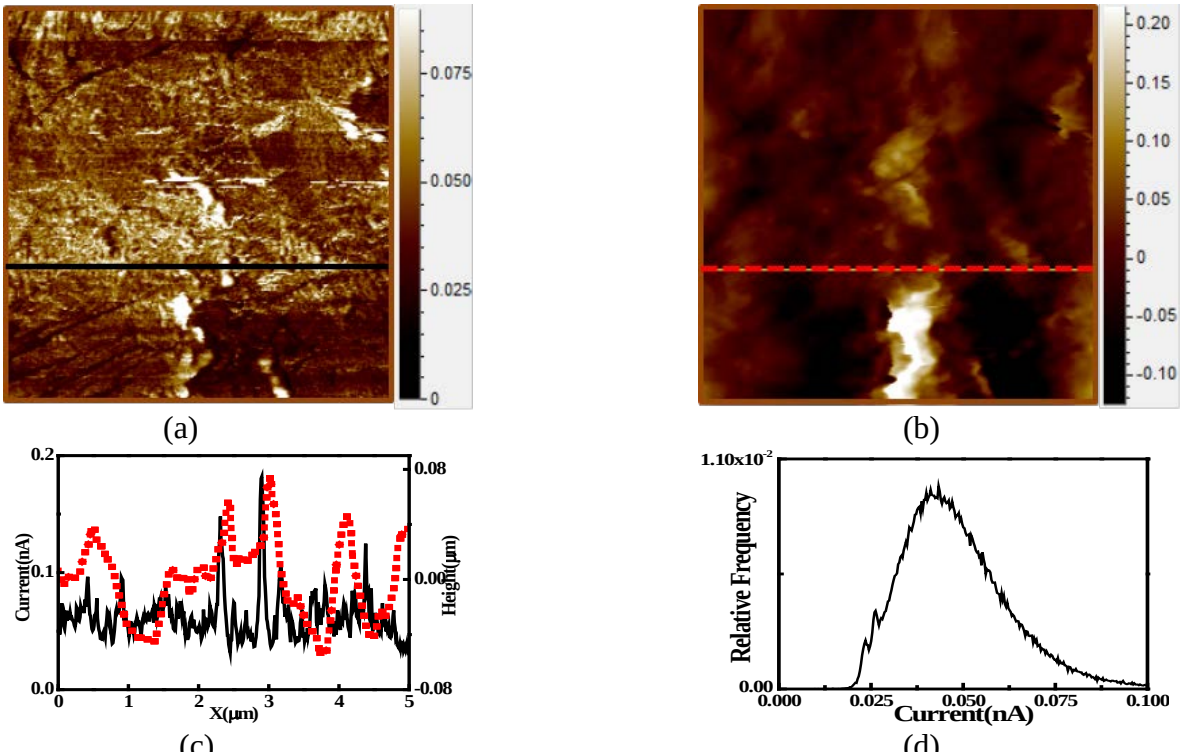

Figure 72. Nafion® 212 annealed at 90°C for 105 hours

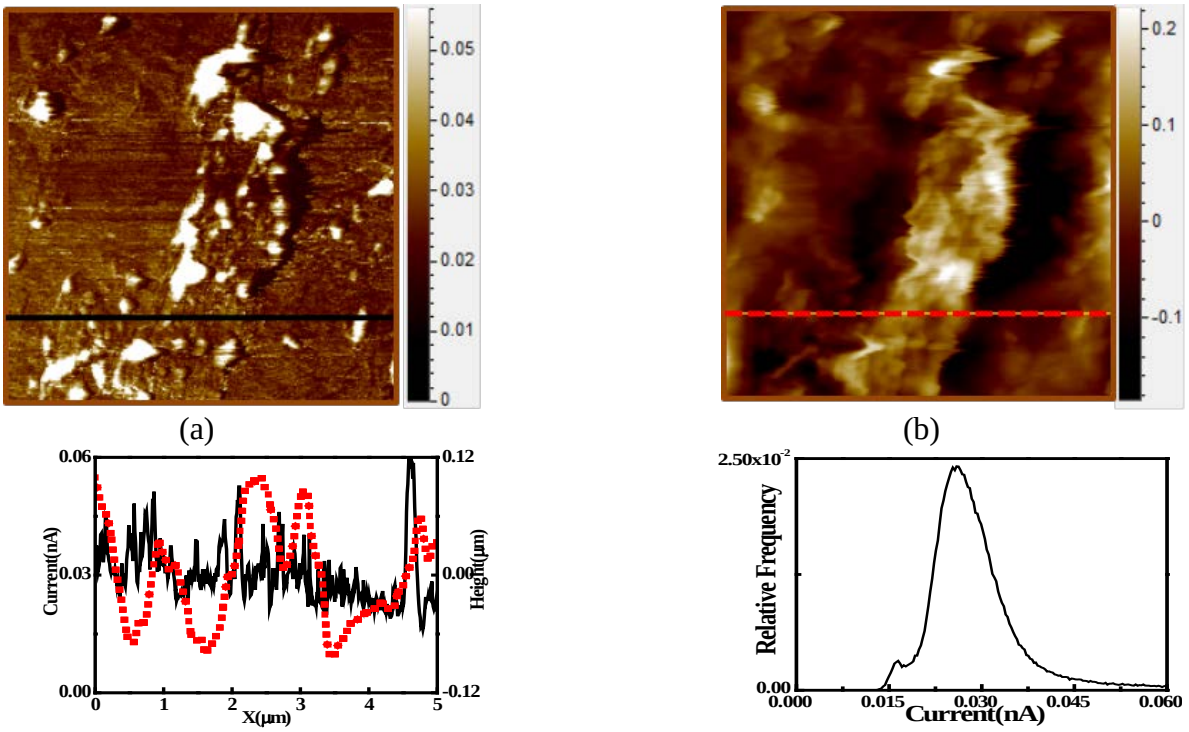

Figure 73. Nafion® 212 annealed at 90°C for 115 hours

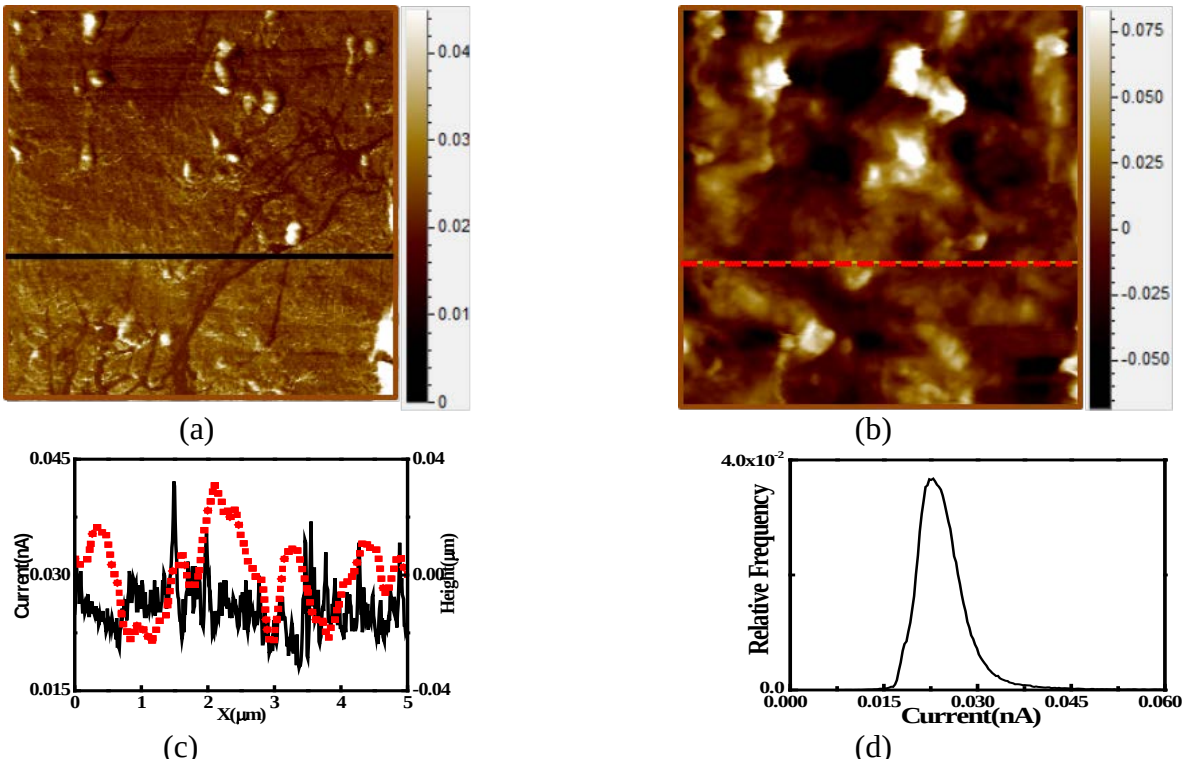

Figure 74. Nafion® 212 annealed at 90°C for 122 hours

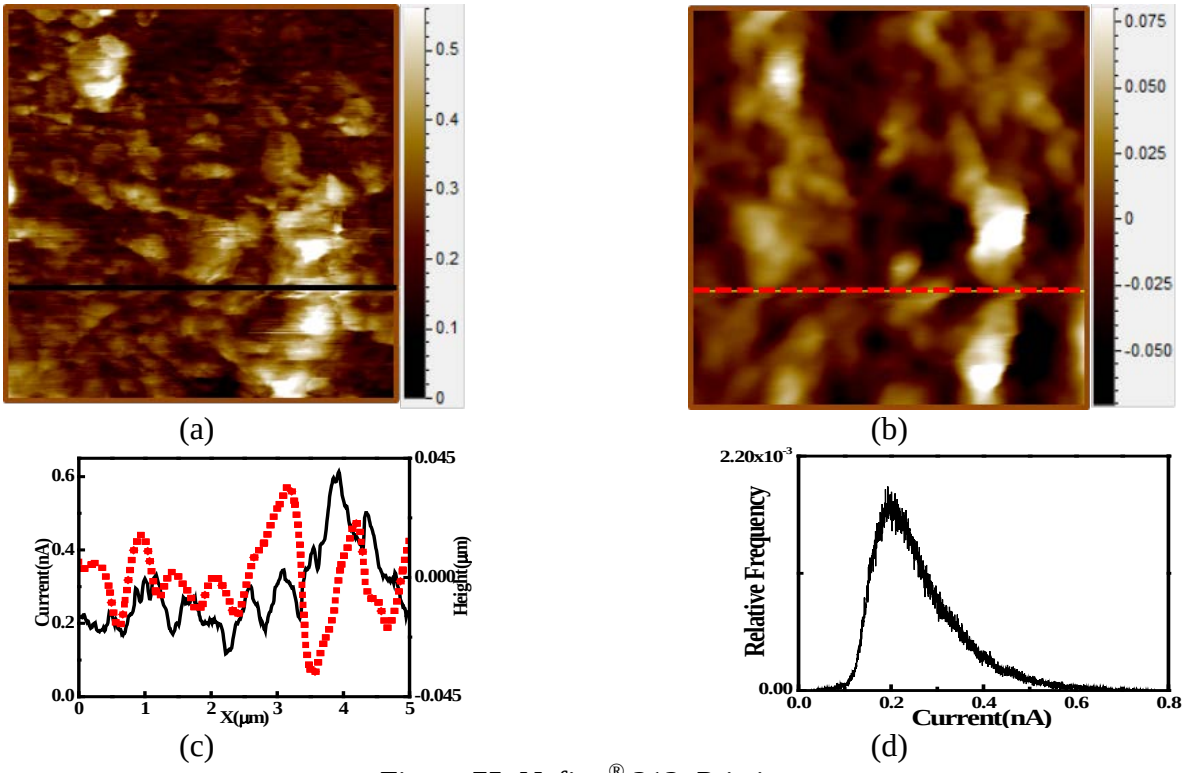

Figure 75. Nafion® 212, Pristine

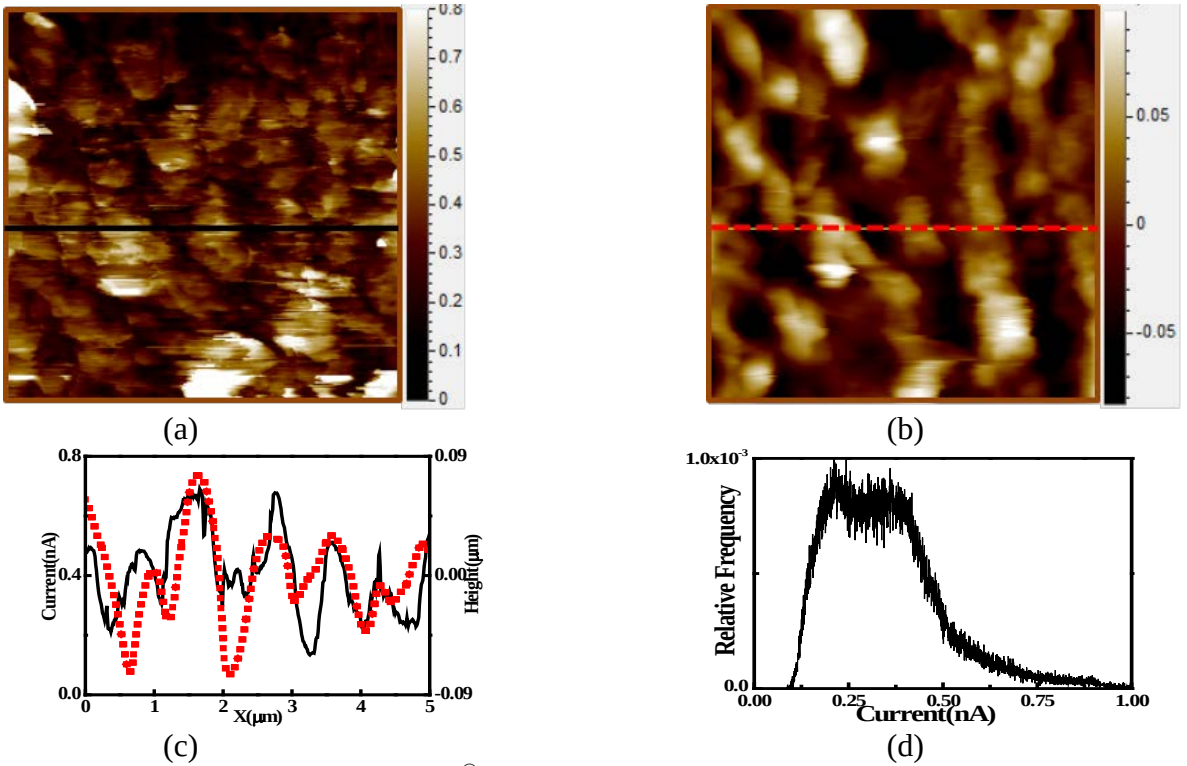

Figure 76. Nafion® 212 annealed at 100°C for 10 hours

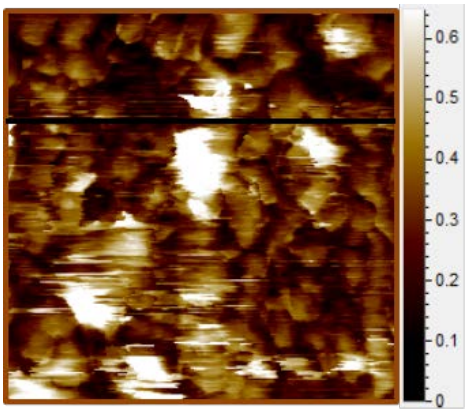

(a)

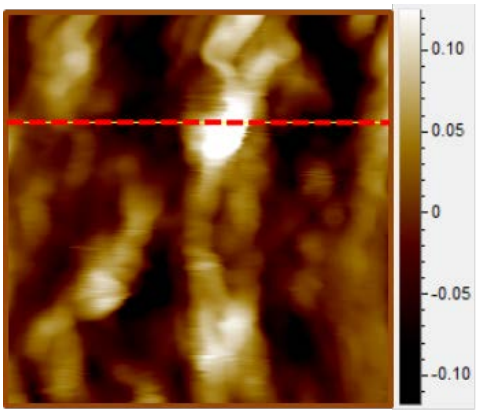

(b)

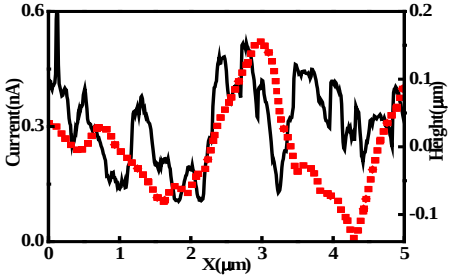

(c)

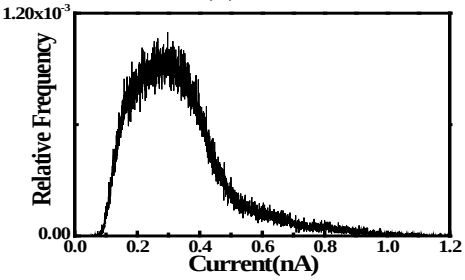

(d)

Figure 77. Nafion® 212 annealed at 100°C for 15 hours

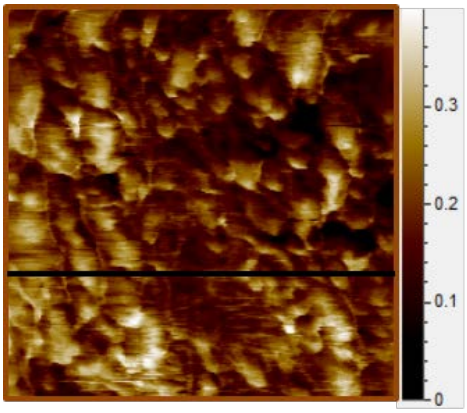

(a)

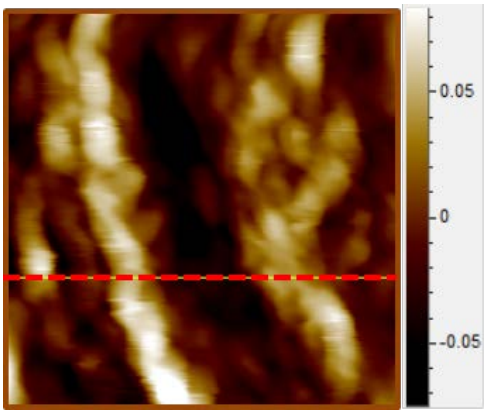

(b)

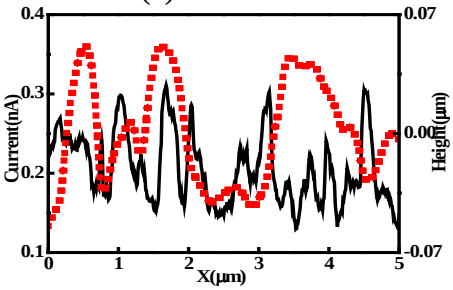

(c)

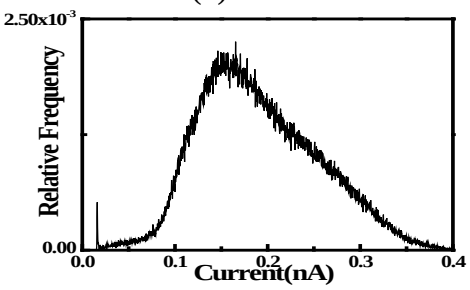

(d)

Figure 78. Nafion® 212 annealed at 100°C for 31 hours

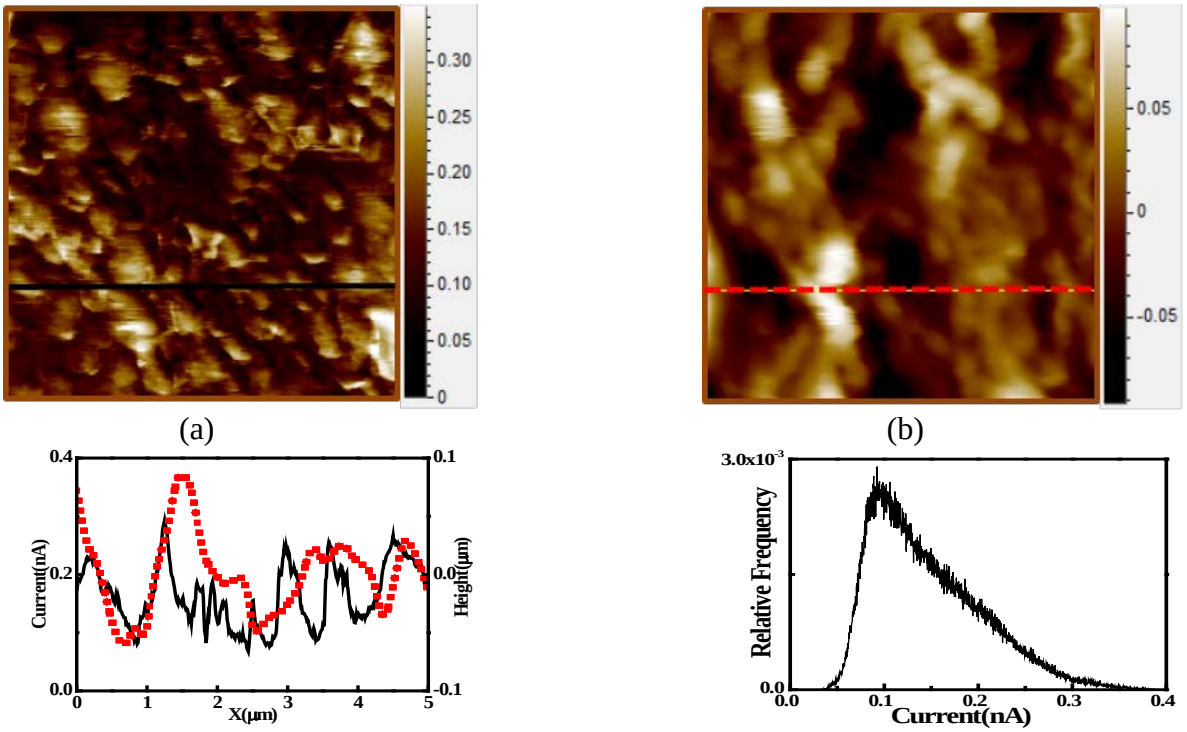

Figure 79. Nafion® 212 annealed at 100°C for 41 hours

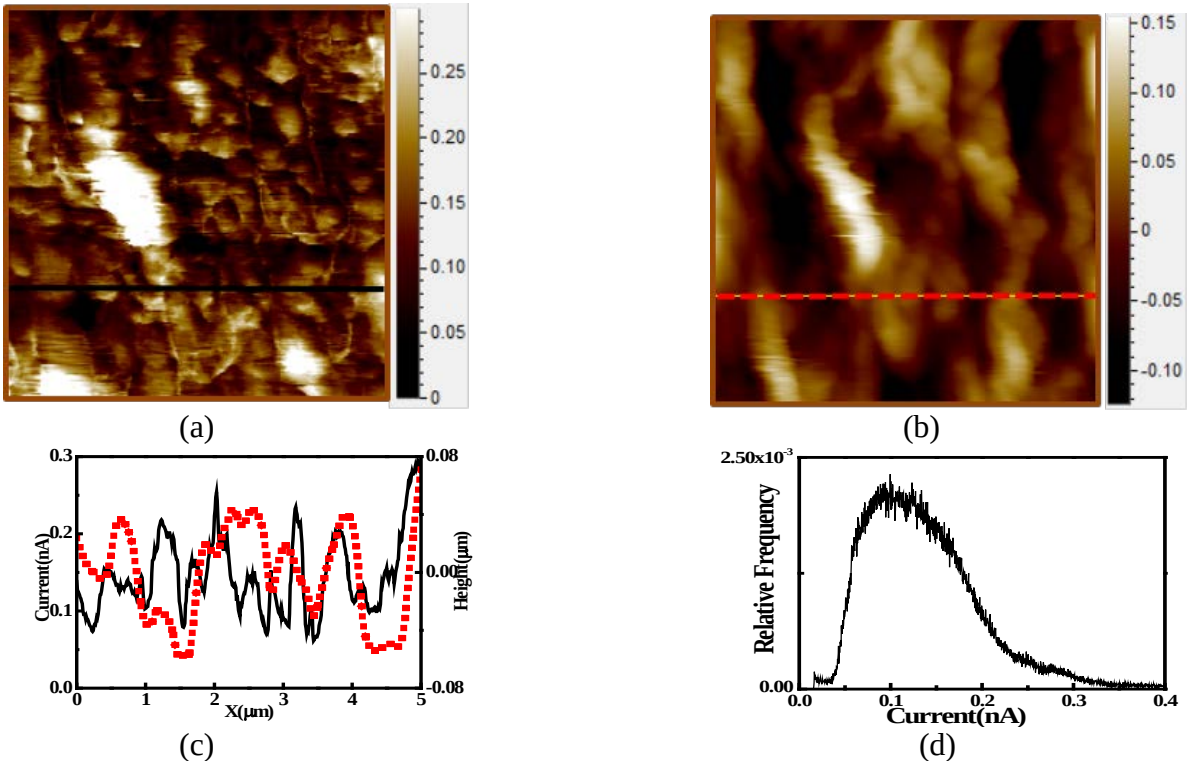

Figure 80. Nafion® 212 annealed at 100°C for 46 hours

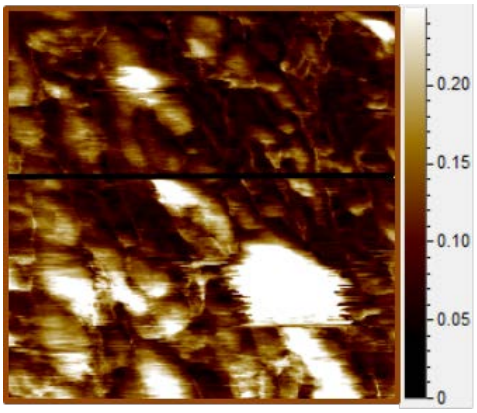

(a)

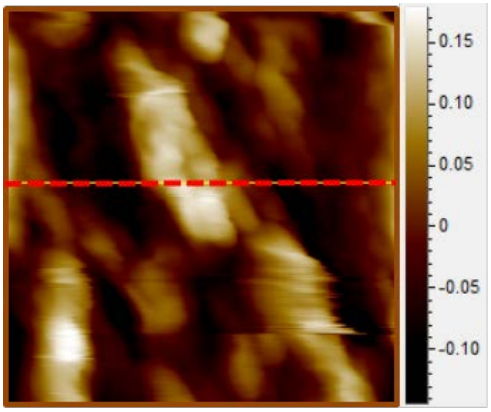

(b)

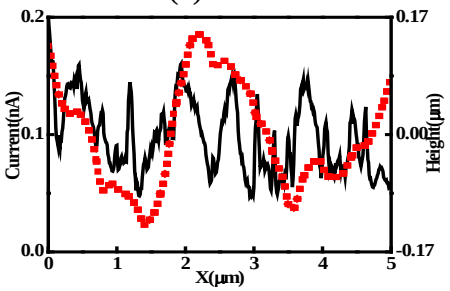

(c)

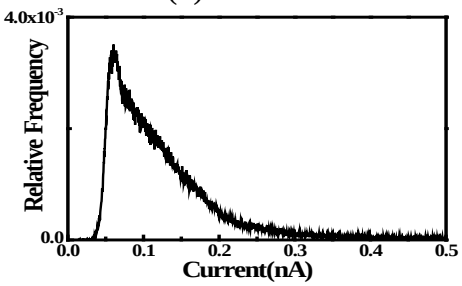

(d)

Figure 81. Nafion® 212 annealed at 100°C for 51 hours

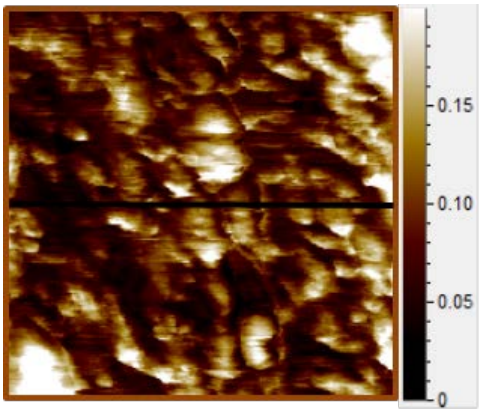

(a)

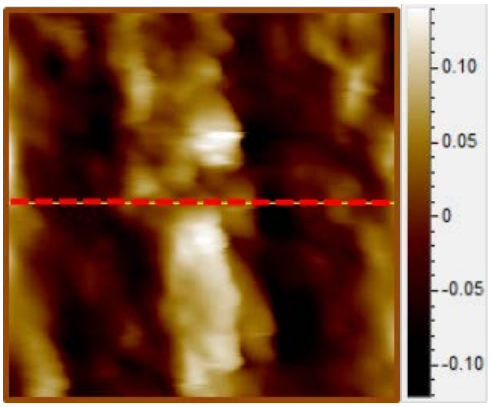

(b)

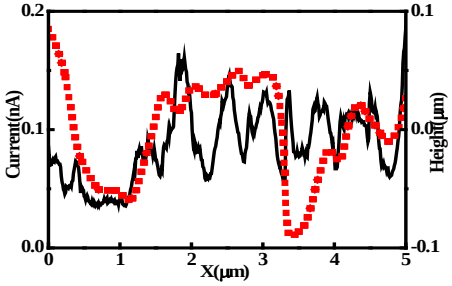

(c)

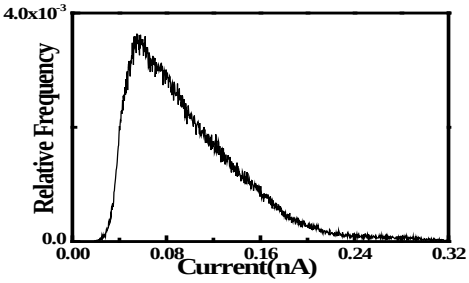

(d)

Figure 82. Nafion® 212 annealed at 100°C for 56 hours

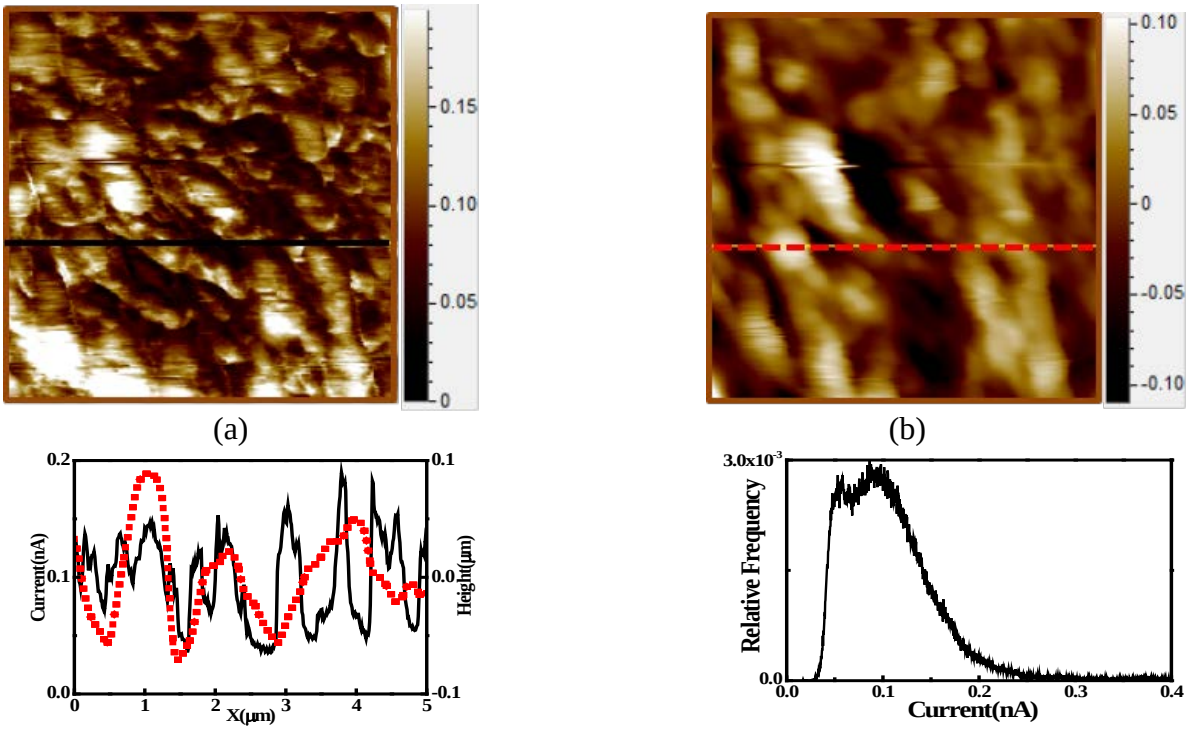

Figure 83. Nafion® 212 annealed at 100°C for 61 hours

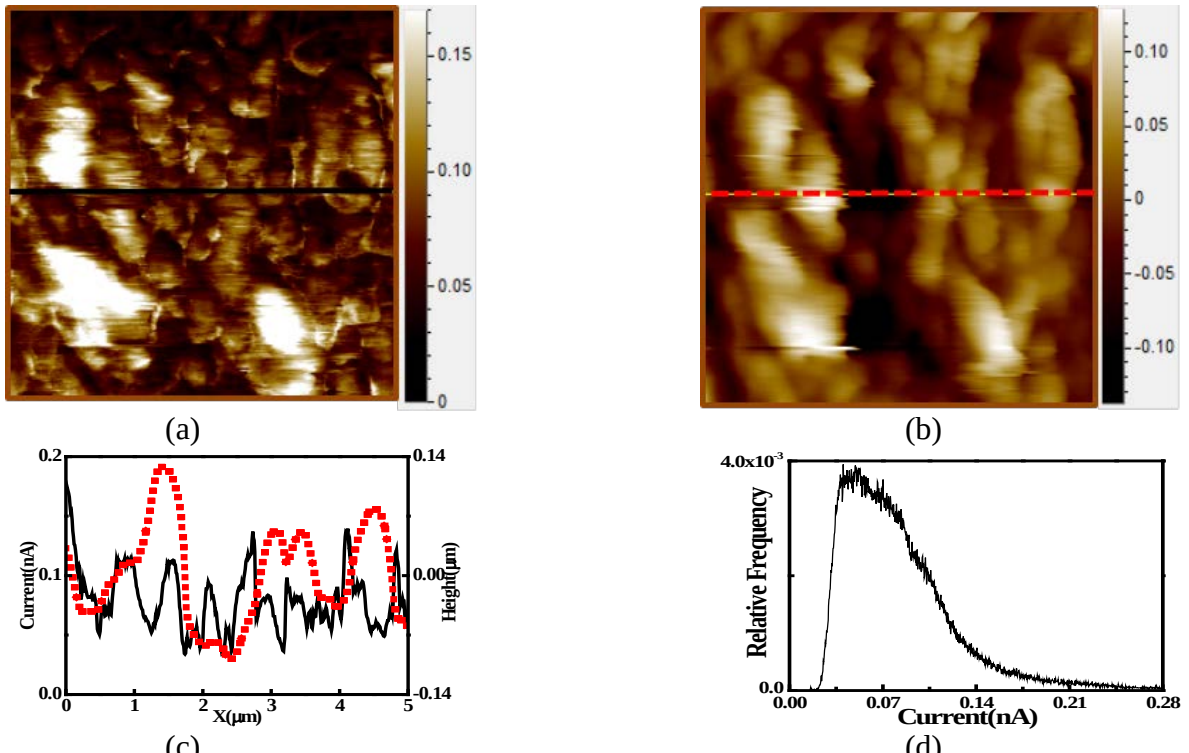

Figure 84. Nafion® 212 annealed at 100°C for 66 hours

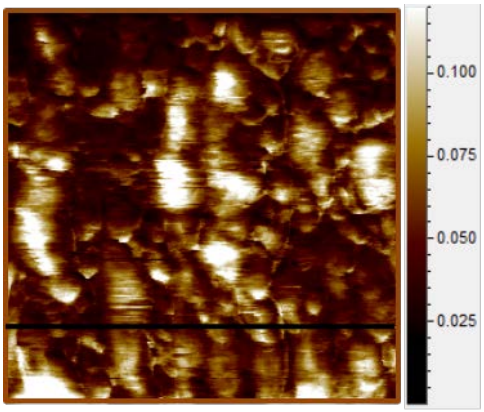

(a)

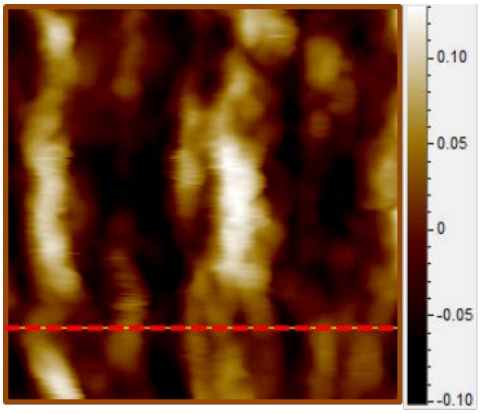

(b)

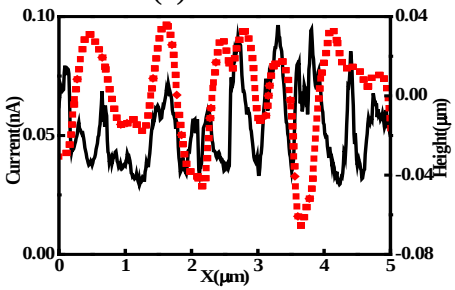

(c)

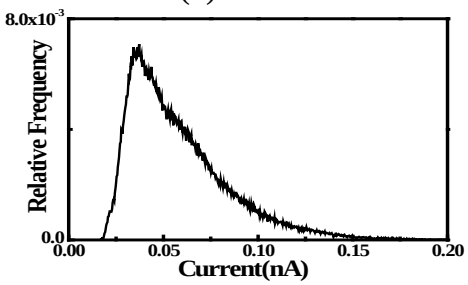

(d)

Figure 85. Nafion® 212 annealed at 100°C for 76 hours

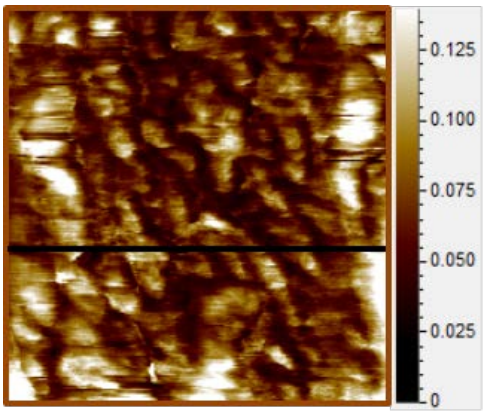

(a)

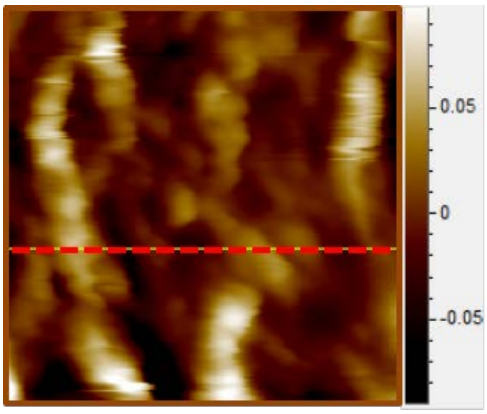

(b)

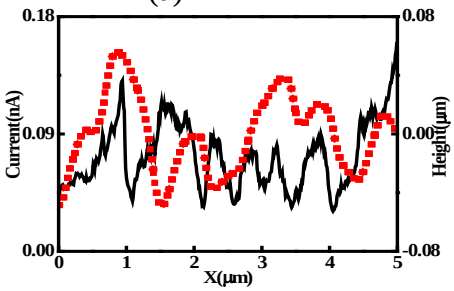

(c)

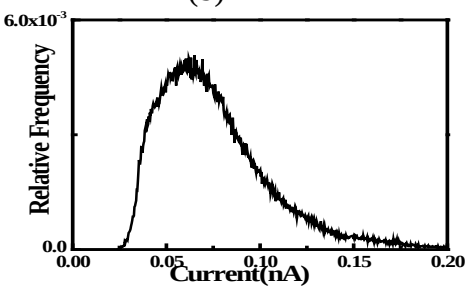

(d)

Figure 86. Nafion® 212 annealed at 100°C for 86 hours

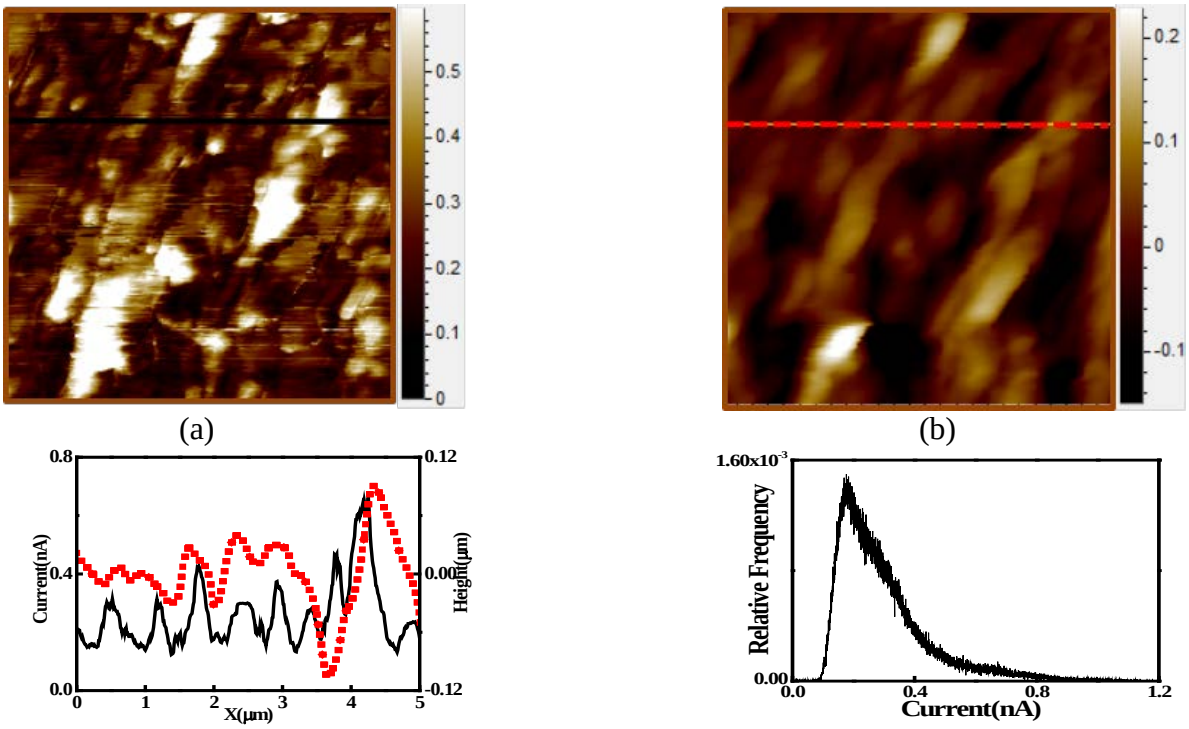

Figure 87. Nafion® 212, Pristine

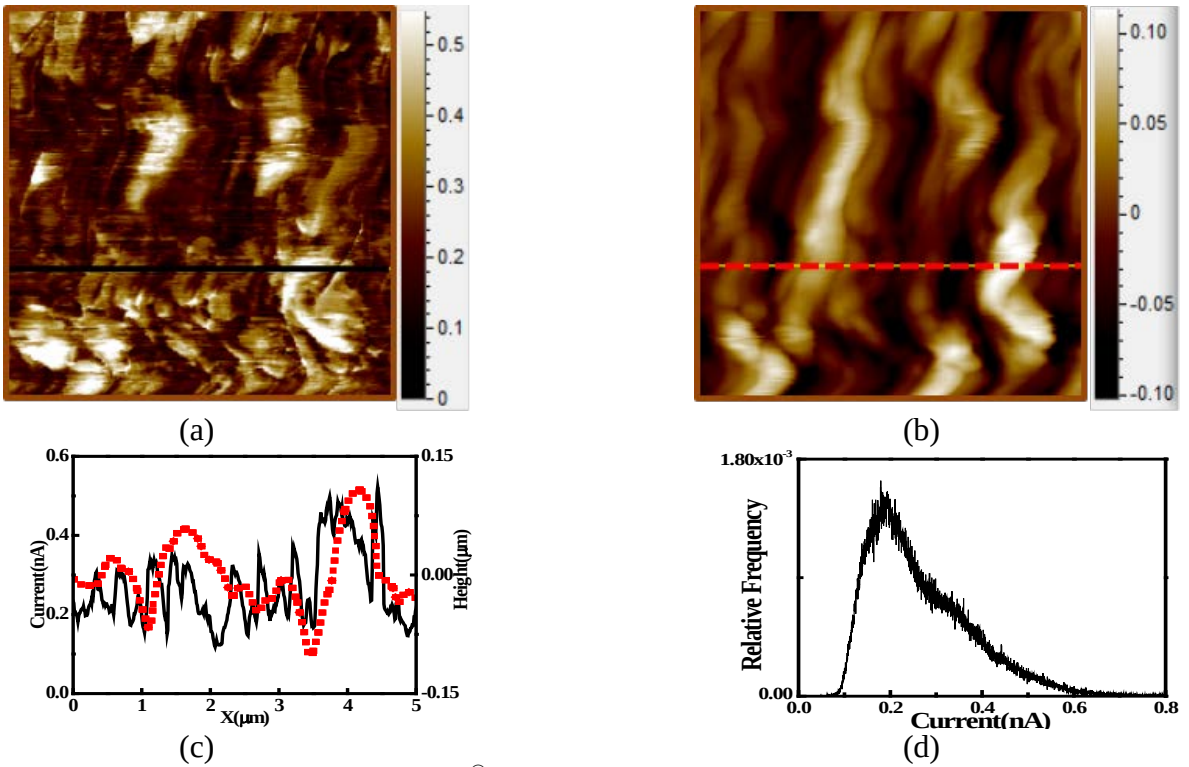

Figure 88. Nafion® 212 annealed at 110°C for 8 hours

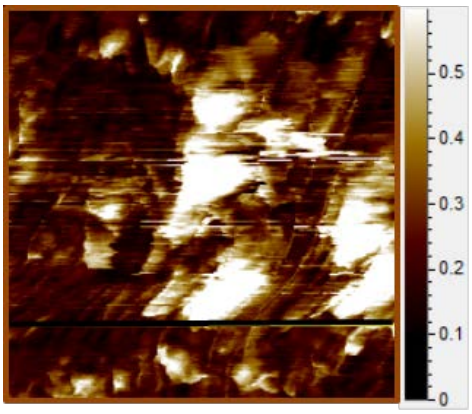

(a)

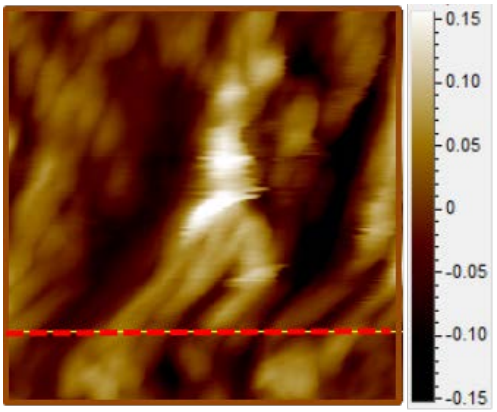

(b)

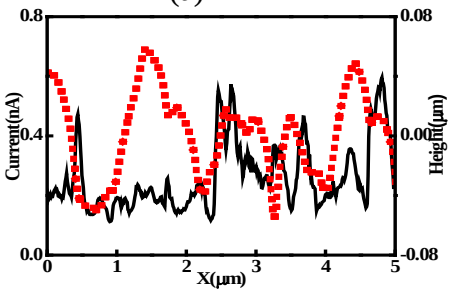

(c)

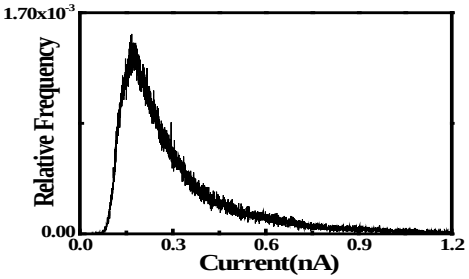

(c)

Figure 89. Nafion® 212 annealed at 110°C for 11 hours

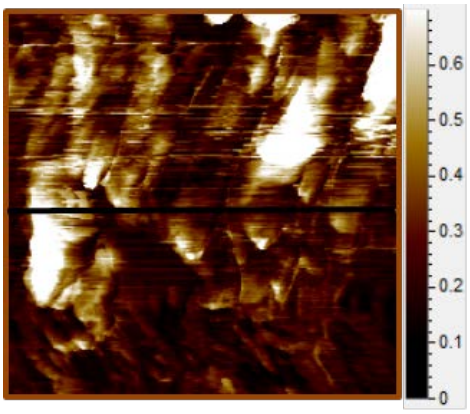

(a)

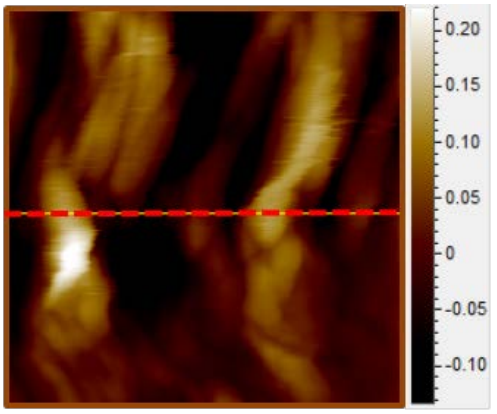

(b)

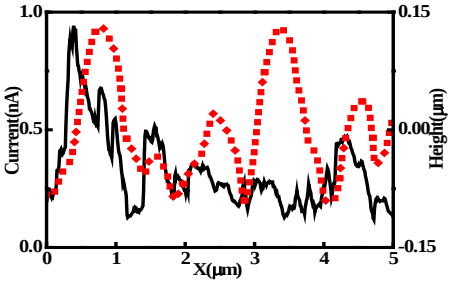

(c)

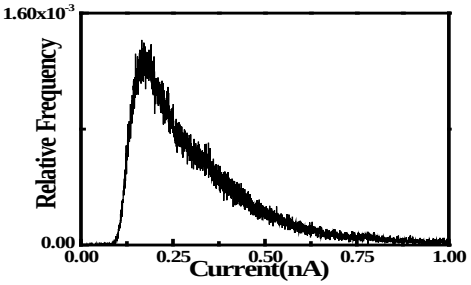

(d)

Figure 90. Nafion® 212 annealed at 110°C for 15 hours

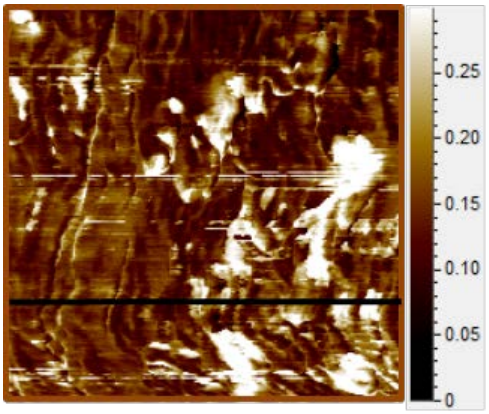

(a)

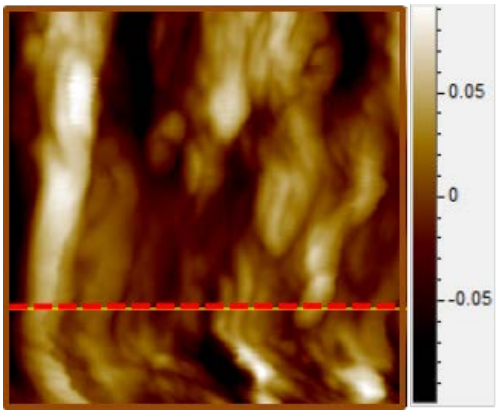

(b)

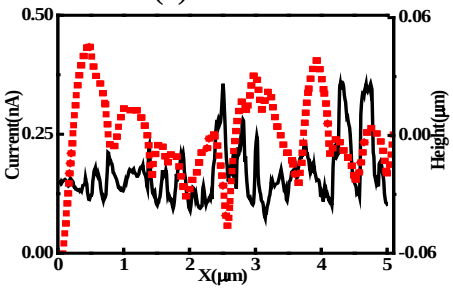

(c)

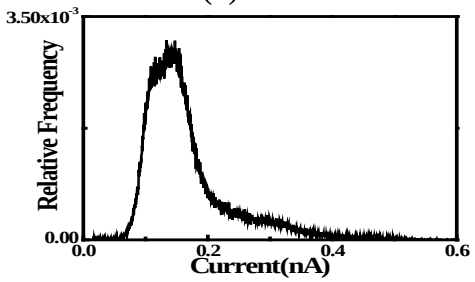

(d)

Figure 91. Nafion® 212 annealed at 110°C for 19 hours

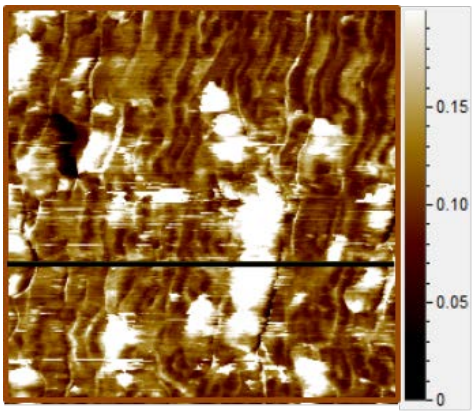

(a)

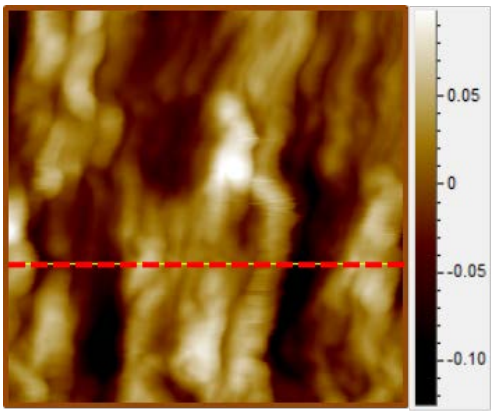

(b)

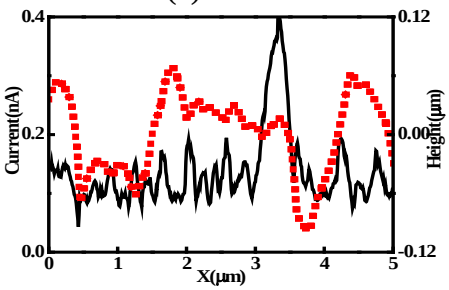

(c)

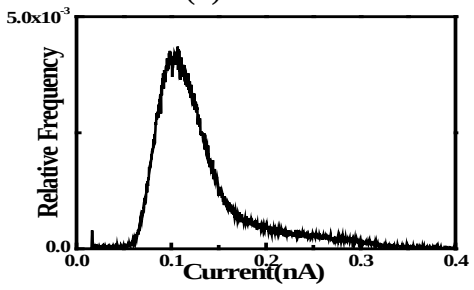

(d)

Figure 92. Nafion® 212 annealed at 110°C for 26 hours

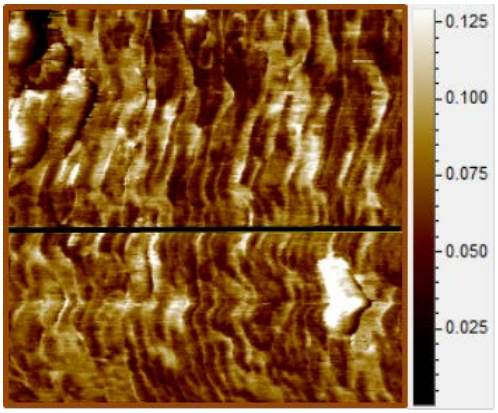

(a)

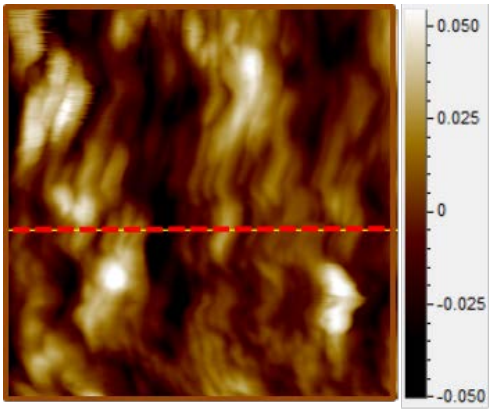

(b)

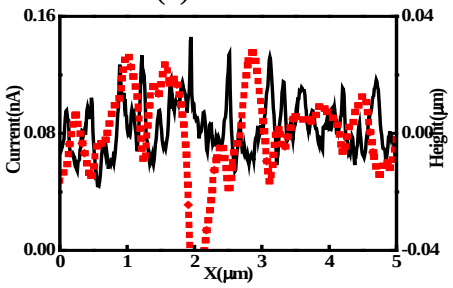

(c)

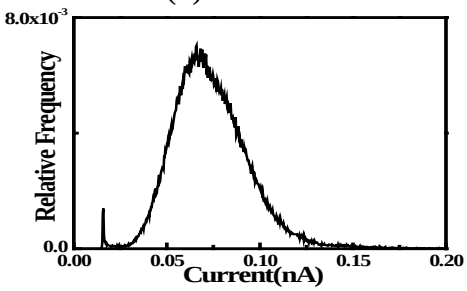

(d)

Figure 93. Nafion® 212 annealed at 110°C for 34 hours

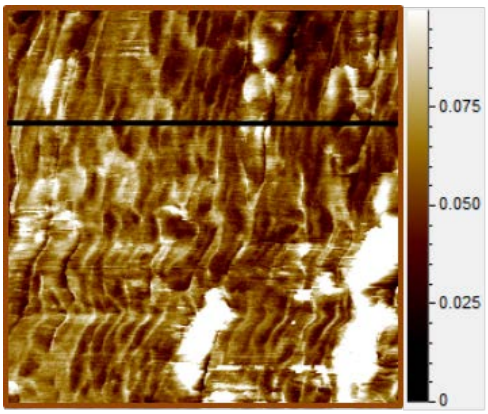

(a)

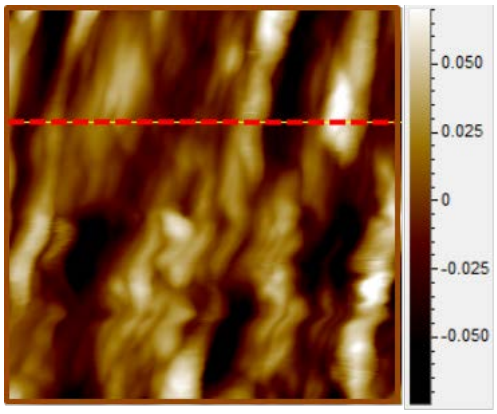

(b)

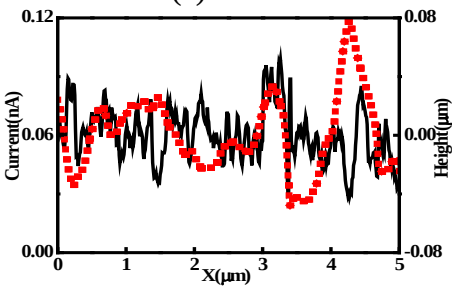

(c)

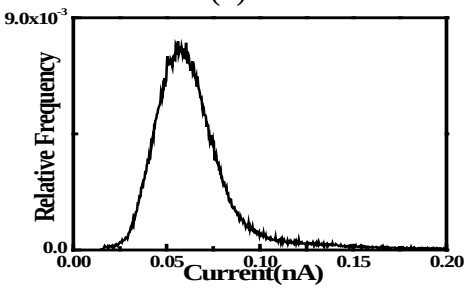

(d)

Figure 94. Nafion® 212 annealed at 110°C for 38 hours

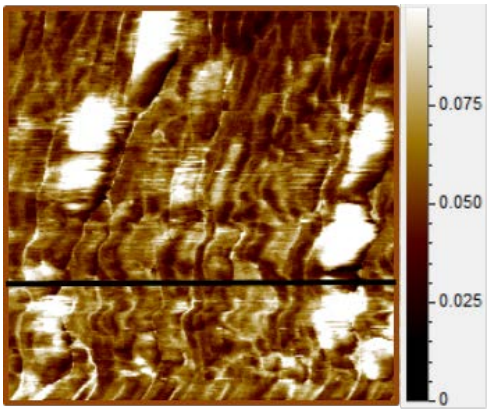

(a)

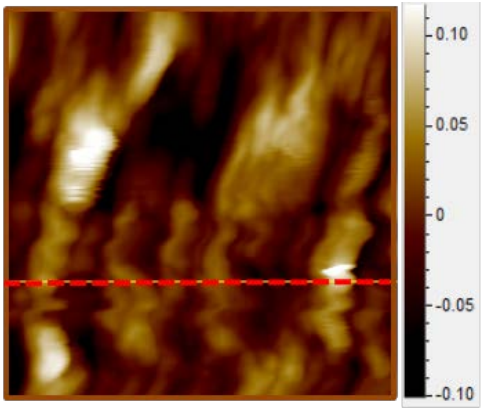

(b)

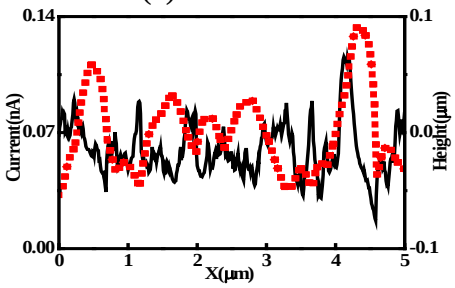

(c)

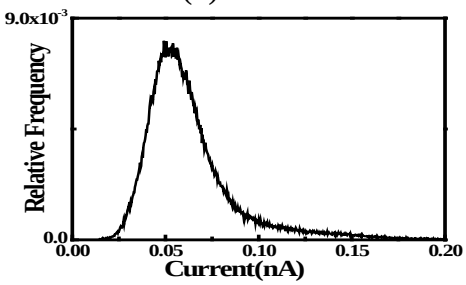

(d)

Figure 95. Nafion® 212 annealed at 110°C for 50 hours

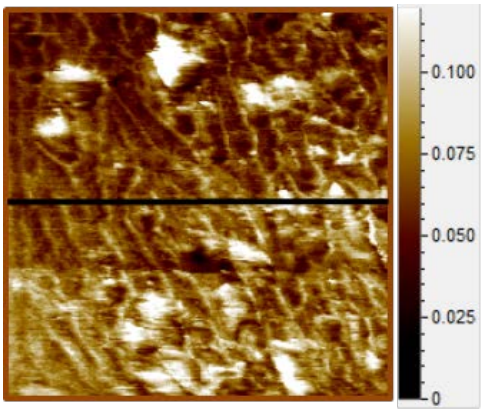

(a)

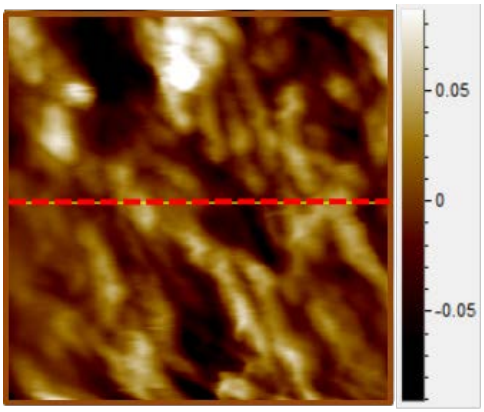

(b)

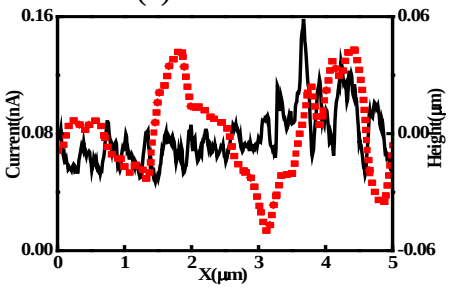

(c)

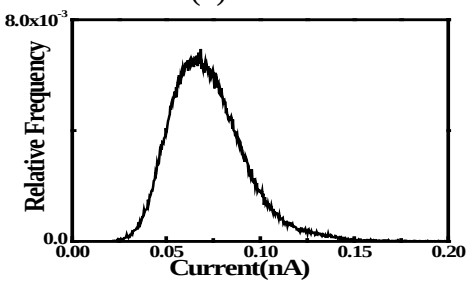

(d)

Figure 96. Nafion® 212 annealed at 110°C for 50 hours

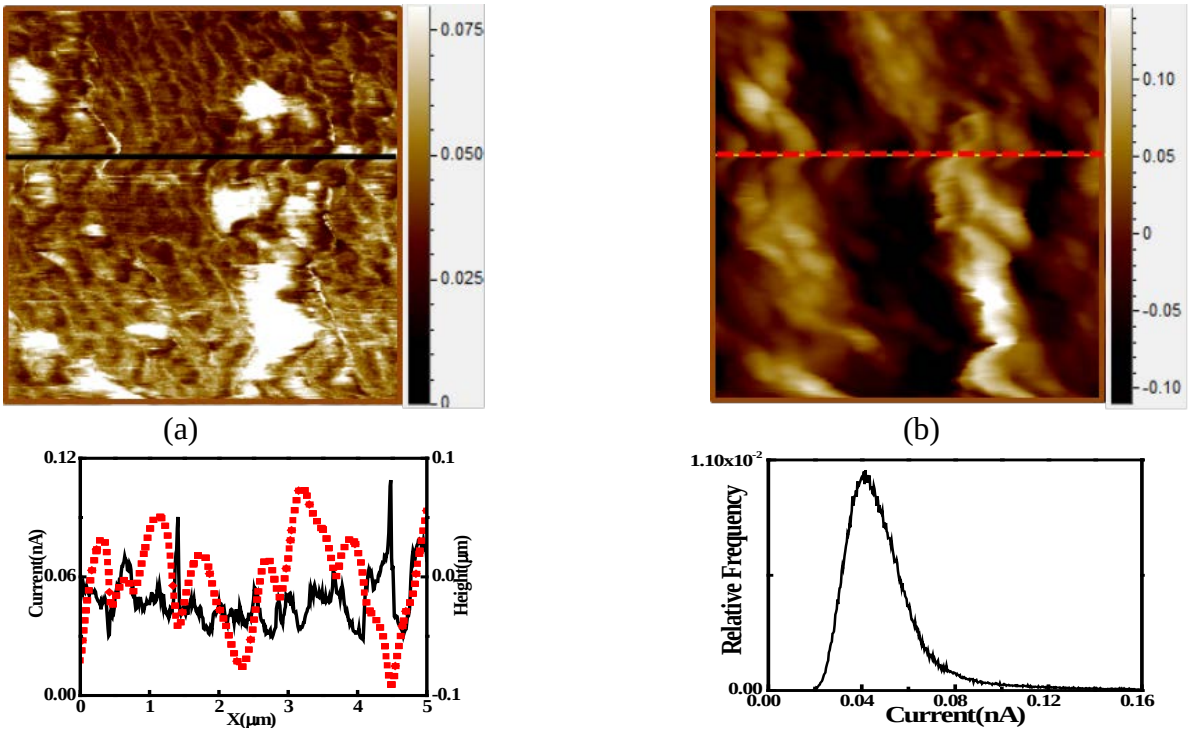

Figure 97. Nafion® 212 annealed at 110°C for 54 hours

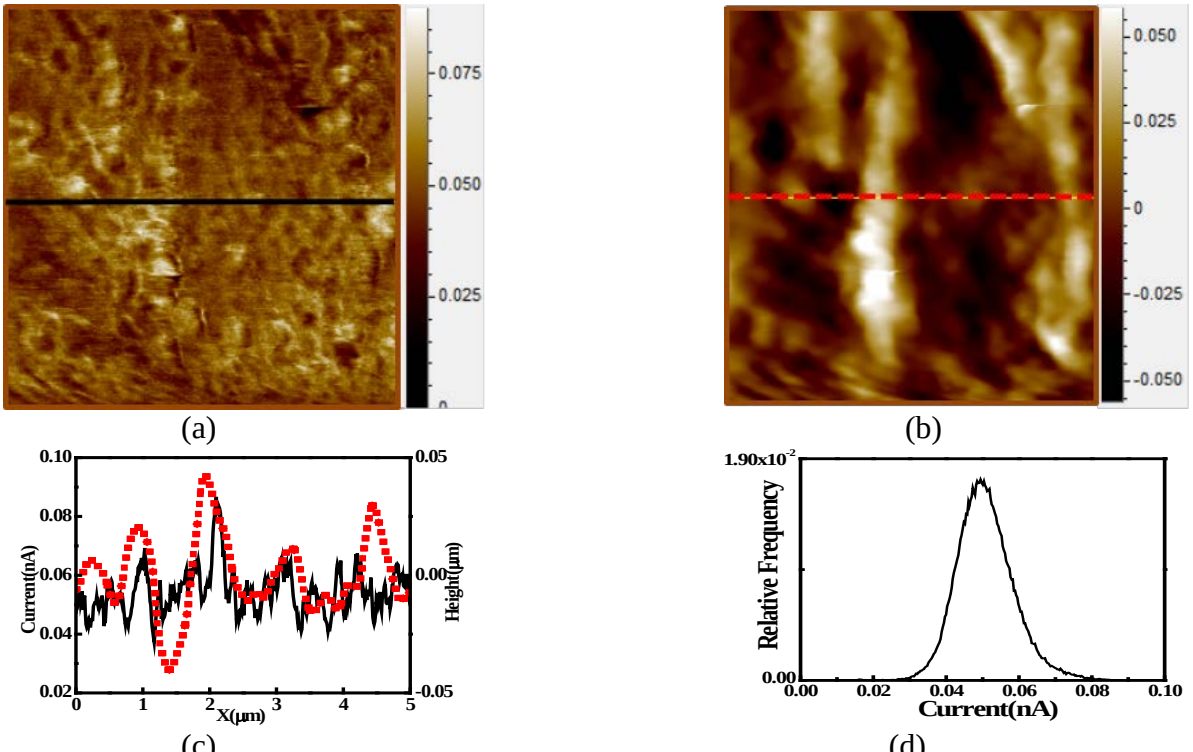

Figure 98. Nafion® 212 annealed at 110°C for 59 hours

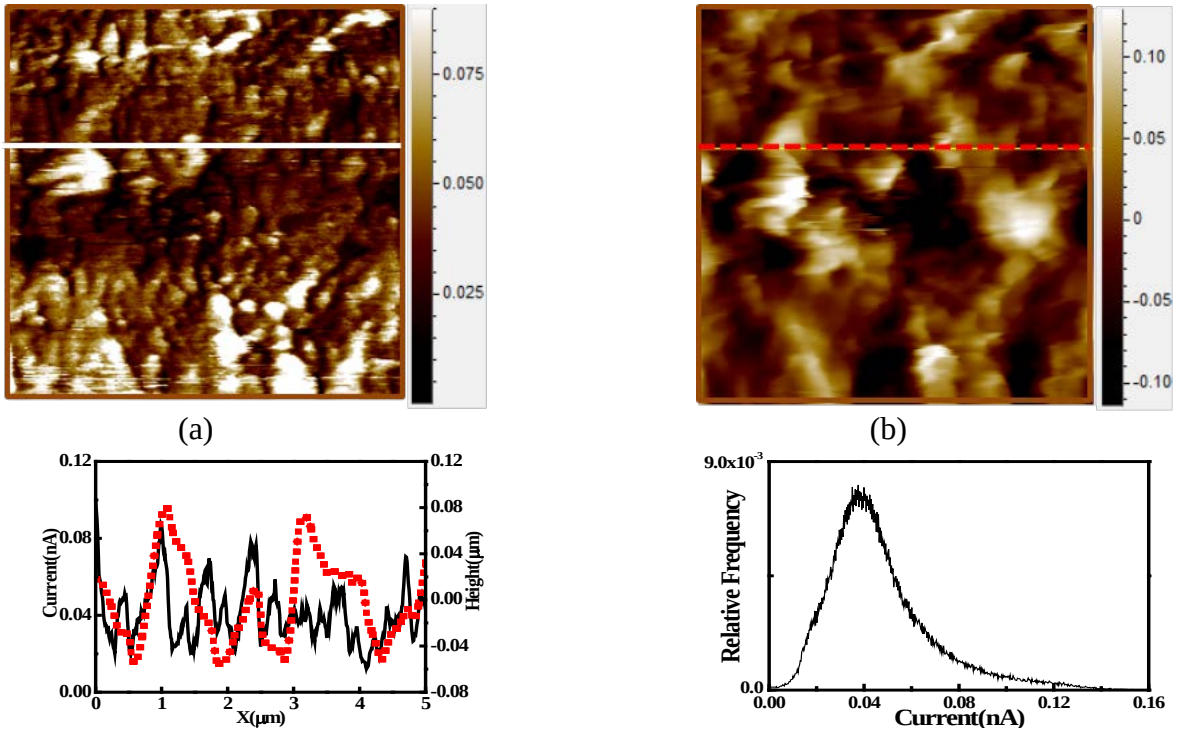

Figure 99. Nafion® 212, Pristine

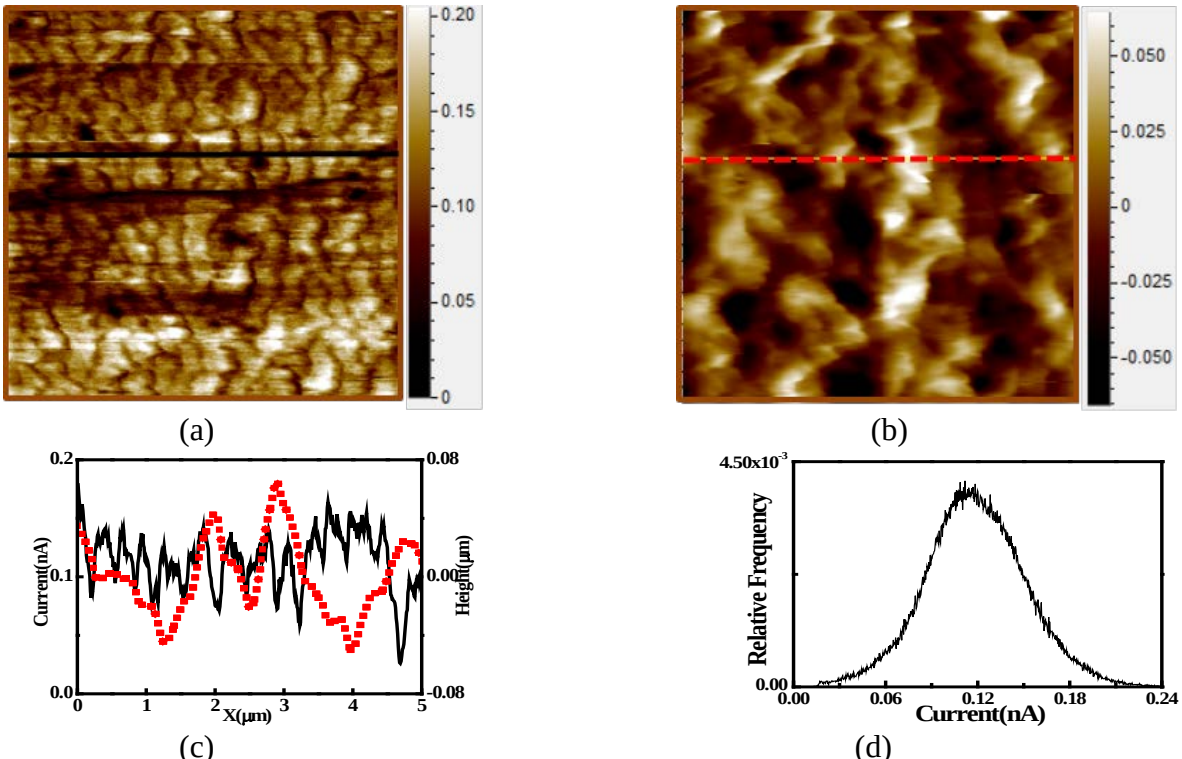

Figure 100. Nafion® 212 annealed at 120°C for 3 hours

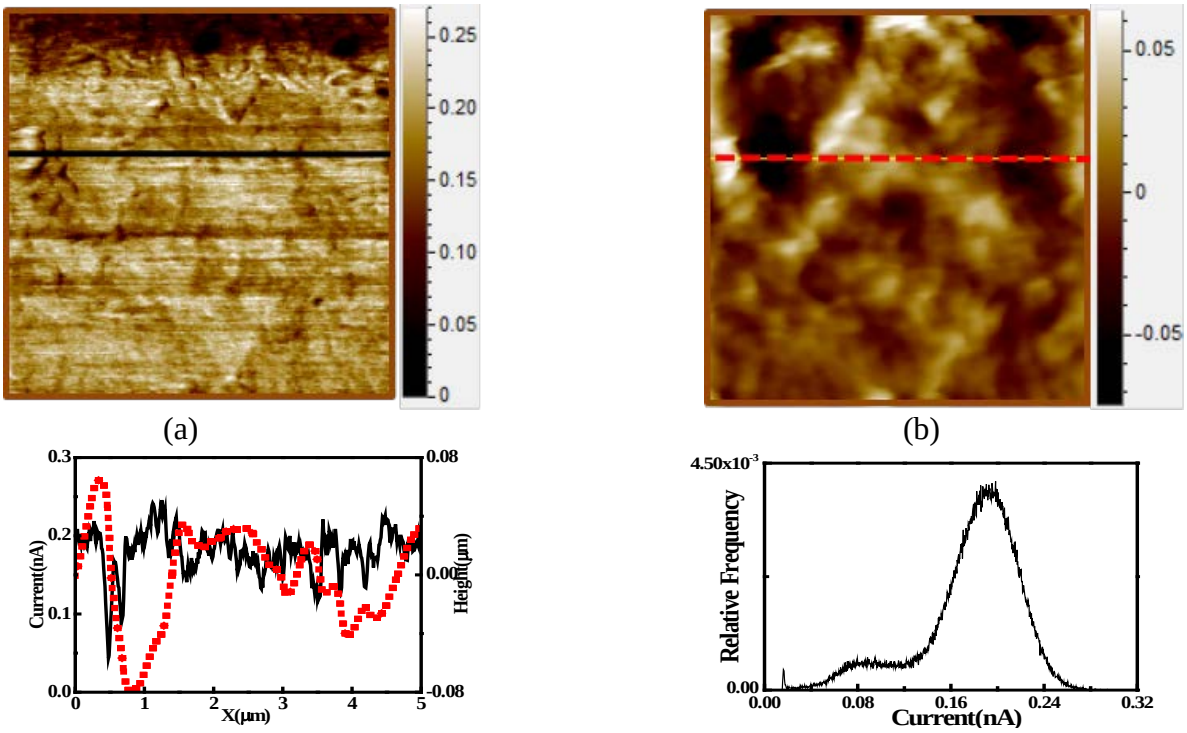

Figure 101. Nafion® 212 annealed at 120°C for 6 hours

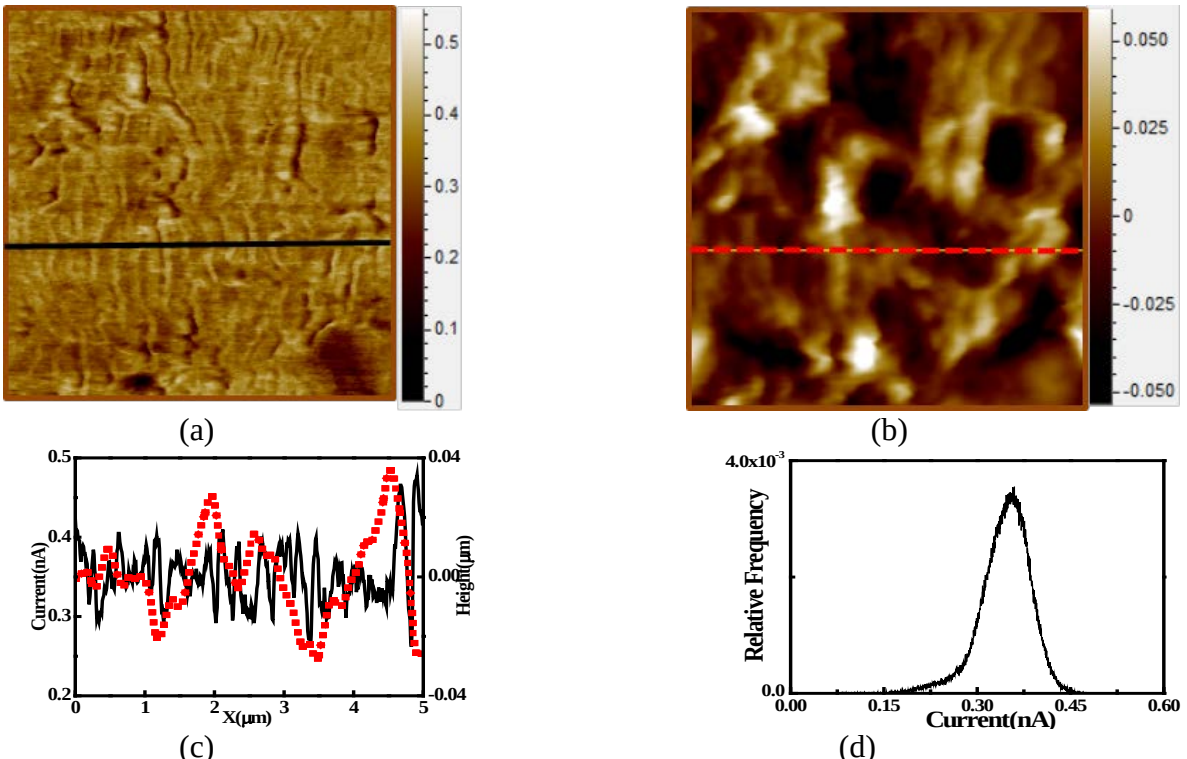

Figure 102. Nafion® 212 annealed at 120°C for 12 hours

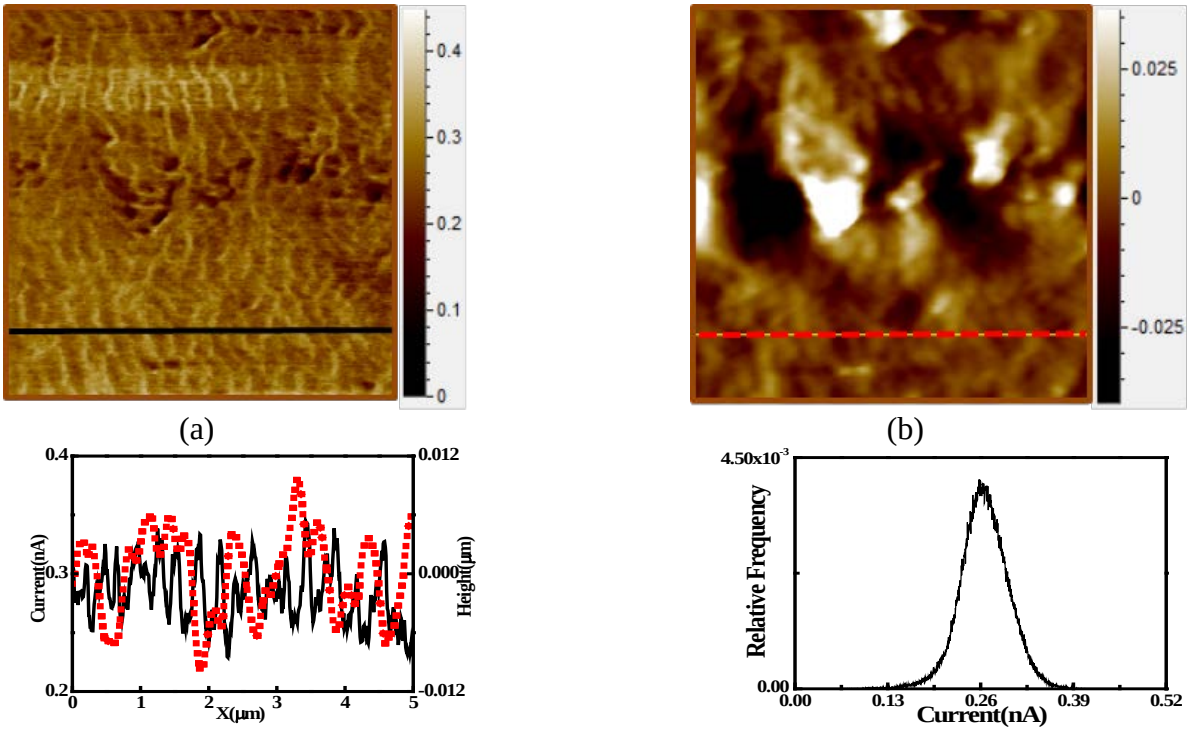

Figure 103. Nafion® 212 annealed at 120°C for 15 hours

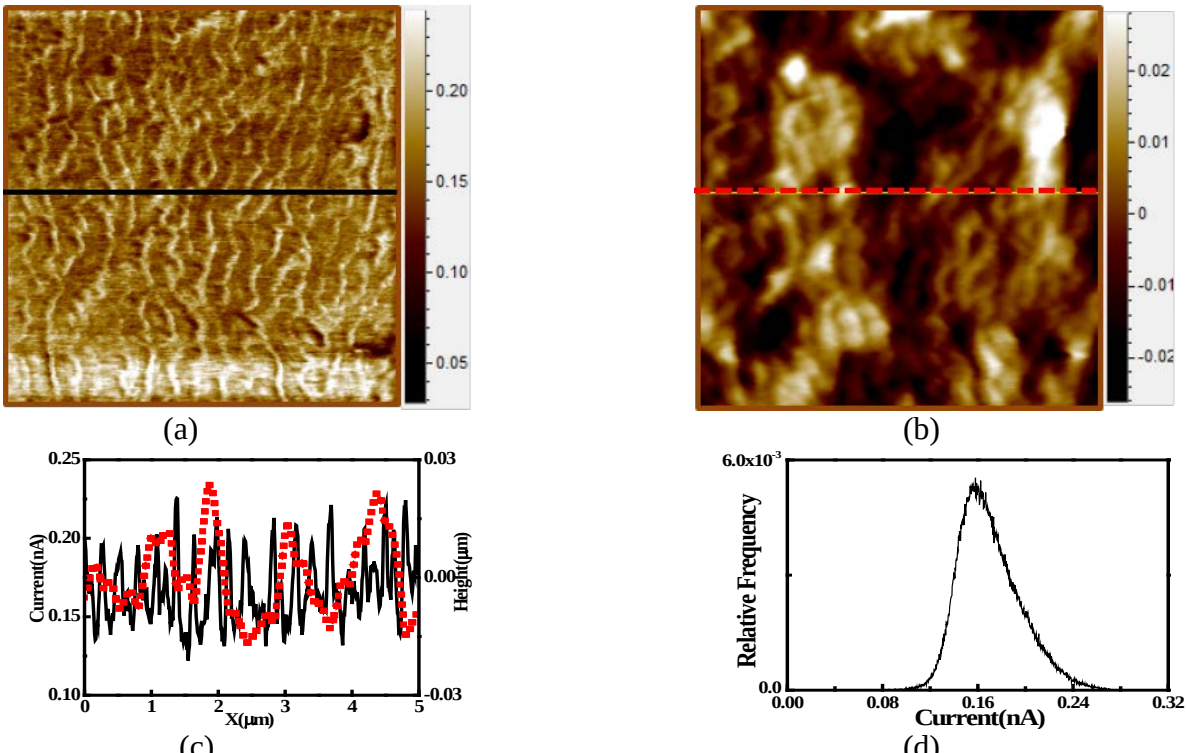

Figure 104. Nafion® 212 annealed at 120°C for 18 hours

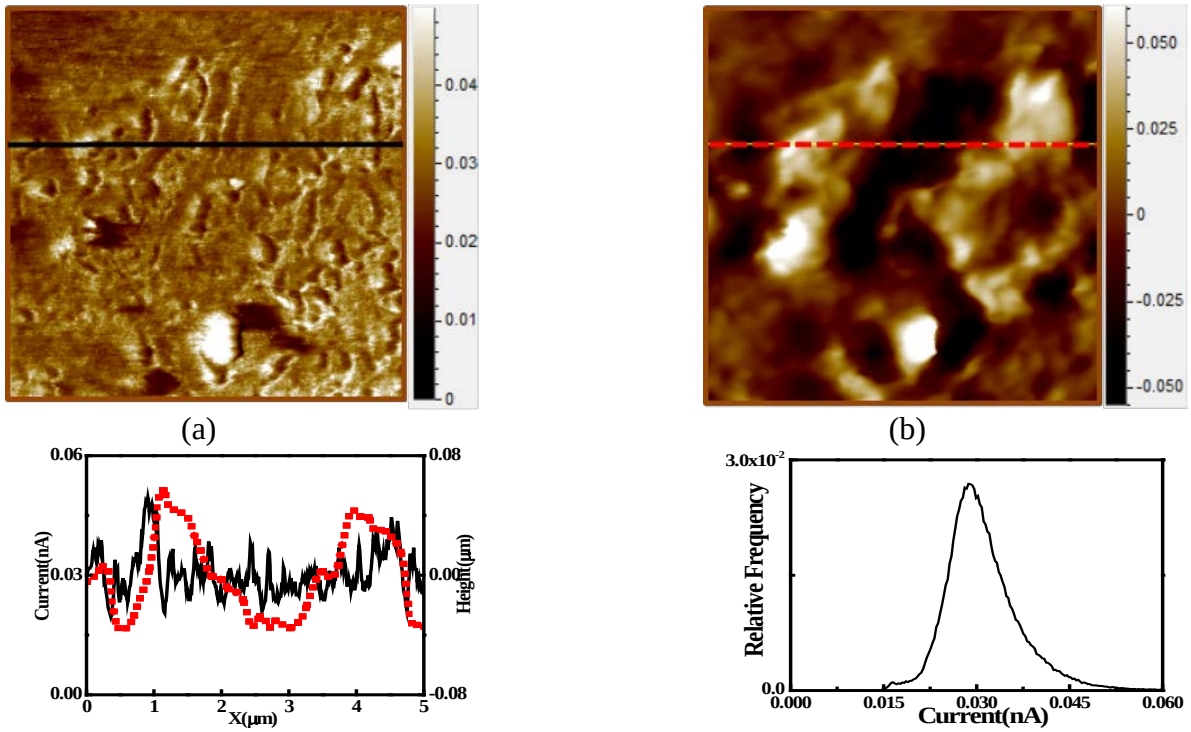

Figure 105. Nafion® 212 annealed at 120°C for 27 hours

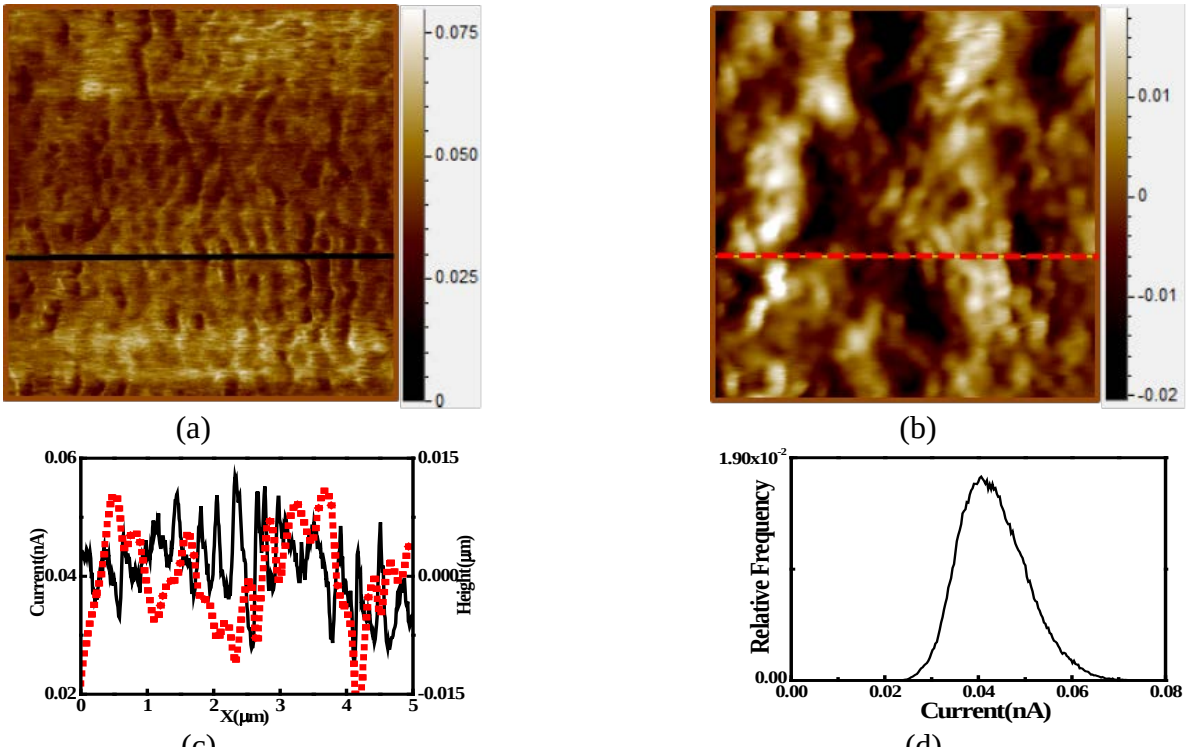

Figure 106. Nafion® 212 annealed at 120°C for 30 hours

Figure 109 to 114 were calculated from the conductance distribution of each image. When the proton current from the single ionic channel on the membrane surface to the opposite electrode is σ and the average number of the contacting clusters with the tip is λ, the peak value C_{peak} and full width at half maximum (FWHM) ΔC can be calculated from a Gaussian distribution. The peak value C_{peak} is the average number multiplied by the current at single cluster and ΔC is FWHM of the normal distribution multiplied by single current from the conductance distribution as shown in equation 3 and 4.

$$C_{peak} = \lambda\sigma \tag{3}$$

$$\Delta C = 2\sqrt{2\ln 2\lambda}\sigma \tag{4}$$

Then the current at the single channel and average number of the clusters in contact with the tip are

$$\sigma = \frac{(\Delta C)^2}{8\ln 2} \tag{5}$$

$$\lambda = \frac{8\ln 2 C_{peak}}{(\Delta C)^2} \tag{6}$$

Figures 107 and 108 plot the peak value variation of each annealing temperature from the Nafion® 115 and Nafion® 212. All plots show the same tendency, initially the peak value, which refers to the mean conductance, increased to the maximum value. Then, the maximum value started to decay and reached to zero. The increment time of the peak value is roughly 10 hours for all annealing temperatures for both membranes. This phenomenon is reported in many studies [88, 89]. Hensley et al. reported the effect of thermal annealing of the Nafion membranes by the X-ray scattering study [88]. He annealed commercial Nafion membranes

for 3 hours. When the Nafion 115 membrane was annealed at 90^{o}C, conductivity of the membrane was increased by about 20%. The conductivity increment is due to enhancement of water permeability, proton conductivity, and equilibrium water sorption increase. However, he could not explain the conductivity increment related to the morphological (ionic channel network) variation, which is crucial for understanding membrane aging. My understanding of the conductivity increment of the membrane is related to the ionic channel network reorganization near the membrane surface. When the membranes are annealed, the ionic channel networks, which are the randomly distributed in the membrane start to diffuse and reorganize to parallel to the membrane. The connectivity of the each ionic channel network should be increased, so that water and protons may easily pass through the network. The increasing of permeability of protons into membrane induces the conductance increasing of the membrane.

After the peak value reaches the maximum, the peak value starts to decay and goes to zero. The decay rate depends on the annealing temperature. The decay time is 130 hours at 90^{o}C, 80 hours at 100^{o}C, 50 hours at 110^{o}C, and 30 hours at 120^{o}C for Nafion 115 membrane. Nafion 212 membranes also show similar decay time except for 90^{o}C and 100^{o}C. At 90^{o}C and 100^{o}C annealing temperature, decay time of the Nafion 212 membranes are longer than the Nafion® 115. This should be related to EW differences of the two membranes as previously mentioned. The peak value decay might be due to the morphological change of ionic clusters in the membrane surface. The proton permeability, which is related proton conductivity, is reduced while the morphology of ionic clusters changes.

Figures 109 and 110 are full width at half maximum (FWHM) for Nafion 115 and Nafion 212 membranes. When the difference of each pixel on the current sensing image is

relatively large, the FWHM of conductance distribution is relatively large. Similarly the difference of pixels is relatively small because FWHM is affected by deviation of the current at each pixel. Thus, FWHM on the membranes represents conductance roughness of the membrane. If the conductance discrepancy of each pixel is large which represent a wide FWHM, than the conductance defines the rough state; otherwise it is a smooth state. All of the graphs from Nafion 115 and Nafion 212 membranes show the same variation. The FWHM, conductance roughness, increases for 10 hours and then it continuously decreases to zero. All membranes show the similar conductance roughness increasing rate while the membrane is annealing. However, the decreasing rate of conductance roughness depends on the annealing time. By increasing annealing time10^{o}C, the decreasing rate is 20 hours shorter. The increasing of roughness can be explained by reorganization of the ionic clusters. During the ionic channel network reorganization, the ionic channels form an inter-connection in the membrane. Different numbers of inter-connection should be formed for each ionic cluster. The variety of inter-connection of the ionic channel should be possible by thermal annealing. One possibility is that the ionic channel near the membrane is connected to many other ionic channels inside of the membrane and branches out to the end of the membrane. In this case, the probability of the proton passing through the network will be high and then the measured conductance of that point (pixel) is higher than any other pixels. Another possibility is that the ionic channel near the membrane is connected to only a few channels. Then low conductance will be recorded at the pixel because the probability of the proton passing through the network is relatively small. Another possibility is that the ionic channel is connected to other ionic channels but the connection is only inside the membrane. In this case, the proton conductance becomes zero. In the early stage (from 0 hours to 10 hours) of

annealing, the ionic channel inter-connection should be increased. The increasing of the conductance roughness is due to coexistence of the many connection possibilities of ionic channels.

There are two possible explanations about decreasing of the conductance roughness on the membrane. The first explanation is that the numbers of ionic clusters in contact with tip become smaller due to thermal annealing. By decreasing the number of the ionic clusters in contact with the tip, the discrepancy of conductance between each pixel becomes smaller and smaller. Eventually, the discrepancy of conductance between each pixel becomes zero and the conductance on the membrane becomes perfectly smooth. When the thermal energy is increased, the clusters decomposition is increased and the decreasing rate of roughness becomes smaller by increasing the annealing temperatures.

The second explanation is that the permeability of proton in the single channel can vary. The permeability of protons determines the conductance of the single channel. The permeability change influences the conductance variation of each pixel. This permeability variation might be explained by the changing geometry of a single ionic cluster. So, continuous deformation of the ionic cluster induces reduction of permeability. Due to the permeability reduction, the difference of each pixel becomes smaller. The continuous reduction of permeability in the single channel induces the continuous conductance decreasing in difference of each pixel. Both hypotheses explain the conductance roughness decreasing mechanism well by thermal annealing.

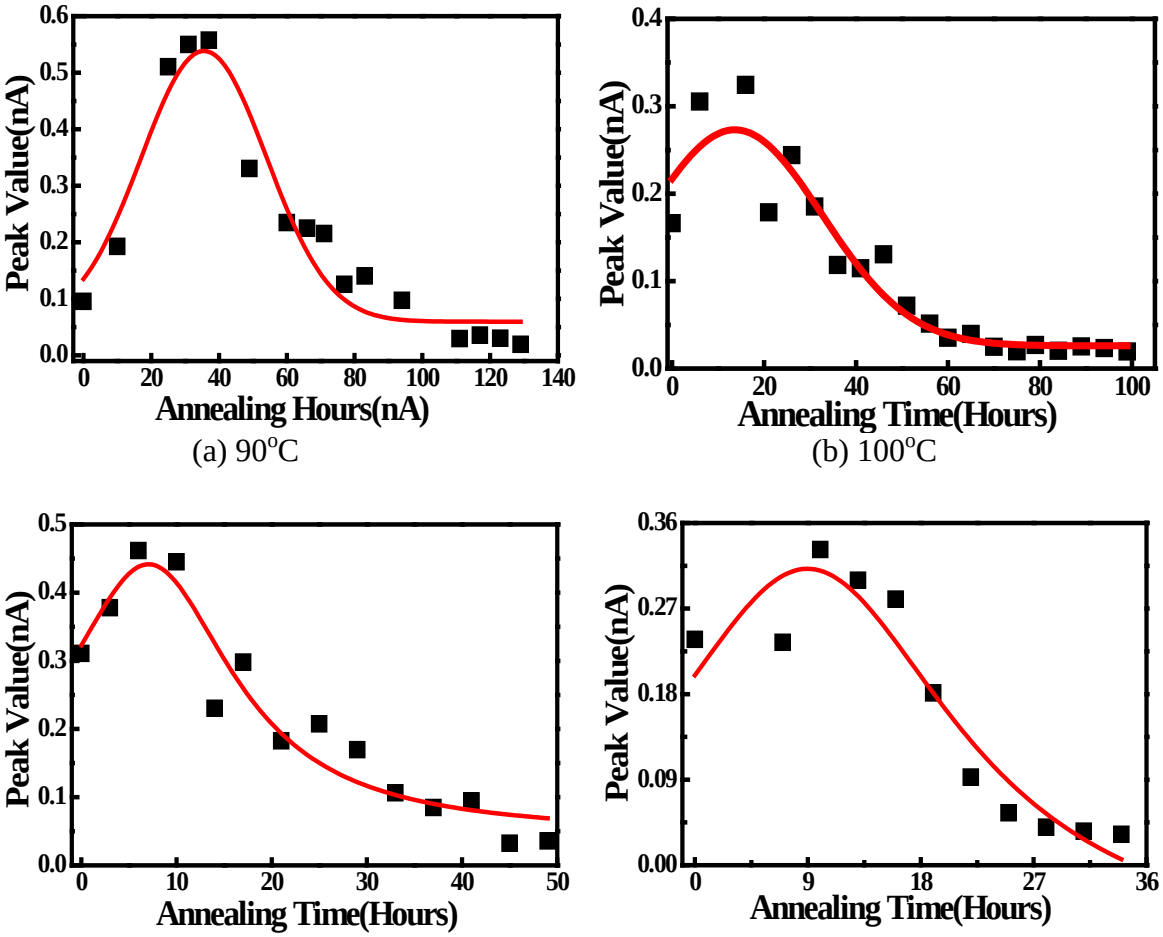

(a) 90°C (b) 100°C

(c) 110°C (d) 120°C

Figure 107. Peak Value of Nafion® 115 at each annealing time

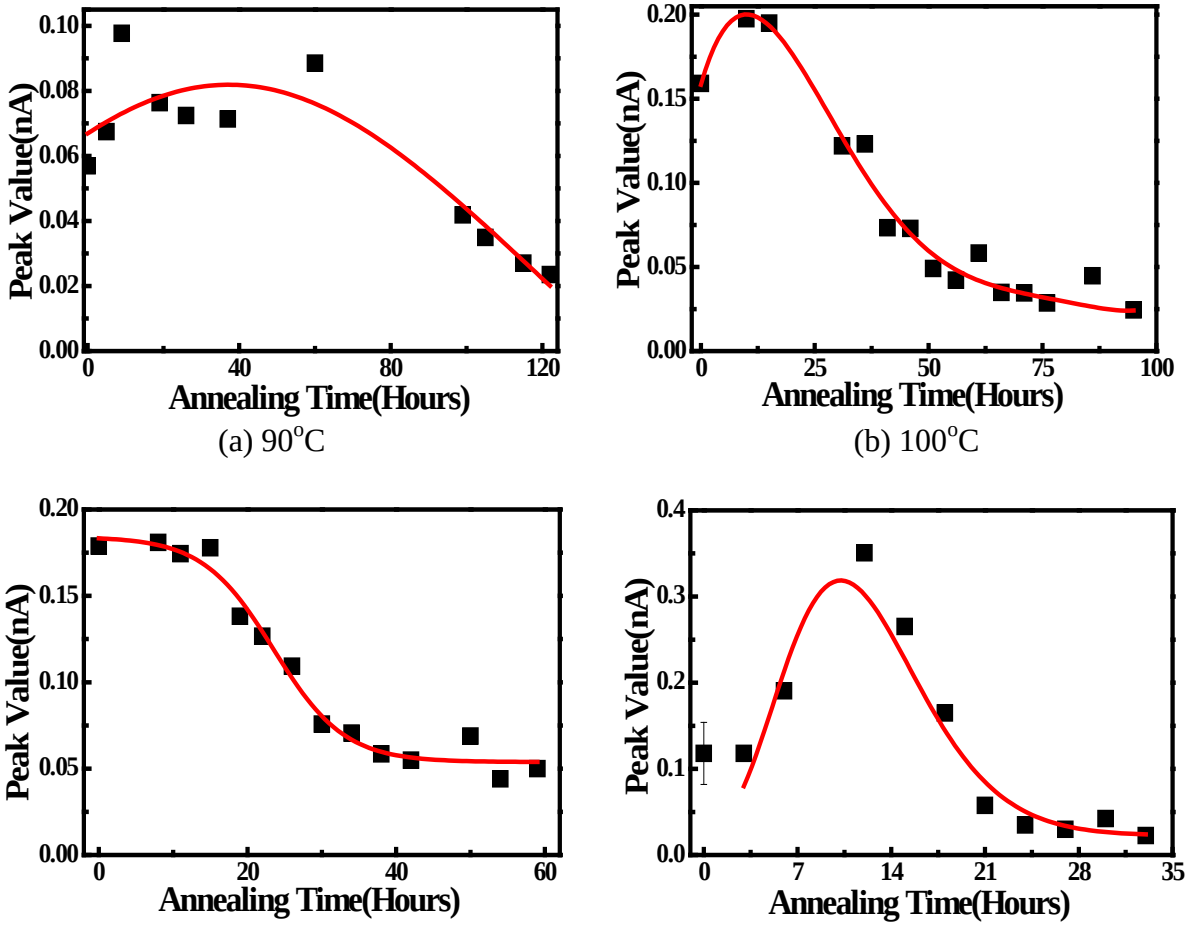

(a) 90°C (b) 100°C

(c) 110°C (d) 120°C

Figure 108. Peak value of Nafion® 212 at each annealing time

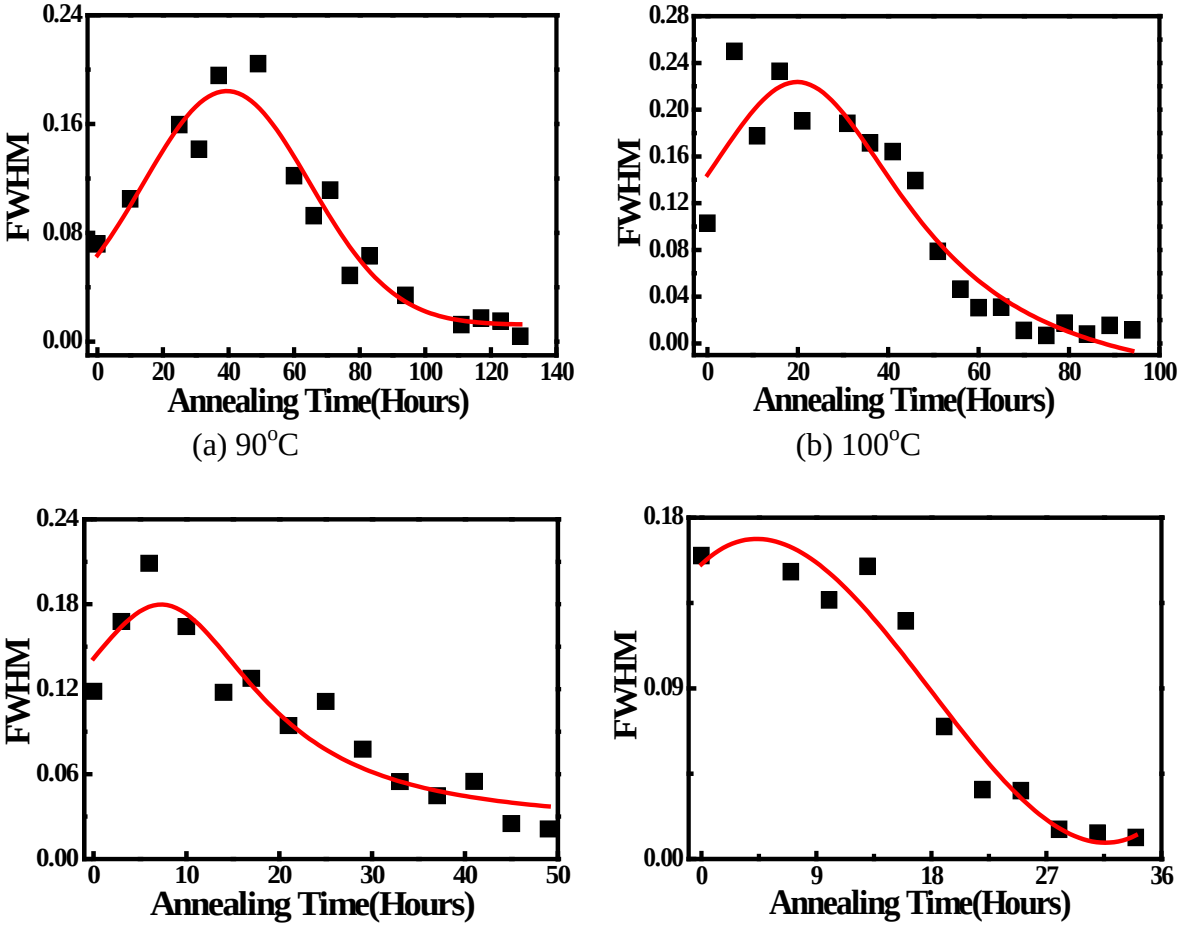

(a) 90°C (b) 100°C

(c) 110°C (d) 120°C

Figure 109. Full width at half maximum of the Nafion® 115 at each annealing time

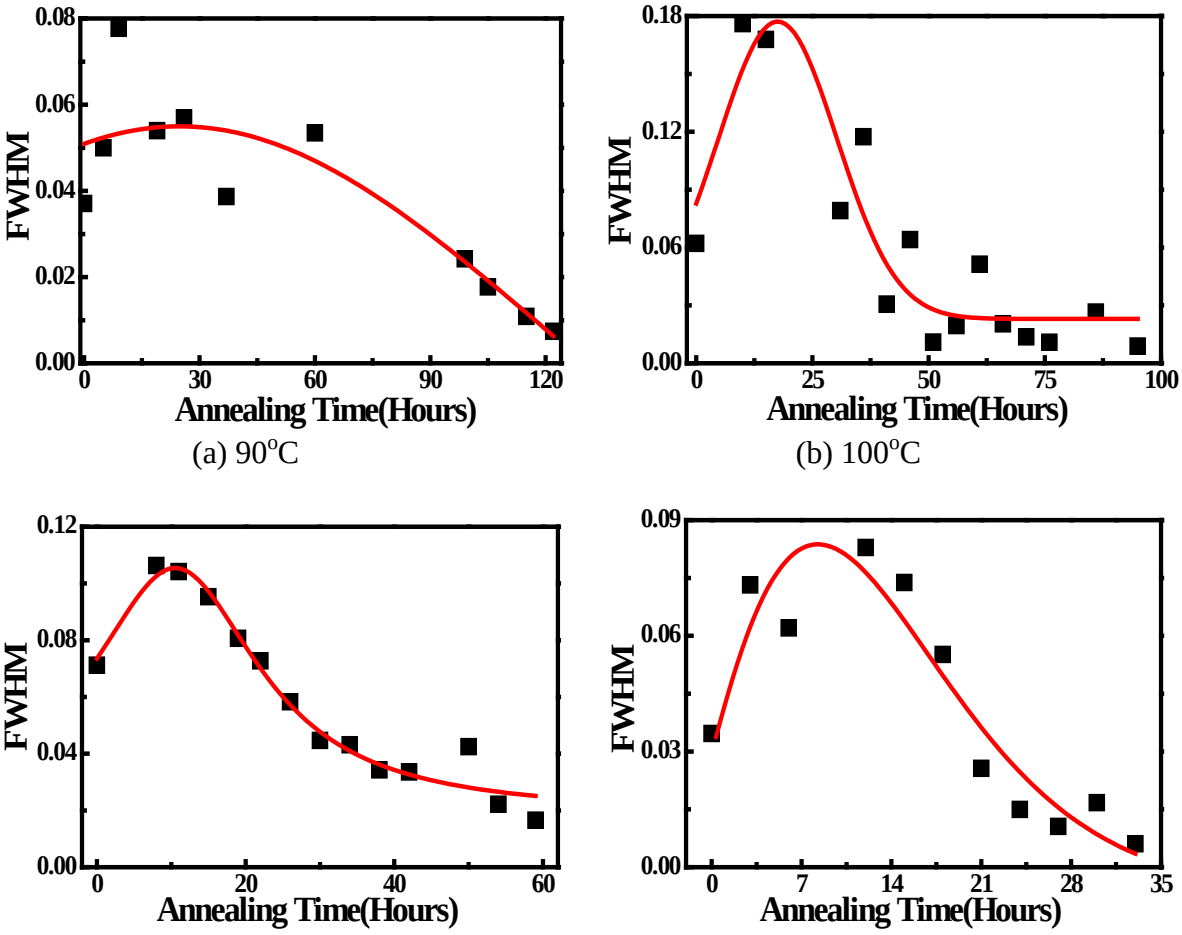

(a) 90°C (b) 100°C

(c) 110°C (d) 120°C

Figure 110. Full width at half maximum of the Nafion® 212 at each annealing time

Figure 111 and 112 plot current variation in a single channel by each annealing temperatures of Nafion® 115 and Nafion® 212. The current in a single channel is calculated from equation 5 using the peak value and FWHM in the conductance distribution. If protonw easily pass through ionic cluster channels, the current in a single channel will be high, otherwise it will be low. So, the current in a single channel is directly related to proton permeability and the figures 111 and 112 represent the proton permeability variation of the membrane. All plots of the Nafion 115 and Nafion 212 membranes display the same variation tendency. When the annealing of the membrane is started, the current in a single channel also starts increasing. After 10 hours annealing time, the current in a single channel reaches maximum value. After it reaches a maximum value, it gradually decreases. The decay rate of the membranes depends on the annealing temperatures. Decay rate difference of each annealing temperature is about 20 hours. The variation of the current in a single channel reflects that proton permeability initially increases and then gradually decreases. The increasing of the current in a single channel can be explained by the reorganization of the ionic channels. When the membrane is annealed, the mobility of ionic channels increases and organizes into stable state. While the ionic channels are organized, the connectivity of each channel is enhanced. Due to the enhancement of the connectivity, the proton easily passes through the channels. Thus, the proton permeability is increased and the current in a single channel is increased. Proton permeability is directly related to the geometry of the ionic cluster. So, the current change in a single channel can be due to the geometrical change of the ionic clusters. The structure of the ionic cluster is inverted micelles which include sulfonic

acid groups. If sulfonic acid groups are decomposed by the thermal annealing, the geometry of the ionic clusters is deformed and the proton permeability is reduced by this ionic cluster deformation. Thus, the current in a single channel is decreased. This hypothesis explains the decay of the current in a single channel well; however, there is another possible explanation. The current in a single channel was calculated using the peak value, mean current on the membrane. If the number of the ionic clusters in contact with the tip is reduced, then the mean current on the membrane is decreased. Because of the decreasing mean current, the current in a single channel is also decreased. Figure 111 and 112 show that the membrane aging is clearly related to the variation of the ionic cluster but the specific ionic cluster variation mechanism is unclear.

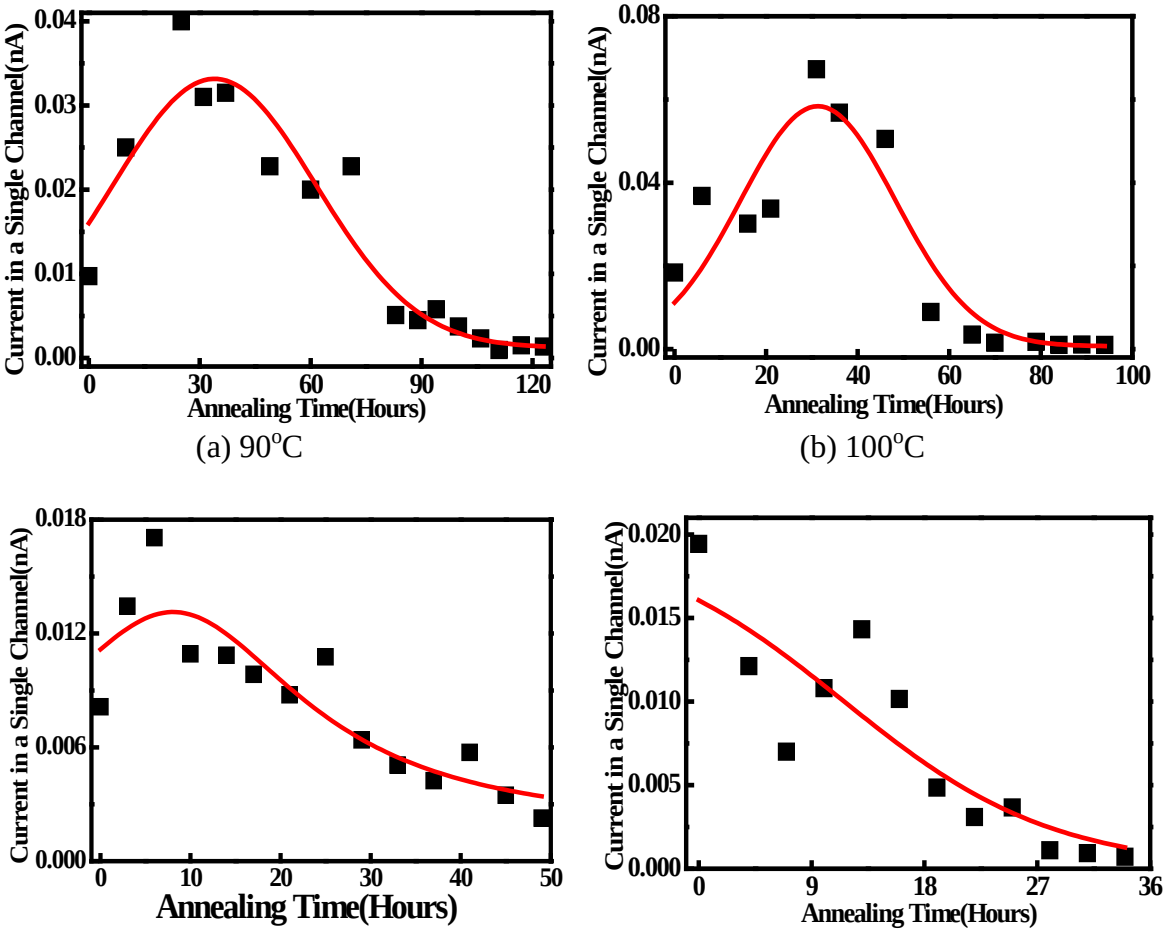

(a) 90°C (b) 100°C

(c) 110°C (d) 120°C

Figure 111. Current at single channel of the Nafion® 115 at each annealing time

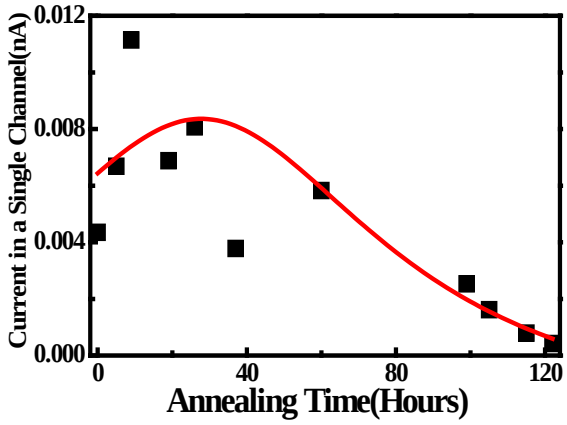

(a) 90°C

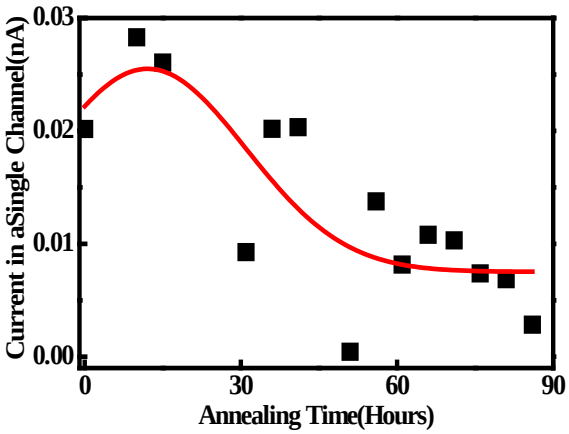

(b) 100°C

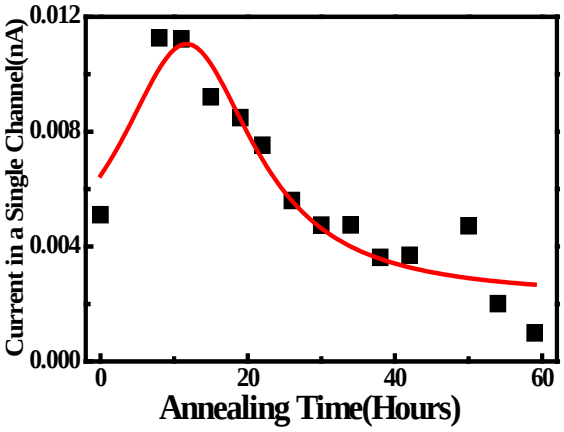

(c) 110°C

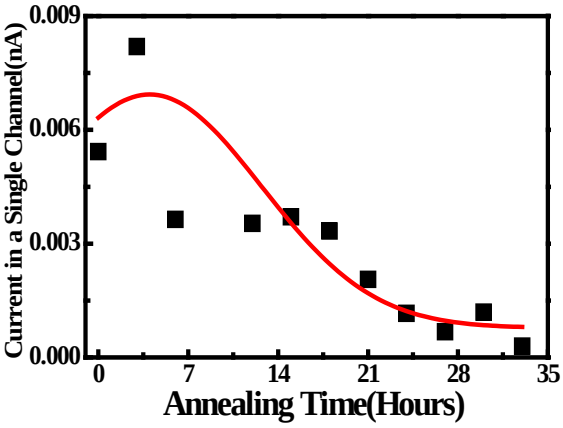

(d) 120°C

Figure 112. Current at single channel of Nafion® 212 at each annealing time

Figures 113 and 114 plot the average number of clusters in contact with the tip at each annealing temperature. Each point in the plot was calculated using equation 5. In the Nafion 115 membrane, the average number of clusters in contact with the tip is roughly 20 at 90^{o}C to 110^{o}C. At 120^{o}C, the number of clusters in contact with the tip is about 30 for the Nafion 115 membrane. In the Nafion 212 membrane, the average number of clusters in contact with the tip is 15 from 90^{o}C to 110^{o}C and 30 at 120^{o}C. Another point, both greater and less than 20, was affected by the tip deformation. The tips used in this study were coated by a soft Pt layer. This Pt layer can easily deform; it should be ground away from the tip due to the friction between the tip and membrane. Also, something could be adhered to the tip. The result which is the constant average number of clusters in contact with the tip during the annealing process represents the overall ionic clusters in the membrane which are always constant. It is very important to understand the aging mechanism of the membrane because it indicates that there is no number of ionic clusters change on the membrane and the deformation of individual ionic cluster induces the aging of the membrane.

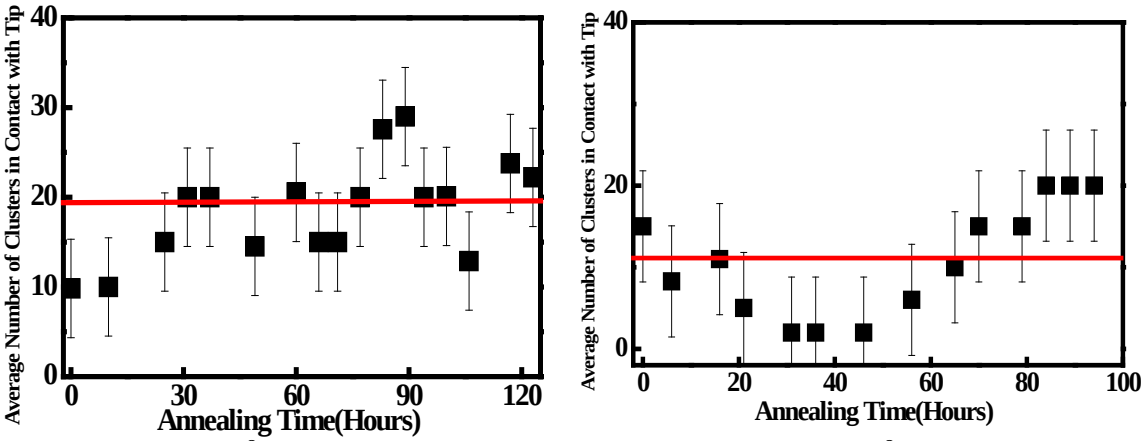

(a) 90°C

(b) 100°C

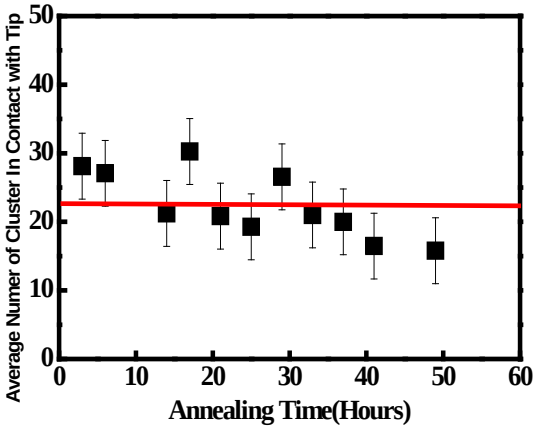

(c) 110°C

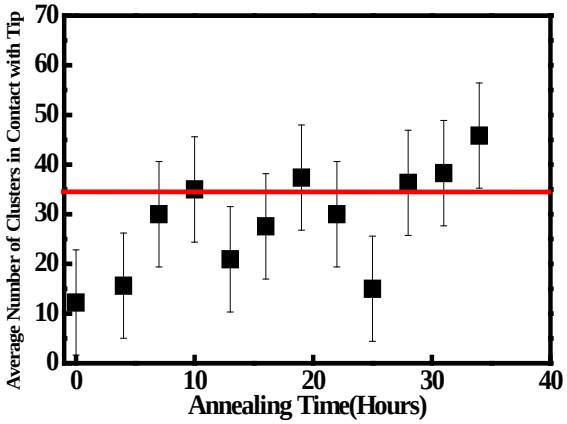

(d) 120°C

Figure 113. Average number of clusters in contact with tip at each annealing time in Nafion® 115

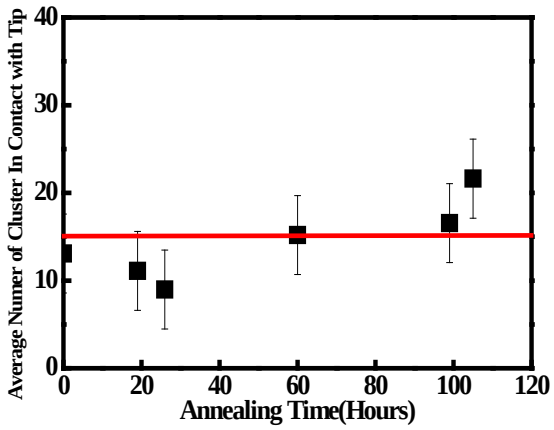

(a) 90°C

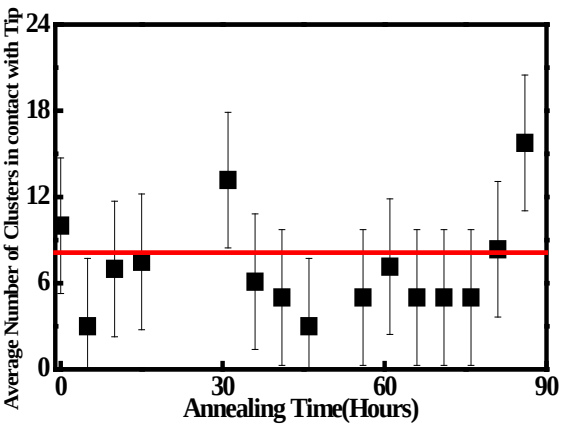

(b) 100°C

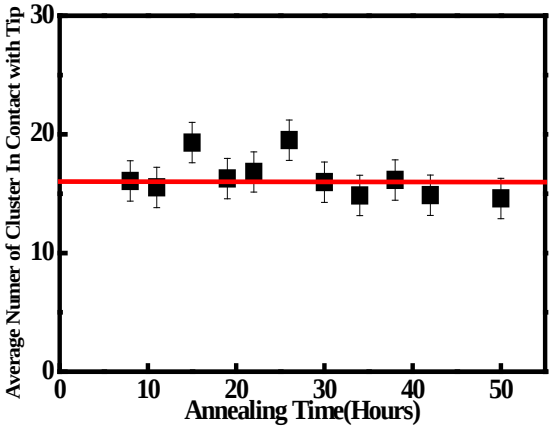

(c) 110°C

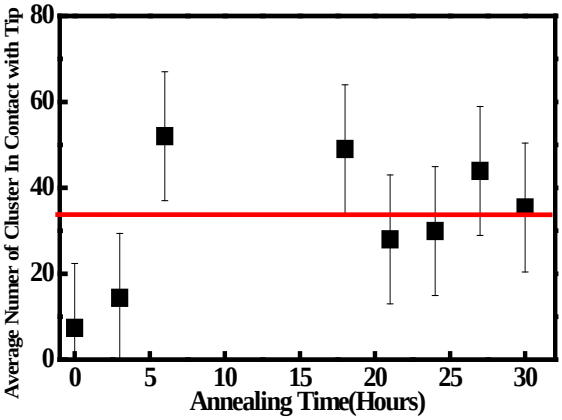

(d) 120°C

Figure 114. Average number of clusters in contact with tip at each annealing time in Nafion® 212

Table 2 is a summarization of the peak value decaying of the Nafion 115 and Nafion 212 membrane. Two membranes show different decay times. The decay time difference of both membranes is 30 hours, 20 hours, 10 hours, and 0 hours relative to 90 ^{o}C, 100 ^{o}C, 110 ^{o}C, and 120^{o}C annealing temperatures. The decay time difference might be related to the equivalent weight (EW) difference of the membranes. Nafion 212 membrane has a larger EW then Nafion 115 because EW is 1100 at Nafion 115 and 2100 at Nafion 212. EW difference of both membranes induces numbers of ionic cluster difference in the Nafion 115 and Nafion 212 membranes. If we assume the decay is related to structural change of the ionic clusters, the membrane which has a larger ionic cluster must have a longer decay time. So, the relatively longer decay time of the Nafion 212 membrane can be explained by larger EW. Table 3 shows that the decay time difference becomes shorter due to annealing temperature. It should be related to the mobility of the sulfonic acid group in the ionic cluster. At low temperatures, the mobility is relatively small so the EW effect is dominant in the membrane. However, EW effect in the membrane becomes smaller and the mobility effect becomes dominant at higher temperatures. Thus, the decay time difference is shorter by increasing of annealing temperatures.

Table 3 is a comparison of the ionic cluster radius between the water channel model and my study. The ionic cluster radius was calculated from the effective contact area between the tip and membrane divided by the average number of the ionic clusters in contact with the tip. From the water channel model, the morphology of the ionic clusters is expressed by the randomly close-packed inverted micelles. So, the contact area of the tip divided by the average number of clusters in contact with the tip gives the radius of the ionic cluster. The result of my calculation is 1.78 and 2.06 relatively for Nafion 115 and Nafion 212 membrane.

This result agrees with the radius of the ionic cluster (1.8~3.5nm) in the water channel model. The radius difference of the Nafion 115 and Nafion 212 membrane is due to EW difference in the membrane. The Nafion 212 membrane EW is twice as large when compared with the Nafion 115 membrane. The ionic clusters in the Nafion 212 membrane consist of a comparably larger number of the sulfonic acid group. Thus the radius of the ionic cluster in the Nafion 212 membrane is larger than Nafion 115 membrane.

Table 4 shows the radius difference of the ionic cluster at each annealing temperature. From 90^{o}C to 110^{o}C, the radius of the ionic cluster is 1.78 nm and 2.06 nm respectively for the Nafion 115 and 212 membranes. At 120^{o}C, the radius of the ionic cluster is reduced to 1.4 nm for both membranes. The mechanism of the reduction of the radius of the ionic cluster is unclear.

	90°C	**100°C**	**110°C**	**120°C**
Nafion 115	80(Hours)	60(Hours)	40(Hours)	20(Hours)
Nafion 212	110(Hours)	80(Hours)	50(Hours)	20(Hours)
Decay Time Difference	30(Hours)	20(Hours)	10(Hours)	0(Hours)

Table 2. Summarization of the peak value decaying

	Water channel model	Nafion 115	Nafion 212
Cluster radius	1.8~3.5nm	1.78nm	2.06nm

Table 3. Comparison of the ionic cluster radius

	Nafion 115	Nafion 212
90°C -110°C	1.78nm	2.06nm
120°C	1.4nm	1.4nm

Table 4. Radius difference of the ionic cluster at each annealing temperatures

Figure 115 illustrates the conductance and current sensing image variation during the thermal aging of the membrane. The conductance in the membrane shows different variations at maximum value (approximately 10 hours annealing time). The conductance on the membrane is increased from 0 to 10 hours. While the conductance on the membrane is increased, the current sensing image shows drastic change such as the randum structures on the current sensing image changes to the filament structures. During this change, FWHM and the current in a single channel are increased; however, the average number of the ionic clusters in contact with the tip is remains constant. The conductance on the membrane is continuously decreased after 10 hours. While the conductance on the membrane decreases, the current sensing image shows the developed filament structures. FWHM and the current in a single channel gradually decay simultaneously. The average number of the ionic clusters in contact with the tip does not change in this interval.

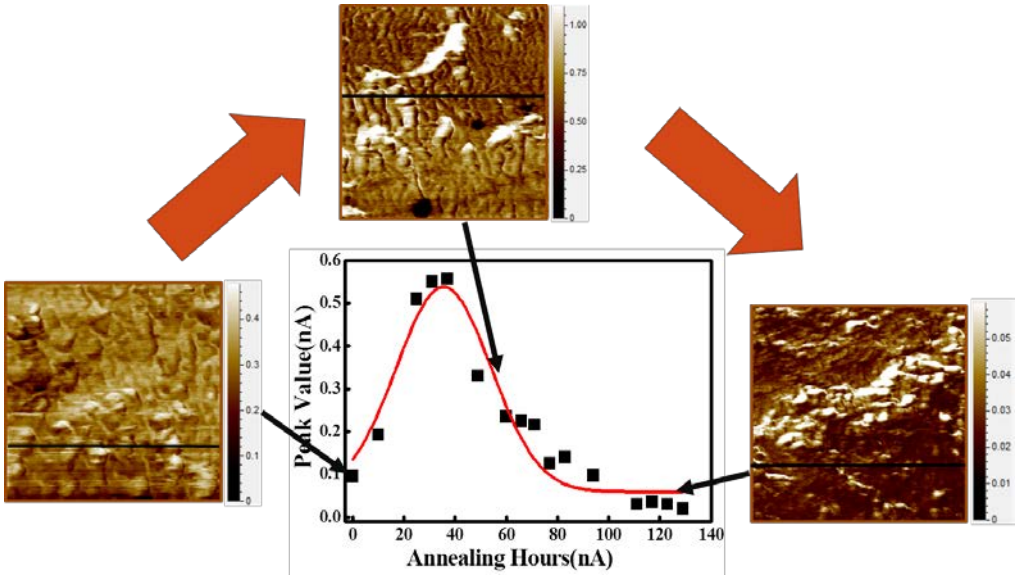

Figure 115. Conductance and current sensing image variation

The aging process of the Nafion membrane can be explained as two steps. Figure 116 and 117 show the simple model of the aging process at each step. Figure 116 (a) and (b) illustrate the ionic channel reorganization while the conductance increases. The glass transition temperature of the Nafion membranes changes in the range of 100^{o}C-150^{o}C which depends on the water uptake by the membrane. [86] As the temperature is close to this range, the mobility of molecules should increase rapidly, making the proton channels easier to rearrange to form a stable state. From the study of Schmidt-Rohr et al., the ionic channel network is explained by the parallel proton channel model using the SAXS and SANS measurement. [37] This model provides a unified view of the ionic structure; however, it is not clear whether such a configuration, presumably formed in the fabrication of the membranes, is a stable one. [89] Between ionic channels, the effective interaction is the

repulsive force and van der Waals force at short and long range [90]. For pristine membranes, the short water channels (ionic channels), are randomly distributed in the membrane and each water channel makes networks as shown in figure 116 (a). When the annealing temperature become close to the glass transition temperature of the Nafion membrane, the ionic channels are diffused and rearranged into a stable state. For the ionic channels near the membrane surface, the ionic channels create are reorganized from perpendicular to parallel with the membrane surface because the interaction between the membrane interface and the ionic channels is attractive. The interaction is due to image charge which is created by the interface. These channels in parallel to the membrane surface might be open on one side forming a groove on the surface, which should increase the contact probability of the channels and the probe tip, and get more channels connected in parallel across the membrane as shown in figure 116 (b). [90] The increased connectivity of ionic channels by the re-organization of the ionic channels improves proton permeability. Thus, conductance in the membrane is increased by thermal annealing. This phenomenon is reported in many other studies. [87, 88, 92] Casciola et al. studied thermal annealing of Nafion 117 membrane [92]. The result shows the same trend as this study. The conductivity was initially increased and then gradually decreased. The conductivity change of the membrane is due to the axis rotation of the ionic channel network. Hensley et al. studied the annealing effect of commercial Nafion® 111 and Nafion® 115 by XRD. The result of their study shows that the conductivity of the membrane was increased during 3 hours annealing. The water and proton permeability of ionic clusters were increased due to the structural change of the ionic cluster and the water and proton permeability increasing induces in the increase conductivity. However, both studies did not report clear evidence of the conductivity variation due to

structural change of the ionic clusters.

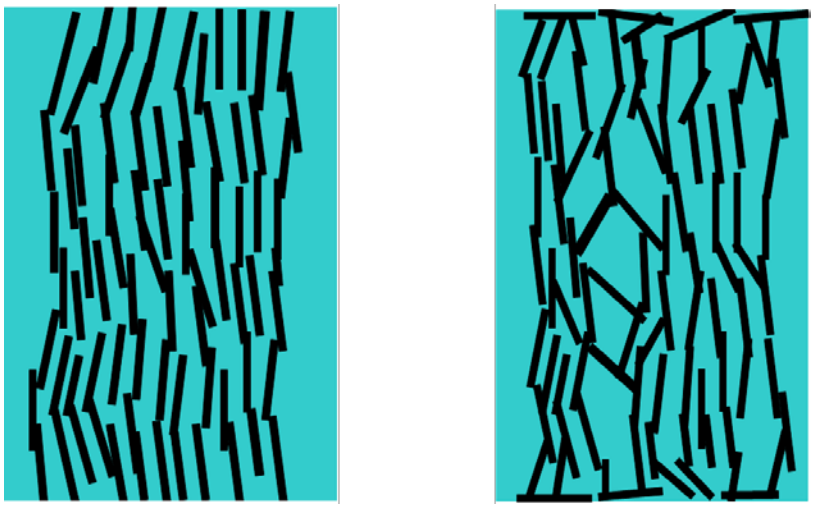

(a) (b)

Figure 116 Simple model of ionic channel network re-organization

Figure 117 illustrates a simple model of sulfonic acid group decomposition. While the conductance on the membrane is decreasing, FWHM and the current in a single channel also show a decrease; however, the average number of clusters in contact with the tip does not change. The rational explanation is that the morphological change of the ionic clusters induces the conductance variation. The morphological change of ionic clusters should be explained by the sulfonic acid group decomposition. Thus, the conductance drop during thermal annealing should be explained by the sulfonic acid group decomposition process in the membrane. The sulfonic acid group decomposition induces a reduction of proton permeability in the ionic channels. The proton conductivity is decreased by the reduction of the proton permeability. The sulfonic acid group decomposition on the low temperature range

(90-150^{o}C) is reported in several studies [38, 64, 67]. These studies insist that the conductance drop due to thermal aging is strongly related to sulfonic acid group decomposition. Collette et al. studied the aging of Nafion 112 membrane under 80^{o}C by IR and NMR. They found that the conductivity of the membrane droped 80% for 20 days when the membrane was annealed at 80^{o}C. During the conductance drop in the membrane, the sulfonic acid group decreased and sulfonic acid anhydride increased according to the NMR measurement. The sulfonic acid group decomposition is directly related in the forming of sulfonic acid anhydride [60]. The anhydride formation on the membrane is also observed by Alentiev et al. study [61]. So, the sulfonic acid group decomposition process can be explained using the formation of sulfonic acid anhydride. From the water channel model, the structure of the ionic channels on the membrane is inverted micelles. The water channel is surrounded by hydrophobic PTFE, which has hydrophilic sulfonic acid tails. The sulfonic acid tail (SO_3^-) is embedded into the water channel as shown in figure 117. In pristine membranes, the sulfonic acid tails are in equilibrium by van de Waals force. When the membrane is annealed near glass transition temperature (90-150^{o}C), the mobility of the sulfonic acid tails is increased. This increased mobility should promote the sulfonic acid anhydride formation by increasing the probability to obtain the optimized distance between the two nearest neighboring sulfonic acid tails. Due to the formation of the anhydride, the sulfonic acid tails are decomposed. Even though the anhydride formation in the water channels explained well decomposition of the sulfonic acid group, there is no direct experimental evidence from this study.

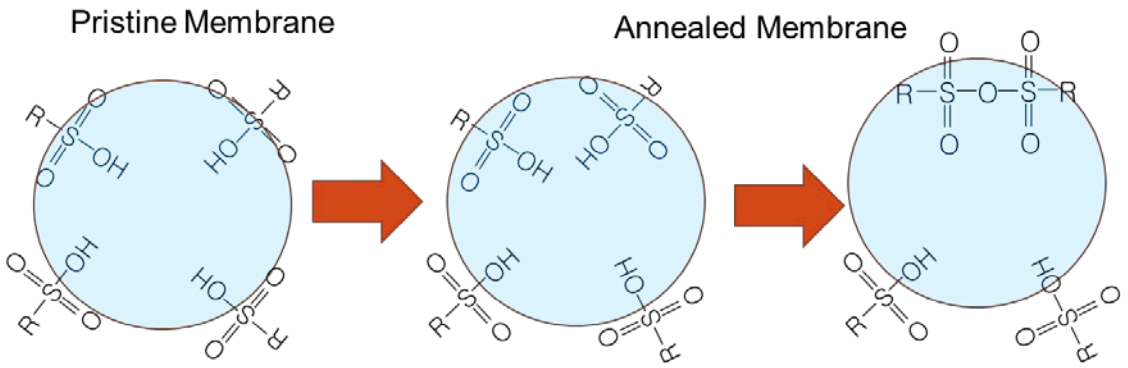

Figure 117. Simple model of conductance decaying

CHAPTER 4

SUMMARY AND DISCUSSION

The aging mechanisms of the Nafion® 115 and Nafion® 212 were studied using the current sensing atomic force microscopy (CSAFM). In order to study thermal aging of both membranes, they are annealed at four different temperatures 90°C, 100°C, 110°C, and 120°C. The result of this study is characterized by the CSAFM images and conductance distribution at each CSAFM image.

The results show that the aging mechanism follows two steps; structural changing of the ionic channel network and sulfonic acid group decomposition. At the early stage, which is annealed within 10 hours, the conductance and conductance roughness (FWHM) in the membrane increases and the current in a single channel increases due to increasing of inter-connection between ionic channels, but the average number of the ionic clusters in contact with the tip does not change. The CSAFM image shows that the ionic clusters are reoriented near the membrane surface. These results reveal that ionic channels near the membrane surface are aligned parallel to the membrane interface. Due to the alignment of ionic channels, the connectivity of each ionic channel is increased. The conductance on the membrane is increased as the result of increasing connectivity of each ionic channel.

After the early stage, the conductance of the membrane decays and reaches to zero. In this stage, FWHM and the current in a single channel gradually decay; however, the average number of the ionic clusters in contact with the tip is constant. The conductance decay due to thermal annealing can be explained by the morphological variation of the ionic channels. When the membranes are continuously annealed, the mobility of the sulfonic acid groups

forming ionic channels is increased. The increasing mobility of ionic channels induces sulfonic acid anhydride is formation. The proton permeability is reduced as the formation of sulfonic acid anhydride. The result of proton permeability reduction, the conductance in the membrane is decreased. These models provide a plausible explanation about the thermal aging mechanism of Nafion membrane. However, the experimental evidence is not sufficient to support these models. So, further research will be required.

REFERENCES

1. Wahdame, B., Candusso, D., Francois, X., Harel, F., Pera, M-C., Hissel, D., and Kauffmann, J. M. Analysis of a Fuel Cell Durability Test Based on Design of Experiment Approach. *IEEE Tansactions on Energy Conversion, 23*, (2008), 1093-1104.

2. Hicker, M. A., Ghassemi, H., Kim, Y. S., Einsla, B. R., and McGrath, J. E. Alternative polymer system for proton exchange membrane (PEMs). *Chemical Reviews 104*, (2004), 4587-4612.

3. Larminie, J. *Fuel Cell System Explained*. Jon Wiley & Sons Ltd, The Atrium Gate, Chicheser, West Sussex, 2003.

4. Heinzel, A., Hebling, C., Muller, M., Zedda, M., and Muller, C. Fuel cells for low power applications. *Journal of Power Sources*, 105 (2002), 250-255.

5. Singhal, S. C. Advances in solid oxide fuel cell technology. *Solid State Ionics 135*, (2000), 305-313.

6. Ormerod, R. M. Solid Oxide Fuel Cells. *Chemical Society Reviews 32*, (2003), 17-28.

7. Mohammed, A., and Mohammed, umar G. Design of an alkaline fuel cell. *Leonardo Electronic Journal of Practices and Technology 9*, (2006), 99-105.

8. Crawley, G. Alkaline fuel cells (AFC). *Fuel cell today* (2006), 1-10.

9. Kordesch, K., and Simader, G. *Fuel cells and their application*, VCH Publishers, Inc., New York, 1996.

10. Rayment, C., and Sherwin, S. Introduction to Fuel Cell Technology Retrieved May 2, 2003, from Department of Aerospace and Mechanical Engineering University of Notre Dame: http://nd.edu/~msen/Teaching/DirStudies/FuelCells.pdf

11. Heidebrechta, P., and Sundmachera, K. Molten carbonate fuel cell (MCFC) with internal reforming: model-based analysis of cell dynamics. *Chemical Engineering Science 58*, (2003), 1029 – 1036.

12. Wu, J., Yuan, X. Z., Martin, J. J., Wang H., Zhang, J., Shen, J., Wu, S., Merida, W. A review of PEM fuel cell durability: Degradation mechanism and mitigation strategies. *Journal of Power Sources 184*, (2008), 104-119.

13. Sammes, N. *Fuel Cell Technology.* Springer-Verlag, London, 2006.

14. Wee, J.-H. Applications of proton exchange membrane fuel cell systems. *Renewable and Sustainable Energy Reviews 11*, (2007), 1720-1738.

15. Santarelli, M. G., and Torchio, M. F. Experimental analysis of the effects of the operating variables on the performance of a single PEMFC. *Energy Conversion and Management 48*, (2007), 40-45.

16. Will, F. G. and Spacil, H. S. Performance analysis of zinc-bromine batteries in vehicle and utility applications. *Journal of Power Sources 5*, (1980), 173-188.

17. Heitner-Wirguin, C. Recent advances in perfluorinated ionomer membranes: structure, properties and applications. *Journal of Membrane Science 120*, (1996), 1-33

18. Yan, W-M., Mei, S-C., Soong, C-Y., Liu, Z-S., and Song, D. Experimental study on the performance of PEM fuel cells with interdigitated flow channel. *Journal of Power Sources 160*, (2006), 116-122.

19. Mehta, V., and Cooper J. S. Review and analysis of PEM fuel cell design and manufacturing. *Journal of Power Sources 114*, (2003), 32-53.

20. James, P. J., McMaster, T. J., Newton, J. M., and Miles, M. J., In situ rehydration of perfluorosulphonate ion-exchange membrane studied by AFM. *Polymer 41*, (2000), 4223-4231.

21. Blanchard, R. M., and Nuzzo, R. G. An infrared study of the effects of hydration on cation-loaded nafion thin films. *Journal of Polymer Science: Part B: Polymer Physics 38*, (2000), 1512-1520.

22. Sammes, N., Bove, R., and Stahl, K. Phosphoric acid fuel cells; Fundamentals and applications, *Current Opinion in Solid State and materials Science 8*, (2004), 372-378.

23. Fujimura, M., Hashimoto, T., and Kawai, H. Small Angle X-ray Scattering Study of Perfluorinated ionomer membranes 1. Origin of Two Scatering Maxima. *Macromolecules 14*, (1981), 1309-1315.

24. Fujimura, M., Hashimoto, T., and Kawai, H. Small Angle X-ray Scattering Study of Perfluorinated ionomer membranes 2. Models for Ionic Scattering Maximum. *Macromolecules 15*, (1982), 1309-1315.

25. Mauritz, K. A., and Moore, R. B. State of understanding of Nafion. *Chemical Reviews 104*, (2004), 4535-4585.

26. Litt, M. H. A reevaluation of Nafion Morphology. *Polym. Prepr. 38*, (1997), 80-81.

27. Startweather, H. W. Crystallinity in perfluorosulfonic acid ionomer and related polymer .

Macromolecules 15 (1982), 320-323.

28. Gebel, G. Small-angle scattering study of water-swollen perfluorinated ionomer membranes. *Macromolecules 30*, (1997), 7914-7920

29. Haubold, H.-G., Vad, Th., Jungbluth, H., and Hiller, P., Nano structure of Nafion: a SAXS study. *Electrochimica Acta 46*, (2001), 1559-1563.

30. Gierke, T. D., Munn, G. E., and Wilson, E. I. The morphology in Nafion perfluorinated membrane products, ad Determined by Wild-and Small-angle X-ray Studies. *Journal of Polymer Science: Polymer Physics Edition 19*, (1981), 1687-1704.

31. Hsu, W. Y., and Gierke, T. D. Elastic theory for ionic clustering in perfluorinated ionomers. *Macromolecules 15*, (1982), 101-105.

32. Roche, E. J., Pineri, M., Duplessix, R., and Levelut, A. M. Samll –angle scattering studies of Nafion Membranes. *Journal of Polymer Science Polymer Physics Edition 19*, (1981), 1-11.

33. Roche, E. J., Pineri, M., and Duplessix, R., Phase separation in perfluorosulfonate ionomer membranes. *Journal of Polymer Science Polymer Physics Edition 20*, (1982), 107-116.

34. Klaus, S.-R., and Chen, Q. Parallel cylindrical water nanochannels in Nafion fuel-cell membranes. *Nature Materials 7*, (2008), 75-83.

35. Gebel, G. Structural evolution of water swollen perfluorosulfonated ionomers from dry membrane to solution, *Polymer 41*, (2000), 5829-5838.

36. Rubtat, L., Rollet, A. L., Gebel G., and Diat, O. Evidence of Elongated Polymeric Aggregates in Nafion. *Macromolecules 35*, (2002), 4050-4055.

37. Rollet, A.-L., Diat, O., and Gebel, G. A new insight into Nafion structure. *Journal of Physical Chemistry B 106*, (2002), 3033–3036.

38.Klus, S.-R., and Qiang, C. Parallel cylindrical water nanochannels in Nafion fuel-cell membranes. *Nature Materials 7*, (2008), 75-83.

39. Wu, J., Yuan, X. Z., Martin, J. J., Wang, H., Zhang, J., Shen, J., Wu, S., and Merida, W. A review of PEM fuel cell durability: Degradation mechanisms and mitigation strategies. *Journal of Power Sources 184*, (2008), 104-119.

40. Yu, J., Matsuura, T., Yoshikawa, Y., Islam, Md N., and Hori, M. Lifetime behavior of a PEM fuel cell with humidification of feed stream. *Phys.Chem.Chem.Phys 7*, (2005), 373-378.

41. Pozio, A., Silva, R. F., Francesco, M. D., and Giorgi, L. Nafion degradation in PEFCs

from end plate iron contamination. *Electrochimica Acta 48*, (2003), 1543-1549.

42. Shores, D. A., and Deluga, G. A. in: Vielstich, W., Gasteiger, H. A., and Lamm, A. *Handbook of Fuel Cells: Fundamentals Technology and Applications, vol 3*, John Wiley&Sons Ltd., 2004, pp 273-285

43. Yan, M. W., Soong, S. C., Liu, Z. and Song, D. Experimental study on the performance of PEM fuel cells with interdigitated flow channels. *Journal of Power Sources 160*, (2006), 116-122.

44. Pozo, A., Silva, R. F., De Francesco, M., and Giorgi, L. Nafion degradation in PEFCs from end plate iron contamination. *Electrochimica Acta 48*, (2003), 1543-1549.

45. Mattsson, B., Ericson, H., Torell, L.M., and Sundholm, F. Degradation of a fuel cell membrane, as revealed by micro-Raman spectroscopy. *Electrochimica Acta 45*, (2000), 1405-1408.

46. Wikie, C. A., Thomsen, J. R., and Mittleman, M. L. Interaction of poly(methyl methacrylate) and nafions. *Journal of Applied Polymer Science 42*, (1991), 901-909.

47. Chu, D., Gervasio, D., Razaq, M., and Yeager, E. B. Infrared reflectance absorption spectroscopy (IRRAS). Study of the thermal stability of perfluorinated sulphonic acid ionomers on Pt. *Journal of Applied Electrochemistry 20*, (1990), 157-162.

48. Elliott, J. A., and Hanna S. Interpretation of the Small-angle X-ray Scattering from Swollen and oriented perfluorinated ionomer membranes. *Macromolecules 33*, (2000), 4161-4171.

49. Crabtree, G. W., Dresselhaus, M. S., and Buchanan, M. V., The Hydrogen Economy. *Physics Today 57*, (2004), 39-45.

50. Cleghorn, S.J.C., Mayfield, D.K., Moore, D.A., Moore, J.C., Rusch, G., Sherman, T.W., Sisofo, N.T., and Beuscher, U. A polymer electrolyte fuel cell life test: 3 years of continuous operation. *Journal of Power Sources 158*, (2006), 446-454.

51. Yu, J., Matsuura, T., Yushikawa, Y. Islam, Md N. and Hori, M. In situ analysis of performance degradation of a PEMFC under nansaturated humidification. *Electrochemical and Solid-State Letters 8*, (2005), A156-A158.

52. Endoh, E., Terazono, S., Widjaja, H., and Takimoto, Y. Degradation study of MEA for PEMFCs under low humidity. *Electrochemical and Solid-State Letters 7*, (2004), A209-A211.

53. Lee, H., Kim,T., Sim, W., Kim, S., Ahn, B., Lim, T., and Park, K. Pinhole formation in PEMFC membrane after electrochemical degradation and wet/dry cycling test. *Korean Journal of Chemical Engineering 38*, (2011), 487-491.

54. Lu, W., Liu, Z., Wang, C., Mao, Z., and Zhang, M. The effects of pinholes on proton exchange membrane fuel cell performance. *International Journal of Energy Research 35*, (2011), 24-30.

55. Weber, A. Z. Gas-crossover and membrane-pinhole effects in polymer-electrolyte fuel cells. *Journal of the Electrochemical Society 155*, (2008), B521-53.

56. Haung, C., Tan, K. S., Lin, J., and Tan, K. L. XRD and XPS analysis of the degradation of the polymer electrolyte in H2–O2 fuel cell. *Chemical Physics Letters 371*, (2003), 80-85.

57. Inaba, M., Kinumoto, T., Kiriake, M., Umebayashi, R., Tasaka, A., and Ogumi, Z. Gas crossover and membrane degradation in polymer electrolyte fuel cell, *Electrochimica Acta 51*, (2006), 5746-5753.

58. Borup, R., Meyers, J., Pivovar, B., Kim, Y. S., Mukundan, R., Garland, N., Myers, D., Wilson, M., Garzon, F., Wood, D., Zelenay, P., More, K., Stroh, K., Zawodzinski, T., Boncella, X. J., McGrath, J. E., Inaba, O. M., Miyatake, K., Hori, M., Ota, K., Ogumi, Z., Miyata, S., Nishikata, A., Siroma, Z., Uchimoto, Y., Yasuda, K., Kimijima, K.-I., and Iwashita, N. Scientific aspects of polymer electrolyte fuel cell durability and degradation. *Chemical Reviews 107*, (2007), 3904-3951.

59. Wang, H., and Capuano, G. A. Behavior of raipore radiation-grafted polymer membranes in H2/O2 fuel cells. *Journal of Electrochemical Society 145*, (1998), 780–788.

60. Surowiec, J., and Bogoczek, R. Studies on the thermal stability of the perfluorinated cation-exchange membrane Nafion-417. *Journal of Thermal Analysis and Calorimetry 33*, (1988), 1097-1102

61. Wilkie, C. A., Thomsen J. R., and Mittleman, M. L., Interaction of poly(methyl mechacrylate) and Nafions. *Journal of Applied Plymer science 42*, (1991), 901-909.

62. Baur, B., Jones, D. J., Roziere, J., Tchicaya, L., Alberti, G., and Casciola, M. Electrochemical characterization of sulfonated polytheerketone membrane. *Journal of New Material Electrochemical Systems 3*, (2000), 93-98.

63. Yang, C., Srinivasan, S., Bocarsly, A. B., Tulyani, S., and Benziger, J. B. A comparison of physical properties and fuel cell performance of Nafion and zirconium phosphate/Nafion composite membranes. *Journal of Membrane Science 237*, (2004), 145–161.

64. Collette, F. M., Lorentz, C., Gebel, G., and Thominette, F. Hygrothermal aging of Nafion. *Journal of Membrane Science 330*, (2009), 21-29.

65. Alentiv, A., Kostina, J., and Bondarenko, G. Chemical Aging of Nafion: FTIR Study. *Desalination 200*, (2006), 32-33.

66. Liang, Z., Chen, W., Liu, J., Wang, S., Zhou, Z., Li, W., Sun, G., and Xin, Q. FT-IR study of the microstructure of Nafion membrane. *Journal of Membrane Science 223*, (2004), 39-44.

67. Shibahara, Y., Akiyama, Y., Izumi, Y., Nishijima, S., Honda, Y., Kimura, N., Tagawa, S., and Isoyama, G. Analysis of thermal degradation process of Nafion-117 with age-momentum correlation method. *Journal of Polymer Science Part B: Polymer Physics 46*, (2008), 1-7.

68. Kundu, S., Simon, L. C., and Fowler, M. W. Comparison of Two accelerated Nafion degradation experiments. *Polymer Degradation and Stability 93*, (2008), 214-224.

69. Anderson, M. S., and Pike, W. T. A Raman-atomic force microscope for apertureless-near-field spectroscopy. *Review of Scientific Instruments 73*, (2002), 1198.

70. Kwon, J., Hong, J., Kim, Y., Lee, D., Lee, K., Lee, S., and Park, S. Atomic force microscope with improved scan accuracy, scan speed, and optic vision. *Review of Scientific Instruments 74*, (2003), 4378-4383.

71. The UK's National Measurement Laboratory "Theory of atomic force microscopy", available from http://www.npl.co.uk/smd/npl_reasearch/afm_theory.html; internet; accessed 1 September 2007.

72. Kang, Y., Kwon, O., Xie, X., and Zhu, D.-M. Conductance Mapping of Proton Exchange Membranes by Current Sensing Atomic Force Microscopy. *Journal of Physical Chemistry B 113*, (2009), 15040–15046.

73. Xie, X., Kwon, O., and Zhu, D.-M. Local Probe and Conduction Distribution of Proton Exchange Membranes. *Journal of Physical Chemistry B 111*, (2007), 6134-6140.

74. Kundu, S., Simon, L. C., Fowler, M., and Grot, S. Mechanical properties of Nafion electrolyte membranes under hydrated conditions. *Polymer 46*, (2005), 11707–11715.

75. Elliott, J. A., and hanna, S. Elimination of orientation in Perfluorinated ionomer membranes. *Polymer Engineering and Science 46*, (2006), 228-234.

76. Mistry, M. K., Choudhury, N. R., Dutta, N. K., and Knott, R. Nanostructure evolution in high-temperature perfluorosulfonic acid ionomer membrane by small-anle X-ray Scattering. *Langmuir 26*, (2010), 19073-19083.

77. Page, K. A., Cable, K. M., and Moore, R. B. Molecular origin of the thermal transitions and dynamic mechanical relaxation in perfluorosulfonate ionomers. *Macromolecules 38*, (2005), 6472-6484.

78. Hill, T. A., Carroll, D. L., Czerw, R., Martin, C. W., and Perahia, D. Atomic force microscopy studies on the dewetting of perfluorinated ionomer thin films. *Journal of polymer*

science part B: Polymer Physics 41, (2002), 149-157.

79. Li, J., Wilmsmeyer, G., and Madsen, L. A. Hydrophilic channel alignment modes in perfluorosulfonate ionomer: Implications for proton transport. *Macromolecules 41*, (2008), 4555-4557.

80. Jang, S. S., Milinero, V., Cagin, T., and Gaddard III, W. A. Nanophase-segregation and transport in Nafion 117 from molecular Dynamics simulations: Effect of monomeric sequence. *Journal of physical chemistry B 108*, (2004), 3149-3157.

81. Laun, Y., Zhang, Y., Zhang, H., Li, L., Li, H., and Liu, Y. Annealing effect of perfluorosulfonated ionomer membranes on proton conductivity and methanol permeability, *Journal of applied polymer science 107*, (2008), 396-402.

82. Carbone, A., Pedicini, R., Longo, A., D'llario, L., and Passalacqua, E. Sulponated poly(ether ether ketone) membranes for fuel cell application: Thermal and structural Characterization. *Journal of Power Sources 163*, (2006), 18-26.

83. Hensley, J. E., Way, D. J., Dec, S. F., and Abney, K. D. The effects of thermal annealing on commercial Nafion membranes. *Journal of Membrane Science 298*, (2007), 190-201.

84. Wang, X., Yakovlev, S., Beers, K. M., Park, M. J., Mullin, S. A., Downing, K. H., and Balsara, N. P. On the origin of slow changes in ionic conductivity of model block copolymer electrolyte membranes in contact with humid air. *Macromolecules 43*, (2010), 5306-5314.

85. Page, K. A., Landis, F. A., Philips, A. K., and Moor, R. B. SASX analysis of the thermal relaxation of anisotropic morphologies in oriented nafion membrane. *Macromolecules 39*, (2006), 3939-3946.

86. Kwon, O., Wu, S., and Zhu, D.-M. Configuration changes of conducting channel network in Nafion membranes due to thermal annealing. *Journal of Physical Chemistry B 114*, (2010), 14989–14994.

87. Boas, L. M. *Mathematical methods in the physical science*. John Wiley and Sons, Canada, 1983.

88. Hensley, J. E., Way a, J. D., Decb, S. F., and Abney, K. D. The effects of thermal annealing on commercial Nafion® membranes. *Journal of Membrane Science 298*, (2007), 190–201.

89. Silva, V., Silva, V., Mendes, A., Madeira, L., and Nunes, S. Pre-treatment effect on the transport properties of sulfonated poly(ether ether ketone) membranes for DMFC application. *Desalination 200*, (2006), 645-647.

90. Bouaskarne, M., Amokrane, S., and Regnaut, C. Effective interaction between reverse

micelles: A study from the potential of mean force at infinite dilution. *Journal of Chemical Physics 114*, (2001), 2442–2451.

91. Casciola , M., Alberti, G., Sganappa, M., and Narducci, R. On the decay of Nafion proton conductivity at high temperature and relative humidity. *Journal of Power Sources 162*, (2006), 141–145.

92. Chena, C., Levitina, G., Hessa, D. W., and Fullera, T. F. XPS investigation of Nafion® membrane degradation. *Journal of Power Sources 169*, (2007), 288-295.

VITA

O Sung Kwon was born on December 5, 1972, in Kyoung Sang Buk Do, Republic of Korea. He was educated by local public school and Kyoung-Sang High School as class valedictorian in 1992. He was enrolled in Myoung-Ji University in 1993 and graduated in 1999. His degree was a Bachelor of Science in Physics. He was matriculated in Master program of Myoung-Ji University in 1999.

In 2000, he joined a research group of Korea Research Institute of Standard and Science.

In September 2004, Mr. Kwon became a graduate student in University of Missouri-Kansas City. He completed his Ph.D. of Physics degree in Physics in summer 2011.

Mr. Kwon is a member of the American Physical Society.